



Universiteit
Leiden
The Netherlands

Advanced MRI markers of cerebral small vessel disease

Harten, T.W. van

Citation

Harten, T. W. van. (2024, January 31). *Advanced MRI markers of cerebral small vessel disease*. Retrieved from <https://hdl.handle.net/1887/3715772>

Version: Publisher's Version

License: [Licence agreement concerning inclusion of doctoral thesis in the Institutional Repository of the University of Leiden](#)

Downloaded from: <https://hdl.handle.net/1887/3715772>

Note: To cite this publication please use the final published version (if applicable).

Colophon

ISBN: 978-94-90858-83-4

Printing: drukkerij Mostert & Van Onderen

Copyright © Thijs W. van Harten, The Netherlands 2024. All rights are reserved. No part of this book may be reproduced, distributed, stored in a retrieval system, or transmitted in any form or by any means, without prior written permission of the author.

Financial support by the Dutch Heart Foundation for the publication of this thesis is gratefully acknowledged. The research described in this thesis was supported by a grant from the Dutch Heart Foundation (14729) This research has been made possible by the Dutch Heart Foundation and the Netherlands Organisation for Scientific Research (NWO), as part of their joint strategic research programme: "Earlier recognition of cardiovascular diseases". This project is partially financed by the PPP Allowance made available by Top Sector Life Sciences & Health to the Dutch Heart foundation to stimulate public-private partnerships.

Advanced MRI markers of cerebral small vessel disease

Proefschrift

ter verkrijging van
de graad van doctor aan de Universiteit Leiden,
op gezag van rector magnificus prof. dr. ir. H. Bijl,
volgens besluit van het college voor promoties
te verdedigen op woensdag 31 januari 2023
klokke 13:45 uur

door

Thijs Wijnzen van Harten
geboren te 's-Gravenhage
in 1985

Promotores

Prof. dr. ir. M.J.P. van Osch

Prof dr. M.J.H. Wermer

Copromotor

Dr. M.A.A. van Walderveen

Leden promotiecommissie

Dr. J. Claassen

Dr. E. van Etten

Prof. dr. J. Hendrikse

Prof. dr. A. Webb

Radboud University Medical Center

University Medical Center Utrecht

Table of Contents

Chapter 1	General introduction.....	5
Chapter 2	On the ability to exploit signal fluctuations in pseudocontinuous Arterial Spin Labeling for inferring the major flow territories from a traditional perfusion scan	19
Chapter 3	Impact of ROI definition on visual stimulation based cerebral vascular reactivity fMRI with a special focus on applications in Cerebral Amyloid Angiopathy	41
Chapter 4	High temporal resolution fMRI for visual-activation induced vascular reactivity measurements in D-CAA mutation carriers .	67
Chapter 5	Quantitative measurement of cortical Superficial Siderosis in Cerebral Amyloid Angiopathy	89
Chapter 6	Brain Deep Medullary Veins on 7T MRI in Dutch-Type Hereditary Cerebral Amyloid Angiopathy	105
Chapter 7	Summary and discussion.....	122
Nederlandse samenvatting.....		135
List of publications.....		141
Curriculum vitae.....		145

Chapter 1

General Introduction

The cerebral vasculature

The brain is a very metabolically active organ with 20% of total oxygen and glucose consumption at rest [1]. To ensure that the blood flow is maintained at appropriate levels to deliver these nutrients a complex system of arteries, veins and capillaries is present [2]. This system is able to regulate a stable flow of blood during changes in blood pressure [2, 3].

In case of a stroke, the blood vessels supplying the brain are acutely affected. These blood vessels are either obstructed in case of ischemic stroke or ruptured in case of hemorrhagic stroke. Stroke can be caused by large artery disease which encompasses a range of conditions, including aneurysms, dissections and atherosclerosis of large vessels. Global Burden of Disease (GBD) 2019 stroke burden estimates an incidence of 6 million for ischemic stroke and 4.5 million for hemorrhagic strokes in the year 2019 [4, 5]. The lifetime risk of stroke between 1990 and 2016 showed a relative increase from 8.9% to 24.9% [6]. This increase is mainly caused by regions scoring around the middle of the sociodemographic index, where stroke incidence remained similar or increased, while non-stroke mortality declined.

The cerebral vasculature can also be affected in a more chronic way. Cerebral small vessel disease (cSVD) is a diverse range of chronic and progressive disorders that affect the smallest blood vessels of the brain [7, 8]. Hypertension, diabetes mellitus and cerebral amyloid angiopathy (CAA) are the most common causes of cSVD. Hypertension and diabetes primarily lead to damage in the deep brain regions, but may also affect lobar regions, while CAA primarily exhibits lobar pathology. Comparable to larger artery stroke, cSVD can also result in acute stroke when small cerebral vessels acutely rupture or occlude.

Cerebral amyloid angiopathy

As one of the most common forms of cSVDs, CAA is a major cause of Intracerebral Hemorrhage (ICH) and dementia in the elderly [9]. A recent meta-analysis found a prevalence of moderate to severe CAA pathology in 24.1% of patients with an ICH, and 56.7% in lobar ICH [10]. CAA is often a comorbidity in Alzheimer's disease and in 48% of patients a moderate to severe CAA pathology is found and in 22% MRI markers related to CAA pathology can be observed [9]. Even otherwise healthy elderly 23% show moderate to severe CAA pathology and 8% MRI markers related to CAA pathology [10]. CAA is thought to develop in four pathophysiological stages[11]. Initially, amyloid- β is deposited in the wall of blood vessels, followed by the development of changes in cerebrovascular function. Next, non-hemorrhagic damage to brain tissue occurs, and finally hemorrhagic injury to brain tissue represents the last stage. There is overlap between these stages, but they start subsequently to each other. These stages in total take many years, and the earliest is thought to start decades before symptoms arise. A graphic representation of a proposed model of these stages is shown in *Figure 1*. However, the axes should be considered illustrative and further research is needed to pinpoint the temporal position of the stages in the cascade more precisely, similar to the framework proposed for Alzheimer's disease by Jack *et al.* [11, 12].

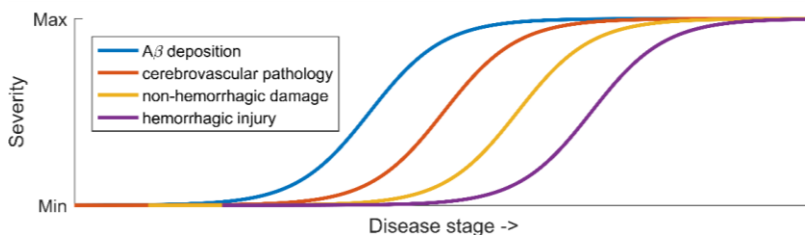


Figure 1: a graphic representation of the proposed model for disease stages of CAA.

CAA pathology is generally found in the small and medium sized arteries of brain, and less frequently also involves the veins [13]. The diagnosis of CAA can be

difficult, as the definite diagnosis can only be made post mortem by histological examination of brain tissue. In vivo, however, imaging with MRI plays a central role and can be used to establish the diagnosis of probable or possible CAA in clinical practice. Currently, CAA is diagnosed according to the Boston criteria. These criteria have gone through several iterations over the years [14-18]. The current version of the Boston criteria (version 2.0) is shown in *Table 1*. While the first versions of the criteria only included hemorrhagic based lesions as imaging evidence of CAA, the current version also includes non-hemorrhagic markers such as enlarged perivascular spaces and the presence of a multispot pattern of white matter hyperintensities (WMH) (>ten small round or oval T2-weighted hyperintense lesions in the bilateral subcortical white matter). The changes from the previous version are indicated with † in *Table 1* [18]. The Boston criteria rely on MRI, should this modality be contraindicated or unavailable a probability of moderate to severe CAA can also be determined by the Edinburgh criteria, based on CT imaging and genotyping [19, 20].

Table 1: Boston criteria version 2.0[18]. Changes from version 1.5 are indicated by †.

Boston criteria version 2.0 for sporadic cerebral amyloid angiopathy

1. Definite CAA
 - a. Full brain post-mortem examination demonstrating:
 - i. Spontaneous intracerebral hemorrhage, transient focal neurological episodes, convexity subarachnoid hemorrhage, or cognitive impairment or dementia
 - ii. Severe CAA with vasculopathy
 - iii. Absence of other diagnostic lesion
2. Probable CAA with supporting pathology
 - a. Clinical data and pathological tissue (evacuated hematoma or cortical biopsy) demonstrating:
 - i. Presentation with spontaneous intracerebral hemorrhage, transient focal neurological episodes, convexity subarachnoid hemorrhage, or cognitive impairment or dementia
 - ii. Some degree of CAA in specimen
 - iii. Absence of other diagnostic lesion
3. Probable CAA
 - a. For patients aged 50+ years and older, clinical data and MRI demonstrating:
 - i. Presentation with spontaneous intracerebral hemorrhage, transient focal neurological episodes, or cognitive impairment or dementia
 - ii. At least two of the following strictly lobar hemorrhagic lesions on T2*-weighted MRI, in any combination: intracerebral hemorrhage, cerebral microbleeds, or foci of cortical superficial siderosis or convexity subarachnoid hemorrhage
 - b. OR
 - i. One lobar hemorrhagic lesion plus one white matter feature (severe perivascular spaces in the centrum semiovale or white matter hyperintensities in a multispot pattern)†
 - ii. Absence of any deep hemorrhagic lesions (i.e., intracerebral hemorrhage or cerebral microbleeds) on T2*-weighted MRI
 - iii. Absence of other cause of hemorrhagic lesions
 - iv. Hemorrhagic lesion in cerebellum not counted as either lobar or deep hemorrhagic lesion
4. Possible CAA
 - a. For patients aged 50+ years and older, clinical data and MRI demonstrating:
 - i. Presentation with spontaneous intracerebral hemorrhage, transient focal neurological episodes, or cognitive impairment or dementia
 - ii. Absence of other cause of hemorrhage
 - iii. One strictly lobar hemorrhagic lesion on T2*-weighted MRI: intracerebral hemorrhage, cerebral microbleeds, or foci of cortical superficial siderosis or convexity subarachnoid hemorrhage

- b. OR
- i. One white matter feature (severe visible perivascular spaces in the centrum semiovale or white matter hyperintensities in a multispot pattern)[†]
 - ii. Absence of any deep hemorrhagic lesions (i.e., intracerebral hemorrhage or cerebral microbleeds) on T2*-weighted MRI
 - iii. Absence of other cause of hemorrhagic lesions
 - iv. Hemorrhagic lesion in cerebellum not counted as either lobar or deep hemorrhagic lesion

Dutch-type hereditary cerebral amyloid angiopathy

While most cases of CAA are sporadic, a number of mutations are known to cause familial forms of CAA [21]. To this day Dutch-type hereditary CAA (D-CAA) is the best described and investigated form of hereditary CAA. D-CAA, formerly known as Hereditary Cerebral Hemorrhage with Amyloidosis- Dutch type (HCHWA-D), is an autosomal dominant disease caused by an E693Q point mutation on the APP gene, resulting in accumulation of abnormal amyloid- β peptide [22]. While its autosomal dominant nature was described as early as 1982 [23], the exact mutation of D-CAA was only discovered in 1990 [24]. D-CAA is seen as a pure model to study disease progression and pathology of sporadic CAA (sCAA). Like in sCAA, pathological examination of D-CAA shows extensive vascular amyloid-beta deposition in leptomeningeal and cortical arteries [25]. Furthermore, we see a similar, but faster disease progression pattern as with sCAA that starts at an earlier age [11, 26]. Conversely, D-CAA only rarely shows neuritic plaques or neurofibrillary tangles as seen in Alzheimer's disease [25] and is free from comorbidities due to general aging. Because of the genetic nature of the disease and therefore the availability of testing in combination with the full clinical penetrance of the mutation, it is possible to follow disease progression starting from the presymptomatic stage.

Magnetic resonance imaging markers of cerebral amyloid angiopathy

The constant evolution of our understanding of disease progression of CAA, results in a continuous need to refine our imaging methodology to better diagnose and classify patients, especially in light of potential clinical trials on CAA treatment. MRI has shown to be a powerful tool for both clinicians and scientists to study cerebrovascular diseases [18]. In the Boston criteria several subtypes of hemorrhages are included. Besides ICH and microbleeds, the Boston criteria also include cortical superficial siderosis (cSS) and convexity subarachnoid hemorrhages (cSAH). Especially, cSS has shown to be a very potent marker for prediction of ICH [27-29], and is scored in research using a categorical scale [30]. Other markers, such as WMH, were traditionally also scored on a qualitative scale, such as the Fazekas score [31]. However, in many populations this was shown to be of limited value due to ceiling effects and thus large heterogeneity in the highest category [32]. Many research papers now opt to quantify the volume of WMH instead of using only a Fazekas score. A similar approach may also be valuable for other markers, such as cSS.

Besides the MRI features incorporated in the Boston criteria, research shows numerous other imaging markers associated with development and progression of CAA. In its most recent iteration, the non-hemorrhagic markers enlarged perivascular spaces[33] and multispot pattern WMH were added apart from the hemorrhagic markers. There is also a strong association in CAA with cortical thinning [34, 35], microinfarcts [36] and changes in diffusion measures [37]. Moreover, impaired cerebrovascular function, as can be measured in vivo with functional MRI, has been proven to be an important hallmark of the disease [38-40]. These, as well as potentially other, novel MRI methods or postprocessing of MRI data are expected to be highly valuable to further qualify and quantify pathology and disease progression of CAA, both for use in clinical practice, as well as marker in future clinical trials on CAA.

Magnetic resonance imaging techniques

MRI is an imaging technique that relies on an interplay between magnetic fields and radio waves. Any nucleus that has a non-zero spin can be used to generate contrast, but in medicine hydrogen atoms are generally used, as they are ubiquitous in organic molecules and especially water. By placing a subject in a strong and homogenous magnetic field, protons will start to precess around the direction of the magnetic field. By applying a pulse scheme consisting of a combination of magnetic gradients and radio frequency pulses, different contrasts can be generated. By choosing the right combination one can generate contrast based on the relative density of excited protons, differences in relaxation times, as well as many other parameters. The contrast generated is always sensitive to more than one property, but one can emphasize the contrast mechanism of interest and minimize the contribution of other mechanisms on that image contrast. There are two types of MR sequences discussed in this thesis that warrant further elaboration:

Pseudo-continuous arterial spin labeling perfusion MRI

Arterial spin labeling (ASL) MRI is a non-invasive technique that uses the water in blood as an endogenous tracer to measure cerebral perfusion. Pseudo-continuous ASL (pCASL) is currently the recommended and most used version of ASL [41]. This technique is based on the labeling of water spins that traverse a labeling plane in a blood vessel, which are then measured in an organ further downstream. For example when measuring cerebral hemodynamics one would introduce a labeling plane in the neck (see Figure 2) and the readout would be planned through the brain. After labeling, a certain pause is included, which is called the 'post labeling delay', after which the readout is performed. In a typical pCASL experiment a number of image pairs are acquired. Such pairs consist of a label and control image, i.e. one image in which the blood was labeled and one without labeling.

These two images are subtracted, after which only the signal of the labeled water will remain. Acquisition of such image pairs are subsequently repeated and averaged to increase the signal to noise ratio, as the signal of the labeled water is only a small percentage of the total signal and therefore quite noisy.

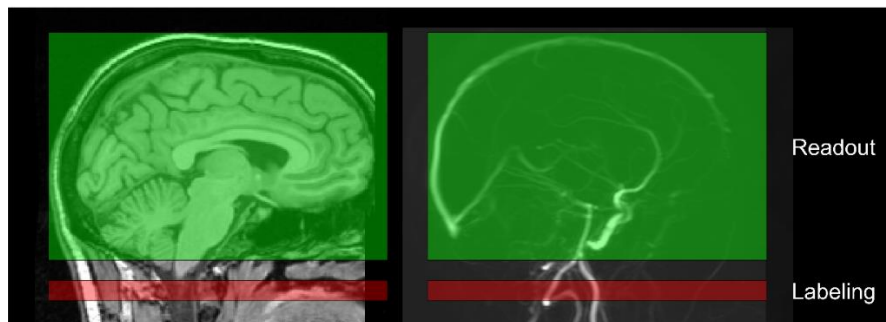


Figure 2: Labeling and readout positioning in brain pCASL. As water in the blood crosses the labelling plane (depicted in red) it is labeled, after which it is imaged in the readout (green), where it travelled to during the post-labeling delay period.

Blood oxygen level dependent (BOLD) MRI

Blood oxygen level dependent (BOLD) contrast is generated from a change in the local concentration of deoxygenized hemoglobin. As hemoglobin becomes deoxygenized, the magnetic properties also change, from slightly diamagnetic to highly paramagnetic [42]. The presence of the deoxygenized hemoglobin in blood vessels causes local disturbances of the magnetic field. As BOLD signal changes are merely a reflection of local concentration of deoxygenized hemoglobin and how this affects the local magnetic field, the extent of the BOLD-effect is influenced by a mixture of neuronal activation and thus local oxygen consumption and the accompanying changes in local cerebral blood flow and volume, i.e. the hemodynamic response. In the brain this local response to neuronal activation is tightly regulated by the phenomenon known as neurovascular coupling: the interaction between neuronal activity and the vasculature [43]. In BOLD

experiments typically many images are made in succession, and the local signal changes are used to detect brain function.

A graphical representation of the difference between the basal and activated state is shown in *Figure 3* [44]. A higher concentration of deoxygenized hemoglobin leads to a lower signal on BOLD images. The default hemodynamic response curve of the BOLD signal occurring after neuronal activation can be divided into three parts, as described previously in the balloon model [45]. First, there is an initial dip, where oxygen consumption is elevated and the blood flow and volume start to increase. This is followed by an overshoot, where blood flow increases much more than oxygen consumption. The third and final stage is a post-stimulus undershoot, where blood volume returns slower to its baseline state after the inflow has diminished.

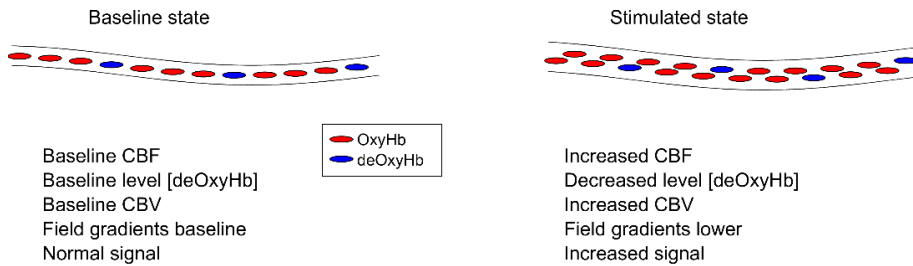


Figure 3: adapted from Matthews et al[44]. In a stimulated state increases in oxygen consumption, blood flow and blood volume lead to an increase of MRI signal, i.e. the BOLD-effect.

Thesis outline

In this thesis new- and improvements to existing MRI methods are explored that provide information on cerebrovascular pathology. The proposed MRI techniques and postprocessing encompass the complete cerebrovascular tree, starting with the large arteries (**chapter 2**), followed by measurements of the function of

penetrating arteries (**chapters 3 and 4**), to quantification of remnants of hemorrhages in the parenchymal tissue (**chapter 5**), to finally the venous compartment (**chapter 6**).

In **chapter 2** the possibility to extract additional information from standard pCASL perfusion scans is investigated and especially whether the large flow territories could be extracted from such data. The degree of fluctuations in the labeling plane that are needed to allow differentiation between the flow territories of both internal carotid arteries is explored using several state of the art statistical methods. Subsequently, it is studied whether these methods would perform better in the presence of severe large vessel pathology compared to normal circumstances.

As mentioned previously, the cerebrovascular function is changed in CAA and this is considered a candidate biomarker for clinical trials on CAA [26, 39, 46, 47]. In **chapter 3** we investigated several post-processing methods used in literature to measure cerebrovascular reactivity with fMRI, and specifically focus on the ROI-selection from which the reactivity is measured.

Whereas **chapter 3** relied on 3T data with a traditional reactivity measurement protocol, the next chapter focuses on 7T MRI and more advanced BOLD-sequences. This new experimental paradigm exhibits a high temporal resolution and employ a short stimulus (3s) with a long rest period (45s). In **chapter 4** this new approach is tested to see whether it would better describe the hemodynamic changes as occurring in CAA. The new reactivity measurements are then compared to the conventional method, which has a much lower (150-200 times) temporal resolution and a paradigm consisting of long stimulus (~20s) and shorter rest period (~28s).

For research purposes we may need more sensitive descriptions of qualitatively and categorically scored markers. One of the emerging markers of CAA is the

forementioned cSS. The categorical scoring approach of this marker is severely hampered by ceiling effects, especially in D-CAA patients, who have a faster disease progression than sCAA patients. To better monitor progression in longitudinal studies, as well as to be able to evaluate differences between patients with a high burden of cSS, we propose a new semi-automatic and quantitative method in **chapter 5**.

While CAA pathology is mainly found in the smaller leptomeningeal and cortical arteries, in some elderly patients CAA pathology is also found in venous vessels [48]. In many cSVDs changes in deep medullary veins have been described. CAA is one of the most common cSVDs and often a comorbidity of Alzheimer's disease [9, 10]. Furthermore, venous morphology is changed in Alzheimer's disease [49]. Therefore, we investigated in **chapter 6** whether CAA pathology causes changes to the venous morphology in a Dutch type hereditary CAA population.

Finally, in **chapter 7**, the findings of this thesis are summarized and discussed.

REFERENCES

1. Shulman, R.G., et al., *Energetic basis of brain activity: implications for neuroimaging*. Trends in Neurosciences, 2004. **27**(8): p. 489-495.
2. Claassen, J.A.H.R., et al., *Regulation of cerebral blood flow in humans: physiology and clinical implications of autoregulation*. 2021. **101**(4): p. 1487-1559.
3. Paulson, O.B., S. Strandgaard, and L. Edvinsson, *Cerebral autoregulation*. Cerebrovasc Brain Metab Rev, 1990. **2**(2): p. 161-92.
4. Feigin, V.L., et al., *World Stroke Organization (WSO): Global Stroke Fact Sheet 2022*. Int J Stroke, 2022. **17**(1): p. 18-29.
5. *Global, regional, and national burden of stroke and its risk factors, 1990-2019: a systematic analysis for the Global Burden of Disease Study 2019*. Lancet Neurol, 2021. **20**(10): p. 795-820.
6. Feigin, V.L., et al., *Global, Regional, and Country-Specific Lifetime Risks of Stroke, 1990 and 2016*. N Engl J Med, 2018. **379**(25): p. 2429-2437.
7. Chojdak-Lukasiewicz, J., et al., *Cerebral small vessel disease: A review*. Adv Clin Exp Med, 2021. **30**(3): p. 349-356.
8. Pantoni, L., *Cerebral small vessel disease: from pathogenesis and clinical characteristics to therapeutic challenges*. Lancet Neurol, 2010. **9**(7): p. 689-701.
9. Greenberg, S.M., et al., *Cerebral amyloid angiopathy and Alzheimer disease - one peptide, two pathways*. Nat Rev Neurol, 2020. **16**(1): p. 30-42.
10. Jäkel, L., et al., *Prevalence of cerebral amyloid angiopathy: A systematic review and meta-analysis*. Alzheimers Dement, 2022. **18**(1): p. 10-28.

11. Koemans, E.A., et al., *Progression of cerebral amyloid angiopathy: a pathophysiological framework*. The Lancet Neurology, 2023.
12. Jack, C.R., et al., *Tracking pathophysiological processes in Alzheimer's disease: an updated hypothetical model of dynamic biomarkers*. The Lancet Neurology, 2013. **12**(2): p. 207-216.
13. Vinters, H.V., *Cerebral amyloid angiopathy. A critical review*. Stroke, 1987. **18**(2): p. 311-24.
14. Greenberg, S.M., et al., *Apolipoprotein E epsilon 4 and cerebral hemorrhage associated with amyloid angiopathy*. Ann Neurol, 1995. **38**(2): p. 254-9.
15. Greenberg, S.M. and M.A. Edgar, *Case records of the Massachusetts General Hospital. Weekly clinicopathological exercises. Case 22-1996. Cerebral hemorrhage in a 69-year-old woman receiving warfarin*. N Engl J Med, 1996. **335**(3): p. 189-96.
16. Greenberg, S.M. and J.P. Vonsattel, *Diagnosis of cerebral amyloid angiopathy. Sensitivity and specificity of cortical biopsy*. Stroke, 1997. **28**(7): p. 1418-22.
17. Greenberg, S.M. and A. Charidimou, *Diagnosis of Cerebral Amyloid Angiopathy: Evolution of the Boston Criteria*. Stroke, 2018. **49**(2): p. 491-497.
18. Charidimou, A., et al., *The Boston criteria version 2.0 for cerebral amyloid angiopathy: a multicentre, retrospective, MRI-neuropathology diagnostic accuracy study*. Lancet Neurol, 2022. **21**(8): p. 714-725.
19. Rodrigues, M.A., et al., *The Edinburgh CT and genetic diagnostic criteria for lobar intracerebral haemorrhage associated with cerebral amyloid angiopathy: model development and diagnostic test accuracy study*. The Lancet. Neurology, 2018. **17**(3): p. 232-240.
20. van Etten, E.S., et al., *Sensitivity of the Edinburgh Criteria for Lobar Intracerebral Hemorrhage in Hereditary Cerebral Amyloid Angiopathy*. Stroke, 2020. **51**(12): p. 3608-3612.
21. Biffi, A., *Main features of hereditary cerebral amyloid angiopathies: A systematic review*. Cereb Circ Cogn Behav, 2022. **3**: p. 100124.
22. Maat-Schieman, M., R. Roos, and S. van Duinen, *Hereditary cerebral hemorrhage with amyloidosis-Dutch type*. Neuropathology, 2005. **25**(4): p. 288-97.
23. Wattendorff, A.R., et al., *Familial cerebral amyloid angiopathy presenting as recurrent cerebral haemorrhage*. J Neurol Sci, 1982. **55**(2): p. 121-35.
24. Levy, E., et al., *Mutation of the Alzheimer's disease amyloid gene in hereditary cerebral hemorrhage, Dutch type*. Science, 1990. **248**(4959): p. 1124-6.
25. Revesz, T., et al., *Sporadic and familial cerebral amyloid angiopathies*. Brain Pathol, 2002. **12**(3): p. 343-57.
26. van Dijk, S.E., et al., *Longitudinal Progression of Magnetic Resonance Imaging Markers and Cognition in Dutch-Type Hereditary Cerebral Amyloid Angiopathy*. Stroke, 2022. **53**(6): p. 2006-2015.
27. Charidimou, A., et al., *Emerging concepts in sporadic cerebral amyloid angiopathy*. Brain, 2017. **140**(7): p. 1829-1850.
28. Charidimou, A., et al., *Cortical superficial siderosis: detection and clinical significance in cerebral amyloid angiopathy and related conditions*. Brain, 2015. **138**(Pt 8): p. 2126-39.
29. Greenberg, S.M. and E.E. Smith, *Implications of cortical superficial siderosis in CAA. Superficial relationships*, 2019. **92**(8): p. 360-361.
30. Charidimou, A., et al., *Cortical superficial siderosis multifocality in cerebral amyloid angiopathy: A prospective study*. Neurology, 2017. **89**(21): p. 2128-2135.
31. Fazekas, F., et al., *MR signal abnormalities at 1.5 T in Alzheimer's dementia and normal aging*. AJR Am J Roentgenol, 1987. **149**(2): p. 351-6.
32. Andere, A., et al., *Volumetric White Matter Hyperintensity Ranges Correspond to Fazekas Scores on Brain MRI*. Journal of Stroke and Cerebrovascular Diseases, 2022. **31**(4): p. 106333.
33. Charidimou, A., et al., *MRI-visible perivascular spaces in cerebral amyloid angiopathy and hypertensive arteriopathy*. Neurology, 2017. **88**(12): p. 1157-1164.
34. Fotiadis, P., et al., *Cortical atrophy in patients with cerebral amyloid angiopathy: a case-control study*. Lancet Neurol, 2016. **15**(8): p. 811-819.

35. Subotic, A., et al., *Cortical Thickness and Its Association with Clinical Cognitive and Neuroimaging Markers in Cerebral Amyloid Angiopathy*. Journal of Alzheimer's disease : JAD, 2021. **81**(4): p. 1663-1671.
36. Wermer, M.J.H. and S.M. Greenberg, *The growing clinical spectrum of cerebral amyloid angiopathy*. Current Opinion in Neurology, 2018. **31**(1): p. 28-35.
37. Reijmer, Y.D., et al., *Relationship between white matter connectivity loss and cortical thinning in cerebral amyloid angiopathy*. Human brain mapping, 2017. **38**(7): p. 3723-3731.
38. Switzer, A.R., et al., *Longitudinal decrease in blood oxygenation level dependent response in cerebral amyloid angiopathy*. NeuroImage. Clinical, 2016. **11**: p. 461-467.
39. Dumas, A., et al., *Functional MRI Detection of Vascular Reactivity in Cerebral Amyloid Angiopathy*. Annals of neurology, 2012. **72**(1): p. 76-81.
40. Smith, E.E., et al., *Impaired visual evoked flow velocity response in cerebral amyloid angiopathy*. Neurology, 2008. **71**(18): p. 1424-30.
41. Alsop, D.C., et al., *Recommended implementation of arterial spin-labeled perfusion MRI for clinical applications: A consensus of the ISMRM perfusion study group and the European consortium for ASL in dementia*. Magn Reson Med, 2015. **73**(1): p. 102-16.
42. Pauling, L. and C.D. Coryell, *The Magnetic Properties and Structure of Hemoglobin, Oxyhemoglobin and Carbonmonoxyhemoglobin*. Proc Natl Acad Sci U S A, 1936. **22**(4): p. 210-6.
43. Lecrux, C. and E. Hamel, *The neurovascular unit in brain function and disease*. Acta Physiol (Oxf), 2011. **203**(1): p. 47-59.
44. Matthews, P.M. and P. Jezzard, *Functional magnetic resonance imaging*. Journal of Neurology, Neurosurgery & Psychiatry, 2004. **75**(1): p. 6.
45. Buxton, R.B., E.C. Wong, and L.R. Frank, *Dynamics of blood flow and oxygenation changes during brain activation: the balloon model*. Magn Reson Med, 1998. **39**(6): p. 855-64.
46. van Dijk, S.E., et al., *Aging Effect, Reproducibility, and Test-Retest Reliability of a New Cerebral Amyloid Angiopathy MRI Severity Marker-Cerebrovascular Reactivity to Visual Stimulation*. J Magn Reson Imaging, 2022.
47. van Opstal, A.M., et al., *Cerebrovascular function in pre-symptomatic and symptomatic individuals with hereditary cerebral amyloid angiopathy: a case-control study*. The Lancet. Neurology, 2017. **16**(2): p. 115-122.
48. Thal, D.R., et al., *Two types of sporadic cerebral amyloid angiopathy*. J Neuropathol Exp Neurol, 2002. **61**(3): p. 282-93.
49. Bouvy, W.H., et al., *Abnormalities of Cerebral Deep Medullary Veins on 7 Tesla MRI in Amnesic Mild Cognitive Impairment and Early Alzheimer's Disease: A Pilot Study*. J Alzheimers Dis, 2017. **57**(3): p. 705-710.

Chapter 2

On the ability to exploit signal fluctuations in pseudocontinuous Arterial Spin Labeling for inferring the major flow territories from a traditional perfusion scan

T.W. van Harten, O. Dzyubachyk, R.P.H. Bokkers, M.J.H. Wermer, M.J.P. van Osch

This chapter has been published Neuroimage 2021 Apr 15;230:117813. doi: 10.1016/j.neuroimage.2021.117813.

ABSTRACT

In arterial spin labeling (ASL) a magnetic label is applied to the flowing blood in feeding arteries allowing depiction of cerebral perfusion maps. The labeling efficiency depends, however, on blood velocity and local field inhomogeneities and is, therefore, not constant over time. In this work, we investigate the ability of statistical methods used in functional connectivity research to infer flow territory information from traditional pseudo-continuous ASL (pCASL) scans by exploiting artery-specific signal fluctuations. By applying an additional gradient during labeling the minimum amount of signal fluctuation that allows discrimination of the main flow territories is determined. The following three approaches were tested for their performance on inferring the large vessel flow territories of the brain: a general linear model (GLM), an independent component analysis (ICA) and t-stochastic neighbor embedding. Furthermore, to investigate the effect of large vessel pathology, standard ASL scans of three patients with a unilateral stenosis (>70%) of one of the internal carotid arteries were retrospectively analyzed using ICA and t-SNE. Our results suggest that the amount of natural-occurring variation in labeling efficiency is insufficient to determine large vessel flow territories. When applying additional vessel-encoded gradients these methods are able to distinguish flow territories from one another, but this would result in approximately 8.5% lower perfusion signal and thus also a reduction in SNR of the same magnitude.

1. Introduction

pCASL is a readily available non-invasive technique for perfusion imaging that can be used in a clinical setting [1], for clinical research, as well as for neuroscience applications, such as identification of neuronal networks [2]. By applying vessel

encoding, pCASL can also be used to infer flow territories of arteries [3-5]. Whereas current clinical practice relies on general atlases of typical flow territories, information on the layout of the actual flow territories in an individual patient can be highly valuable in several clinical settings, such as for risk assessment and guidance of revascularization therapy in patients suffering from stroke, as well as for explaining differences in patient outcome [6-8].

Small changes in ASL signal over time allow for identification of resting state networks [2]. One could hypothesize that small, artery specific signal fluctuations in pCASL-signal would allow to also infer the flow territories from a traditional perfusion scan. Such signal changes could both arise from physiological fluctuations within a flow territory, as well as from the acquisition process. For example, the labeling efficiency of pCASL is known to be dependent on velocity of arterial blood and off-resonance effects at the labeling location [9-11]. Any variation in labeling efficiency of a particular artery will affect the ASL-signal of the complete associated flow territory, and, differences between arteries could therefore provide a source of flow-territory-specific signal fluctuations that could be exploited for identifying these territories. Similarly, dynamic changes in arterial transport times could also induce flow-territory-specific fluctuations. [12, 13] This could be a way of acquiring flow territory information for free from a 2D-multi-slice pCASL scan, which normally has many (>25) repeated measurements. When natural occurring fluctuations would be sufficient, this would enable a penalty-free approach for obtaining combined cerebral blood flow (CBF) and flow territory information from a single scan. Alternatively, small labeling-efficiency fluctuations could be inserted into the sequence, which would only result in a minor SNR penalty on the perfusion scan. To assess the feasibility of such an approach, we analyzed ASL scans by several techniques traditionally used in functional connectivity research. Moreover, by incorporating different levels of signal fluctuations into pCASL scans, it was determined what level of signal variations is needed to allow assessment of flow territory information. Vessel-encoded signal

fluctuations were introduced by deliberately changing the labeling efficiency of the left and right internal carotid artery by adding a vessel-encoding gradient [3, 4] with variable strength into a normal pCASL sequence. The three methods tested are already commonly used in functional MRI analyses: 1) general linear model (GLM) based approach, as generally used in task based fMRI [14]; The GLM based approach was selected to represent the best-case scenario: by including the timing of the inserted signal fluctuations into the analysis an upper-limit of performance of flow-territory extraction can be established. 2) independent component analysis (ICA), as generally used in resting state fMRI [2]; and 3) t-stochastic neighbour embedding (t-SNE), a clustering method with broad applications in image processing [15]. ICA and t-SNE are input naïve approaches as they do not rely on the knowledge of the timing of signal fluctuations and could, therefore, also be used for traditional pCASL data when no additional signal fluctuations are inserted.. The ICA was performed both on the original data, as well as on the data after blurring with a 10 mm kernel. The addition of the 10 mm blurred version was based on the hypothesis that the relatively low SNR of single average ASL images would hamper identification of flow territory specific fluctuations. Since such fluctuations would per definition be spatially coherent, some blurring could help in identifying flow territories, albeit at a loss of effective spatial resolution.

Finally, to investigate this approach in patient cases, we retrospectively analyzed pCASL scans of patients with an internal carotid stenosis and compared the outcome with the flow territories obtained from a separately acquired vessel-encoded pCASL scan. In this proof-of-concept study only the flow territories of the right and left internal carotid artery were considered.

2. Methods

pCASL scans with different levels of vessel-encoded signal fluctuations were acquired in 5 volunteers with traditional flow territory scans obtained as ground

truth. The scans were subsequently analyzed using three different statistical methods: a general linear model (GLM), an independent component analysis (ICA), and a t-Stochastic neighbor embedding (t-SNE) approach. The FMRIB's Software Library (FSL, www.fmrib.ox.ac.uk/fsl) was used for the GLM and ICA approaches, while the t-SNE was performed using an inhouse developed pipeline, as further described in *Applied Models*. The pCASL scans acquired without a vessel-encoding gradient were analyzed only using the ICA and t-SNE methods, since the GLM-approach relies on prior knowledge on the timing of the fluctuations in labeling efficiency, which is not available when there is no prior knowledge on the pattern of signal fluctuations.

2.1 Participants

This research has been performed in accordance with the declaration of Helsinki. Written informed consent was obtained from all participants. Five healthy participants (mean age 30.4 ± 7.6 , male/female = 4/1) were recruited for this study. Since one might expect that patients show larger natural occurring fluctuations than healthy participants, data from three patients (mean age: 69.7 ± 9.5 , male/female = 2/1) with a recently symptomatic unilateral internal carotid stenosis (>50% occluded) were retrospectively analyzed.

2.2 Scans

All healthy participants were scanned on a 3 Tesla MRI scanner (Achieva, Philips Medical Systems, the Netherlands) using a protocol containing a standard background suppressed pCASL (TR/TE 4290/16 ms, FOV $240 \times 240 \times 119 \text{ mm}^3$ matrix size 80×80 , 17 slices with no interslice gap resulting in a voxel-size of $3 \times 3 \times 7 \text{ mm}^3$, labeling duration = 1800 ms, post-labeling delay (PLD) of 1800 ms with 35 repetitions resulting in a total scan duration of 5 min 09 s), a time-of-flight angiogram of the labeling plane (TR/TE 35/3.5 ms, flip angle 60° , 9 slices with a slice thickness of 3 mm, FOV $230 \times 230 \times 19 \text{ mm}^3$, matrix size 192×96 , resulting in a

pixel-size of $1.2 \times 2.4 \text{ mm}^2$ and a scan duration of 31 s), a vessel-encoded flow territory mapping scan, considered as the gold standard, with similar settings as the standard pCASL scan, but acquired in 5 conditions: 1) label, 2) control, 3) vessel-encoding in the RL direction with a distance of 50 mm between full label and control, 4) and 5) two vessel-encodings in the AP direction with a distance of 15 mm with the last condition shifted 7.5 mm compared to the first [4] (12 averages, resulting in a scan duration of 4 min 39 s) The vessel encoding distance is defined as the distance between the location where optimal labelling occurs (always planned to be on top of an internal carotid artery) and the location where the control condition is achieved, an equivalent definition is the distance over which a π phase will occur due to the vessel encoding gradient. E.g. a vessel encoding distance of 50mm (average distance between internal carotid arteries) would have the targeted internal carotid artery in label condition while the contralateral artery would be in control condition. The protocol also included a range of pCASL scans with an additional vessel-selective gradient in the left-right direction with varying gradient strengths according to a predefined scheme (see Figure 1), whose scan parameters were otherwise identical to the standard pCASL scan. The varying gradient strength values were chosen to create artery-specific signal fluctuations by having maximal labelling efficiency at the location of one internal carotid artery, while the contralateral internal carotid artery will experience sub-optimal labelling. The phases of the pCASL labeling pulses were adapted to ensure that the optimal labeling condition was achieved on top of one of the internal carotid arteries. By changing the area under the vessel-encoding gradient by adjusting its amplitude, the spatial frequency of the induced label efficiency changes in the direction of the vessel-encoding gradient can be controlled. With optimal labeling in one internal carotid artery, the contralateral internal carotid artery will experience off-resonance effects and thus a lower labeling efficiency. The magnitude of the off-resonance effects will determine the extent of the labeling efficiency decrease. The term “vessel-encoding distance” will be used for the distance resulting in π phase

shift during the interpulse interval of the pCASL train. At this distance from the internal carotid artery with optimal labeling, the control and label condition will be switched compared to the targeted vessel..

The position of optimal labelling is switched to the contralateral internal carotid artery after acquisition of each label control pair, resulting in a switch in signal intensity of the flow territories after every label/control pair. This was done in order to create temporal fluctuations in labeling efficiency for both internal carotid arteries, while providing a normal perfusion map when averaging all data, albeit with lower mean labeling efficiency.

The data from patients with a unilateral internal carotid artery stenosis was acquired as part of a previously published study. [16] All patients had suffered a transient ischemic attack (TIA) or non-disabling ischemic stroke ipsilateral to the internal carotid artery stenosis. The protocol included standard pCASL (TR/TE 4000/14 ms, FOV 240×140 mm², matrix size 89×79, 17 slices with no interslice gap resulting in a voxel-size of 3×3×7 mm³, labeling duration = 1650 ms, post-labeling delay (PLD) of 1525 ms with 38 repetitions resulting in a total scan duration of 5 min 26 s), and a planning-free flow territory mapping scan with the same settings.

2.2 Post-processing

First, the flow territories of both internal carotid arteries and the basilar artery were determined by processing vessel-encoded flow territory mapping scans, using previously described methods [4]. The effect of the applied vessel-encoding gradient on the labeling efficiency was quantified for each flow territory as the mean signal intensity after subtracting and averaging the images with sub-optimal conditions due to the presence of the vessel-encoding gradient ($SI_{\text{off-resonance}}$) from the images with the artery in perfect labeling condition (SI_{full}); and subsequently normalizing by the mean signal intensity as measured by the standard pCASL scan (SI_{pCASL}):

$$\text{Relative signal fluctuations} = (SI_{\text{full}} - SI_{\text{off-resonance}}) / SI_{\text{pCASL}} * 100\%$$

[Eq. 1]

2.3 Applied models

Four different approaches were selected to extract the flow territories based upon flow-territory-specific signal fluctuations.

Data preprocessing for the GLM and ICA based methods was performed using FSL (FMRIB's Software Library, www.fmrib.ox.ac.uk/fsl). The following preprocessing was applied: motion correction using MCFLIRT; non-brain removal using BET [17]; grand-mean intensity normalisation of the entire 4D dataset by a single multiplicative factor; high-pass temporal filtering (Gaussian-weighted least-squares straight line fitting, with sigma=50.0 s for both GLM and ICA).

2.3.1 General Linear model

In the GLM the applied labeling fluctuations were introduced into the model as an explanatory variable. Because the multiple regression of the GLM requires such prior information, it is not possible to do this analysis on scans where no intentional signal fluctuations were inserted by means of additional gradients switched on in the labeling plane. The general linear model was carried out using FEAT (FMRI Expert Analysis Tool) Version 6.00, part of FSL (FMRIB's Software Library, www.fmrib.ox.ac.uk/fsl). The time-series statistical analysis was carried out using FILM with local autocorrelation correction. Only lower level analysis was applied as this was ran on a single 4-D MRI experiment. T-statistic maps resulting from this analysis were used without thresholding or clustering.

2.3.2 Independent component analysis

ICA analysis was carried out using Probabilistic Independent Component Analysis implemented in MELODIC (Multivariate Exploratory Linear Decomposition into Independent Components) Version 3.15, part of FSL. In summary, pre-processed data were whitened and projected into a multi-dimensional subspace using a probabilistic Principal Component Analysis where the number of dimensions was estimated using the Laplace approximation to the Bayesian evidence of the model order [18, 19]. The whitened observations were subsequently decomposed into sets of vectors that describe signal variation across the temporal domain (time-courses) and across the spatial domain (maps) by optimising for non-Gaussian spatial source distributions using a fixed-point iteration technique [20]. Estimated component maps were divided by the standard deviation of the residual noise and thresholded by fitting a mixture model to the histogram of intensity values [21]. From the identified components, the best fitting was selected based upon the largest difference between left and right intracranial region defined by a left and right hemisphere mask containing intracranial voxels separated by a (mid-)sagittal plane crossing through the genu and splenum of the corpus callosum. The component with the highest corroboration with the corresponding hemisphere mask was used as outcome for that flow territory for further evaluation.

Finally, the complete MELODIC was repeated after blurring the input data with a 10 mm Gaussian kernel to minimize the effect of voxel-level inconsistencies.

2.3.3 t-Distributed Stochastic Neighbor Embedding

Since we are only interested in differentiating left and right flow-territories, which is effectively a 1D problem, we set the target embedding dimensionality to unity. The ASL difference volumes were reduced in the time dimension to a single value by applying the Hierarchical Stochastic Neighbor Embedding (HSNE) algorithm [22]. HSNE is a modification of the classical t-SNE algorithm, which was proven to better preserve the data structure during the embedding process [23]. Full embedding of

each of the data sets was performed as a hierarchical process with 4 levels. Drilling down into the next level of the hierarchy was performed after convergence (defined as the maximum number of iterations) of the embedding on the current level. All the landmarks available on the current level were used for this. Initial positions of the lower-level landmarks were calculated by interpolating current positions of the corresponding higher-level landmarks.

2.4 Validation

The robustness of the methods was tested via receiver operating characteristic (ROC) curves, only including intracranial voxels that show sufficient ASL-signal. Moreover, since signal fluctuations were only introduced in the internal carotid arteries, voxels that are part of the posterior circulation territory as determined from the flow territory maps were excluded. Sufficient ASL-signal was operationalized, as the lower limit of values within the gray matter, which was determined via a consensus value over all participants and was kept constant for all scans. Voxels with lower signal, such as those in the white matter, were excluded from the analysis, because they could not be classified on the flow territory mapping data and are, therefore, not a correct reflection of the performance of the different approaches, and would introduce bias in the evaluation procedure.

The z-statistics map of the GLM-based approach, the IC-map of the ICA-based approaches, as well as the distance maps from the t-SNE-based approach were projected on the ground truth flow territory maps. ROC curves were generated by thresholding the statistical maps reflecting the z-score/distance to yield binary segmentations and subsequently calculating the overlap with the flow territory map. This analysis was done with an in-house developed pipeline combining MeVisLab 3.2 and Matlab 2016a.

3. Results

The vessel-encoding gradients we introduced did lead to the intended changes in ASL signal fluctuation. These fluctuations were directly proportional to the gradient area of the employed vessel-encoding gradients.. In *Figure 1* the effect of vessel-encoding gradient-area on the ASL-images is shown for one subject. For displaying the magnitude of the induced signal fluctuations, the ASL-scans were split into those measurements for which the left internal carotid artery was optimally labeled and those that targeted the right internal carotid artery. From these images we can conclude that the proposed approach indeed leads to a tunable magnitude of labeling efficiency fluctuations on top of a normal ASL-scan. The chosen strength values for the vessel-encoding lead to fluctuations between 3% and 150%.

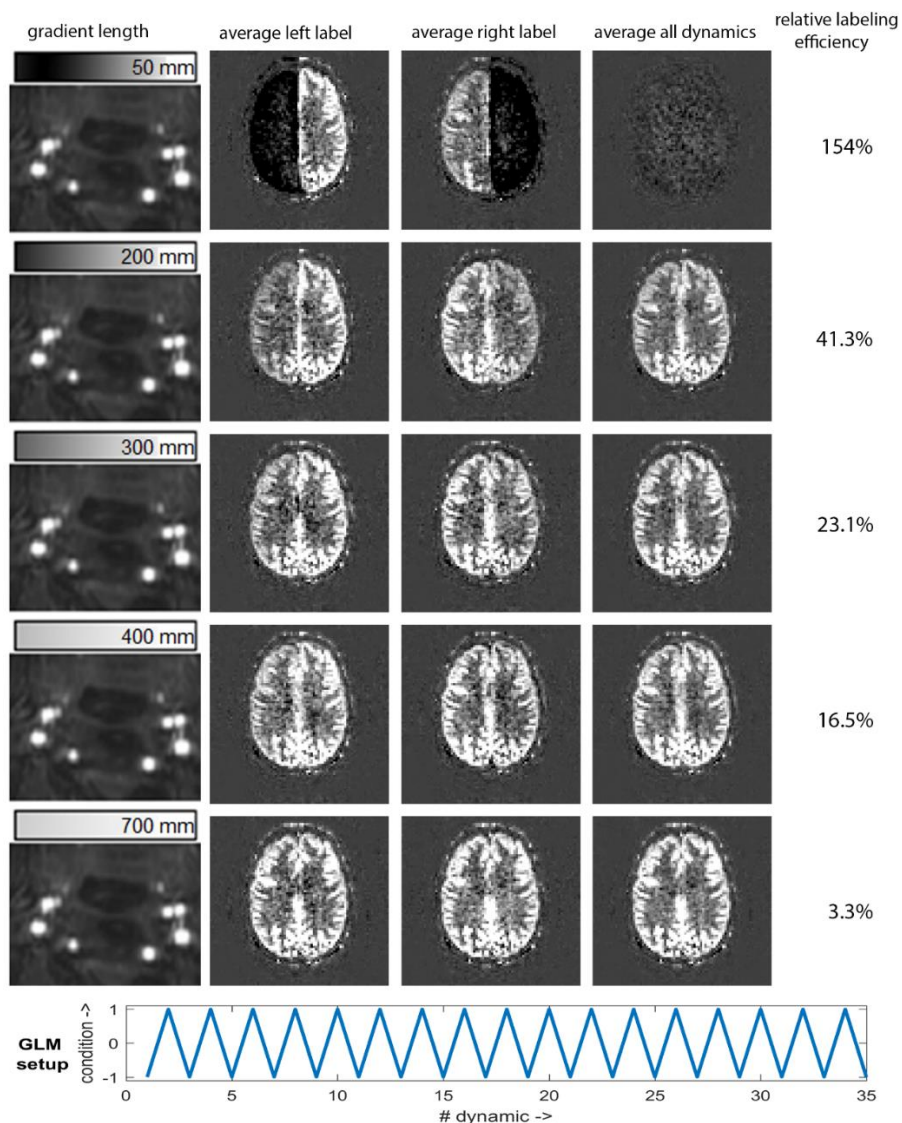


Figure 4: The effect of the area of the vessel-encoding gradient on the ASL-signal in an example subject; with amplitude of the vessel-encoding gradient varying from strong (top) to weak (bottom). The first column shows Time-Of-Flight angiography of the labeling plane with the bar above indicating how the vessel-encoding gradient affects the labeling efficiency: white is optimal labeling and black the location where an additional π phase shift occurs during the pulse-interval, which will result into opposite behavior during labeling (i.e. control during the label, and label during the control condition). The numbers reflect the vessel-encoding distance. Since optimal labeling is switched between the left to the right internal carotid artery after every label-control pair, the data were split into two. Columns

two and three show the resulting mean ASL subtraction image when the left or right internal carotid artery was labeled optimally. The final column shows the mean signal intensity over the complete pCASL scans, i.e. the average of the second and third column, showing a homogenous image, except for the first row that shows signal cancelations. The percentages on the right indicate the relative signal fluctuations for the images shown in this figure, as calculated by [EQ 1]. The bottom row shows the design for GLM setup.

The averaged effect over all participants of the area under the vessel-encoding gradient on the relative signal fluctuations is shown in *Figure 2*, showcasing the direct relationship between the introduced off-resonance effects in the labeling plane and ASL-signal fluctuations downstream within the flow territories of these arteries. The smaller the area under the vessel-encoding gradient, the smaller the off-resonance effects in the contralateral internal carotid artery, and the smaller the difference in relative signal fluctuations between the two flow territories of these arteries.

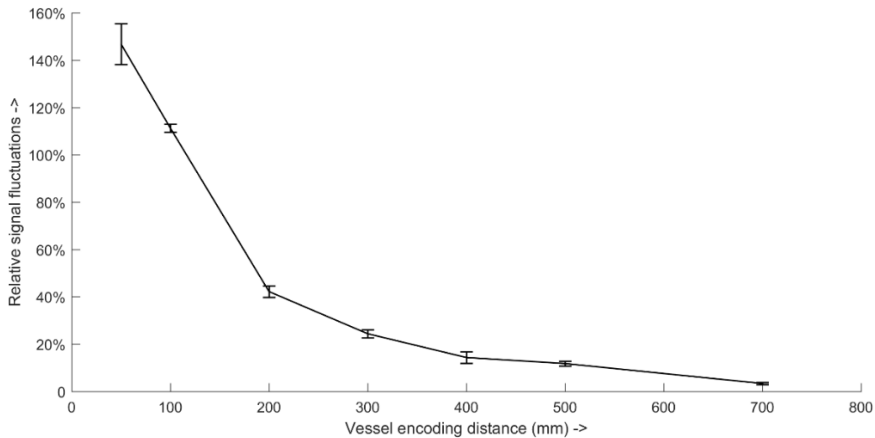


Figure 2: Mean relative signal fluctuations as a function of vessel-encoding distance; (distance resulting in π phase shift during the interpulse interval of the pCASL train) with standard error of the mean for all participants.

Figure 3 shows how well the four different post-processing approaches could detect the underlying flow territories for a single example subject (same subject as *Figure 1*). It can be seen that, as the strength of the vessel-encoding gradient is strong enough, all 3 methods can identify the flow territory correctly, but

specificity and sensitivity vary between the four approaches, which is also reflected in the ROC curves displayed on the right.

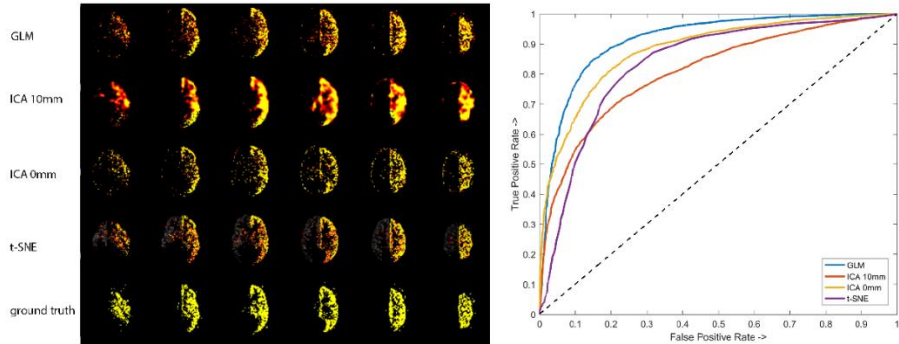


Figure 5: Post-processing approaches and their ability to detect flow territories; example of how well the four post-processing approaches can detect the flow territories on the data from the second row of Figure 1, i.e. a vessel-encoding distance of 200 mm, corresponding to a relative signal fluctuation of 41.3%. From top to bottom: GLM, ICA with 10 mm blurring, ICA without blurring, t-SNE, and flow territory mapping. In the right panel, the ROC are shown for the same data. The dashed line indicates a hypothetical 50/50 random chance classifier.

Figure 4 summarizes the mean and standard deviation of the area under the ROC curves over all 5 participants, over all labeling conditions. The averages of the area under the curve of the ROC curves show that the GLM-based approach does outperform the other methods in this dataset, which was expected because the GLM exploits prior knowledge of the applied labeling fluctuations. In the scans with the strongest signal fluctuations the ICA was found to split flow territories in multiple components. Only the component with the strongest difference between left and right was used in further analyses. Furthermore, for most levels of relative signal fluctuations, blurring improved the ability of the ICA-based approach to differentiate between flow territories, although this was not the case for all

participants or for all conditions. When the differences in fluctuations were especially large (>200 mm gradient length) or small (<500 mm gradient length), there was an agreement between the blurring and non-blurring results, while for conditions between these two extremes, better results were obtained when blurring the input data.

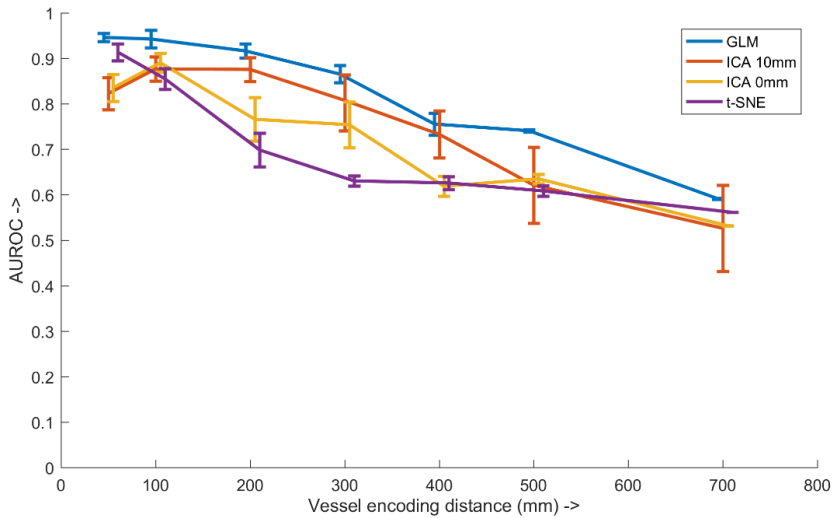


Figure 6: Mean area under the ROC-curve for each method as a function of the vessel encoding distance; error-bars indicate standard error of the mean. A small offset in the x-direction was introduced for each method for illustration purposes.

The ICA as well as the t-SNE analysis on the pCASL data without imputed signal fluctuations did not yield convincing flow territory information, in either healthy volunteers nor the patients with internal carotid artery stenosis (*Figure 5*).

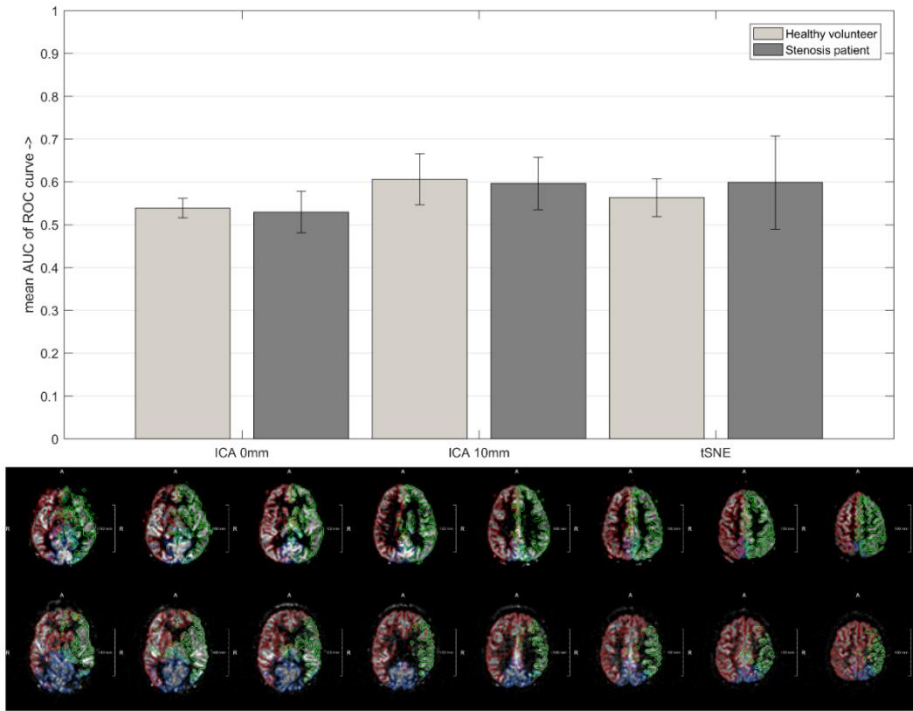


Figure 7: Mean area under the ROC-curve for each method tested on standard pCASL scans; all methods were slightly better than a 50/50 chance classifier but unable to determine flow territories. There was no significant difference between healthy volunteers and patients with a unilateral stenosis in the internal carotid artery. Error bars indicate standard error of the mean.

4. Discussion

The main findings of this study are threefold. First, we are able to report that with the introduction of weak off-resonance effects by means of a vessel-encoding gradient it becomes possible to determine flow territories using a GLM statistical analysis. The performance becomes weaker in robustness when the introduced fluctuations are smaller or when “naive methods” are employed, i.e. when no prior information on the timing of the labeling efficiency fluctuations is exploited in the statistical model. We observe a statistically significant higher ROC for GLM, but this

should be interpreted with care due to the very small sample size of our study. Second, when maintaining a minimum of 0.85 for the area under the ROC-curve to reflect correct performance, the ICA and t-SNE approaches lost their ability to differentiate between left and right flow territory at a relative signal fluctuations of 41.3% and 64.1%, respectively. Third, it was not feasible to determine reliable flow territory information from traditional pCASL scans in healthy volunteers or patients with >70% unilateral carotid stenosis using ICA or t-SNE analysis, i.e. natural occurring fluctuations in labeling efficiency in the temporal domain were insufficient to yield reliable flow territory information.

Coherent fluctuations within a flow territory were found to be too small to identify them from conventional pCASL scans, whereas fluctuations caused by hemodynamic fluctuations were previously found to allow detection of resting state networks, albeit at group level[2]. This can be considered a surprising finding: coherent hemodynamic fluctuations as observed in resting-state fMRI/ASL have a more substantial influence than any flow-territory specific hemodynamic changes or off-resonance effects.. Correct performance of our applied post-processing methodology was proven by showing that imputed labeling efficiency fluctuations did allow differentiation between the left and right internal carotid artery territory. One explanation might be that fluctuations in labeling efficiency are mainly caused by global systemic processes. For example, heart rate or respiratory variations will affect all brain-feedings arteries territories similarly, just as fluctuations in end-tidal CO₂ will have a global rather than an artery specific effect. The impact of breathing on the labeling efficiency can be estimated from previously reported resonance frequency changes [24, 25]. For example, Birn et al. [26, 27] showed that off-resonance frequencies during swallowing and speech reach up to -9.6 Hz at 3 Tesla in the inferior part of the brain, which would result in a phase shift of 4.14 degrees during the 1.2 ms between the pCASL pulses, i.e. a rather limited effect although the effect at the labeling plane could be expected to be a bit more pronounced.

When 16.5% or stronger fluctuations of ASL-signal were imputed on the perfusion signal, reliable discrimination between the right and left internal carotid artery flow territory could be achieved by using the GLM approach. These fluctuations are larger than the fluctuations described earlier induced by respiration and other physiology [26, 27]. The presence of such a gradient implies that the mean labeling efficiency will be 8.3% lower over the whole ASL-acquisition (labeling is only decreased in half of the measurements), which translates directly to 8.3% lower SNR of the perfusion map when compared to an ASL scan with the same scan time. This seems to be on the border of what could be considered acceptable in a clinical setting to allow combined flow territory and perfusion imaging. Also, slight interindividual differences in location of the arteries could affect the induced labeling efficiency reduction between the left and right internal carotid artery, when relying on population averaged settings for the planning of the location of perfect labeling conditions. This would imply that the average perfusion map could become asymmetrical, which might affect clinical interpretation, although also in normal pCASL scans labeling efficiency differences between arteries have been reported [28].

Other approaches for improving vessel encoded scans involve applying novel acquisition techniques, such as a different labeling scheme to reduce scan time while maintaining sufficient SNR for reliable flow territory determination [29, 30]; and approaches to calculate optimal labeling schemes to further improve SNR [31]. These approaches, however, require specific planning approaches and may therefore introduce differences in performance between technicians. Furthermore, these approaches would not be able to extract any additional flow territory information from traditional pCASL scans.

In this study, four different post-processing approaches were tested in their ability to determine flow territory information from small fluctuations in labeling efficiency in the feeding arteries. Based on observed trends in data of this study

the most robust method appears to be a GLM-based approach. This is caused by the prior information that is fed into the model, thereby increasing the statistical power of the model. The relative performance of the naïve methods seems at first glance more difficult to describe, since t-SNE outperforms both ICA-based methods on the biggest and the smallest amount of signal fluctuations, whereas in-between the ICA-based approaches perform better. However, for the strongest signal fluctuations, the ICA was found to split flow territories in multiple components, whereas for the validation only a single component was included. This explains the poorer performance of the ICA-methods for the data with the largest signal fluctuations.

We hypothesized that patients with large vessel disease could show more prominent differences in ASL-signal fluctuations between flow territories than healthy volunteers. However, in the three patients that we included in this study, the ICA and t-SNE analyses did not allow trustworthy determination of the flow territories. Apparently, also in carotid stenotic disease patients, fluctuations in ASL-signal are too correlated between flow territories or, in general, too small to allow differentiation.

A limitation of our experimental approach is that we only focused on differentiation between the left and right internal carotid artery territory and ignored the posterior circulation. This approach was taken for practical reasons: we aimed at primarily demonstrating the possibilities for the main internal carotid artery territories and would expand our efforts to the three regions when successful. Moreover, the distance between the two internal carotid arteries is larger than the distance between the anterior and posterior circulation, which could result in larger difference in fluctuations caused by off-resonance effects, i.e. in data without additional vessel-encoding gradients. To be able to discriminate the posterior from the anterior circulation, stronger gradients should be employed than used in the current studies, since the distance between arteries is smaller.

Discrimination of vessels distanced more than 5 mm could be achieved, although planning the location of optimal labelling would require an angiographic scout and careful planning. In the data without additional flow-encoding gradients, we also tried to discriminate the anterior from the posterior circulation, but this did not provide satisfactory results by either ICA or t-SNE analysis of the ASL-data. Apparently, the difference in hemodynamics between the anterior and posterior circulation does not translate to flow-territory specific fluctuations of the ASL-signal over different repeated measurements.

5. Conclusions

Signal fluctuations present in standard pCASL scans due to fluctuations in off resonance effects in the labeling plane or transit time are not sufficient for extracting flow territory mapping information from standard pCASL scans when using ICA or t-SNE, neither in healthy participants nor in patients with severe (>70%) unilateral internal carotid artery stenosis. When applying additional vessel-encoded gradients these methods are able to distinguish flow territories from one another, but this would result in approximately 8.5% lower perfusion signal and thus also a reduction in SNR of the same magnitude.

Acknowledgements

The authors would like to thank Sophie Schmidt, Wouter Teeuwisse and Annemarieke van Opstal for their help acquiring scan data.

Funding

This research has been made possible by the Dutch Heart Foundation and the Netherlands Organisation for Scientific Research (NWO), as part of their joint strategic research programme: "Earlier recognition of cardiovascular diseases".

This project is partially financed by the PPP Allowance made available by Top Sector Life Sciences & Health to the Dutch Heart foundation to stimulate public-private partnerships. This research was also supported by the EU under the Horizon2020 program (project: CDS-QUAMRI), and the CAVIA project (nr. 733050202), which has been made possible by ZonMW

6. References

1. Alsop, D.C., et al., *Recommended implementation of arterial spin-labeled perfusion MRI for clinical applications: A consensus of the ISMRM perfusion study group and the European consortium for ASL in dementia*. Magn Reson Med, 2015. **73**(1): p. 102-16.
2. Dai, W., et al., *Quantifying fluctuations of resting state networks using arterial spin labeling perfusion MRI*. J Cereb Blood Flow Metab, 2016. **36**(3): p. 463-73.
3. Wong, E.C., *Vessel-encoded arterial spin-labeling using pseudocontinuous tagging*. Magn Reson Med, 2007. **58**(6): p. 1086-91.
4. Gevers, S., et al., *Robustness and reproducibility of flow territories defined by planning-free vessel-encoded pseudocontinuous arterial spin-labeling*. AJNR Am J Neuroradiol, 2012. **33**(2): p. E21-5.
5. Wong, E.C. and J. Guo, *Blind detection of vascular sources and territories using random vessel encoded arterial spin labeling*. Magnetic Resonance Materials in Physics, Biology and Medicine, 2012. **25**(2): p. 95-101.
6. Hendrikse, J., et al., *Relation between cerebral perfusion territories and location of cerebral infarcts*. Stroke, 2009. **40**(5): p. 1617-22.
7. van Laar, P.J., J. van der Grond, and J. Hendrikse, *Brain perfusion territory imaging: methods and clinical applications of selective arterial spin-labeling MR imaging*. Radiology, 2008. **246**(2): p. 354-64.
8. Hartkamp, N.S., et al., *Misinterpretation of ischaemic infarct location in relationship to the cerebrovascular territories*. 2016. **87**(10): p. 1084-1090.
9. Aslan, S., et al., *Estimation of labeling efficiency in pseudocontinuous arterial spin labeling*. Magn Reson Med, 2010. **63**(3): p. 765-71.
10. Wu, W.C., et al., *A theoretical and experimental investigation of the tagging efficiency of pseudocontinuous arterial spin labeling*. Magn Reson Med, 2007. **58**(5): p. 1020-7.
11. Wu, W.-C., et al., *Pseudocontinuous arterial spin labeling perfusion magnetic resonance imaging—A normative study of reproducibility in the human brain*. NeuroImage, 2011. **56**(3): p. 1244-1250.
12. Verbree, J. and M.J.P. van Osch, *Influence of the cardiac cycle on pCASL: cardiac triggering of the end-of-labeling*. Magma (New York, N.Y.), 2018. **31**(1): p. 223-233.
13. Qiu, M., et al., *Arterial transit time effects in pulsed arterial spin labeling CBF mapping: insight from a PET and MR study in normal human subjects*. Magnetic resonance in medicine, 2010. **63**(2): p. 374-384.
14. Yerys, B.E., et al., *Arterial spin labeling provides a reliable neurobiological marker of autism spectrum disorder*. J Neurodev Disord, 2018. **10**(1): p. 32.
15. Hu, Y., et al., *T-distribution stochastic neighbor embedding for fine brain functional parcellation on rs-fMRI*. Brain Research Bulletin, 2020. **162**: p. 199-207.

16. Hartkamp, N.S., et al., *Distribution of cerebral blood flow in the caudate nucleus, lentiform nucleus and thalamus in patients with carotid artery stenosis*. European Radiology, 2011. **21**(4): p. 875-881.
17. Smith, S.M., *Fast robust automated brain extraction*. Hum Brain Mapp, 2002. **17**(3): p. 143-55.
18. Minka, T.P., *Automatic choice of dimensionality for PCA*. Technical Report 514, MIT Media Lab Vision and Modeling Group, 2000.
19. Beckmann, C., J. Noble, and S. Smith. *Investigating the intrinsic dimensionality of fMRI data for ICA*. 2001.
20. Hyvarinen, A., *Fast and robust fixed-point algorithms for independent component analysis*. IEEE Transactions on Neural Networks, 1999. **10**(3): p. 626-634.
21. Beckmann, C.F. and S.M. Smith, *Probabilistic independent component analysis for functional magnetic resonance imaging*. IEEE Trans Med Imaging, 2004. **23**(2): p. 137-52.
22. Pezzotti, N., et al., *Hierarchical Stochastic Neighbor Embedding*. 2016. **35**(3): p. 21-30.
23. van der Maaten, L. and G. Hinton, *Visualizing Data using t-SNE*. Journal of Machine Learning Research, 2008. **9**: p. 2579--2605.
24. Versluis, M.J., et al., *Retrospective image correction in the presence of nonlinear temporal magnetic field changes using multichannel navigator echoes*. 2012. **68**(6): p. 1836-1845.
25. Raj, D., A.W. Anderson, and J.C. Gore, *Respiratory effects in human functional magnetic resonance imaging due to bulk susceptibility changes*. Phys Med Biol, 2001. **46**(12): p. 3331-40.
26. Birn, R.M., et al., *Magnetic field changes in the human brain due to swallowing or speaking*. Magn Reson Med, 1998. **40**(1): p. 55-60.
27. Zhao, L., et al., *Improving the robustness of pseudo-continuous arterial spin labeling to off-resonance and pulsatile flow velocity*. Magnetic resonance in medicine, 2017. **78**(4): p. 1342-1351.
28. Chen, Z., et al., *Simultaneous measurement of brain perfusion and labeling efficiency in a single pseudo-continuous arterial spin labeling scan*. Magn Reson Med, 2018. **79**(4): p. 1922-1930.
29. Zimine, I., E.T. Petersen, and X. Golay, *Dual vessel arterial spin labeling scheme for regional perfusion imaging*. Magn Reson Med, 2006. **56**(5): p. 1140-4.
30. Gunther, M., *Efficient visualization of vascular territories in the human brain by cycled arterial spin labeling MRI*. Magn Reson Med, 2006. **56**(3): p. 671-5.
31. Berry, E.S., P. Jezzard, and T.W. Okell, *An Optimized Encoding Scheme for Planning Vessel-Encoded Pseudocontinuous Arterial Spin Labeling*. Magn Reson Med, 2015. **74**(5): p. 1248-56.

Chapter 3

Impact of ROI definition on visual stimulation based cerebral vascular reactivity fMRI with a special focus on applications in Cerebral Amyloid Angiopathy

T.W. van Harten, S. van Rooden, E.A. Koemans, A.M. van Opstal, S.M. Greenberg, J. van der Grond, M.J.H. Wermer, M.J.P. van Osch

This chapter has been published NMR Biomed. 2023 Mar 12;e4916. doi: 10.1002/nbm.4916.

ABSTRACT

Cerebral vascular reactivity quantified using BOLD fMRI in conjuncture with a visual stimulus has been proven to be a potent and early marker for cerebral amyloid angiopathy. This work investigates the influence of different post-processing methods on the outcome of such vascular reactivity measurements. Three methods for defining the region-of-interest (ROI) over which the reactivity is measured, are investigated: structural (transformed V1), functional (template based on the activation of a subset of subjects) and percentile (11.5 cm³ most responding voxels). Evaluation is done both in a test-retest experiment in healthy volunteers (N= 12), as well as in 27 Dutch-type CAA patients and 33 age and sex matched control subjects. The results show that the 3 methods select a different subset of voxels, although all three lead to similar outcome measures in healthy subjects. However, in (severe) pathology the percentile method lead to higher reactivity measures than the other two, due to circular analysis or 'double dipping' by defining a subject-specific ROI based on the strongest responses within each subject. Furthermore, while different voxels are included in the presence of lesions, this does not necessarily result in different outcome measures. In conclusion, to avoid bias created by the method, either a structural or a functional method is recommended. Both of these methods provide similar reactivity measures, although the functional ROI appears to be less reproducible between studies, since slightly different sub-sets of voxels were found to be included. On the other hand, the functional method did include fewer lesion voxels than the structural method.

1. INTRODUCTION

Cerebral vascular reactivity fMRI, the vascular response to a stimulus, is an increasingly recognized marker for several brain diseases [1-3]. One of these diseases is sporadic Cerebral Amyloid Angiopathy (CAA), a major cause of intracerebral hemorrhages (ICH) and cognitive decline in elderly [4-6]. In CAA the protein amyloid-beta accumulates in the vessel wall of leptomeningeal arteries. The current diagnosis of CAA focusses primarily on clinical symptoms combined with hemorrhagic hallmarks on MRI [7, 8]. However, a multitude of ischemic processes are also observed: there is a strong association with cortical thinning [9, 10], white matter hyperintensities, microinfarcts [11] and changes in diffusion tensor measures [12]. Moreover, impaired cerebrovascular function has been proven to be an important hallmark [13-16]. More specifically, in patients with Dutch-type hereditary CAA (D-CAA, also known as Hereditary Cerebral Hemorrhage With Amyloidosis – Dutch type (HCHWA-D)) vascular reactivity has been found to be an early marker, i.e. already showing differences compared to age-matched controls in mutation carriers without prior ICH [17]. Moreover, reactivity decreased over time in (D-)CAA patients in contrast with healthy controls [13, 18, 19]. Therefore, vascular reactivity can be considered a promising marker to monitor CAA progression over time, for example as outcome measure in clinical trials.

When measuring vascular reactivity both the readout as well as the challenge need to be chosen. Blood oxygenation level dependent (BOLD) fMRI is considered to be a powerful readout to facilitate the quantification of vascular reactivity. The BOLD fMRI signal is, however, a very complicated type of contrast, thought to be a combination of changes in oxygen consumption, regional blood flow and regional blood volume. To map full brain vascular reactivity with MRI, the most commonly used challenges are CO₂-based approaches, such as carbogen breathing or breath-hold experiments, or less commonly administration of acetazolamide [20].

Previous works in CO₂-based approaches in CAA found a diminished vascular reactivity as measured by BOLD fMRI, with a stronger preference in the occipital region of the brain [21]. Furthermore, while evoked potentials remained unchanged, the BOLD response was affected in CAA patients, suggesting a more important contribution of vascular reactivity than neuronal activity in the observed BOLD-changes [22].

To measure vasoreactivity in the field of CAA, most studies employ a visual stimulus and monitor the hemodynamic response to that stimulus in the visual cortex via BOLD fMRI [13-15, 17-19, 23]. This relatively simple approach is chosen as CAA pathology appears to have an occipital preference, the robustness of the visual cortex' hemodynamic response to this stimulus and the non-invasive nature of the administration of such a stimulus. As the small penetrating arteries in the brain are affected in CAA, the changes in BOLD signal change are hypothesized as a surrogate marker for vascular reactivity for subsequent quantification. In such functional MRI experiments an ROI is determined containing voxels within the activated region and subsequently response characteristics, such as the amplitude, time-to-peak and time-to-baseline, are used as outcome measures. However, little consistency exists in literature on how to define this ROI, whereas measures like the amplitude, are crucially dependent on such a definition. Roughly two categories of ROI definitions can be discerned: anatomical and functional. Anatomical ROI definitions rely on atlas-based or group-wise defined ROIs that are registered onto the BOLD-scan of a subject for extraction of the response signals. Functional ROI definitions rely on a two-step approach: in the first step it is determined what voxels are activated by the stimulus and subsequently in the second step the ROI is created based upon all or a subset (like the maximally activated voxels) of the activated voxels.

When considering the use of vascular reactivity as outcome marker for clinical treatment studies in CAA [24], it is important to recognize that consistent ROI-

definitions are essential. When used in patients, the presence of pathology, like hemorrhages in CAA, can be expected and the ROI definition should be able to deal with these, i.e. still provide accurate estimation of the vascular reactivity markers. This might limit the potential of atlas-based ROI definitions, especially when taking into account that activated regions may be shifted outside of the area defined by an atlas that is constructed based on data of healthy subjects. However, functional definitions might be affected by circular analysis, or ‘double-dipping’ especially when the ROI is defined at the individual level: first the level of activation is determined, and subsequently the amplitude (or timing) of the maximally (or significantly) affected voxels is determined, i.e. selection of voxels is directly or indirectly based upon the outcome marker one is interested in.

In this work three methods for ROI-definition and the influence of this definition on outcome markers are investigated. Evaluation is done by four experiments with the first three done on a reproducibility dataset in healthy volunteers and the last done in pre-symptomatic and symptomatic D-CAA patients. In the first experiment, the ROIs resulting from each of the methods were compared in volume and overlap (described in 2.4.1). In the second experiment, the outcome measures generated by each of the ROIs were compared (described in 2.4.2). In the third experiment, the effect on reproducibility of ROI generation and outcome measures are compared (described in 2.4.3). And in the fourth experiment, the impact of the presence of lesions within the visual cortex was investigated for the different approaches (described in 2.4.4).

2. METHODS

To fully explore all of the aforementioned aspects two distinct datasets were analyzed: one dataset with DNA proven D-CAA mutation carriers and age- and sex matched control subjects in which the influence of pathology will be studied, and one with strictly healthy participants who were scanned twice, with ~3 weeks

between sessions, to allow assessment of reproducibility [18]. The D-CAA patient-control dataset was acquired with the same scan parameters and on the same MR scanner as used for the healthy subjects. This D-CAA dataset has been previously described and was acquired as part of the study ‘Early Detection of Angiopathy Network (EDAN)’ [17]. Patient characteristics are summarized in *Table 1*. Informed consent was obtained from all participants of both cohorts. In line with IRB regulations, formal IRB approval was waived for the cohort of healthy participants, and study protocols for the D-CAA patient-control dataset were approved by the local IRB.

Table 1: Participant characteristics

	HEALTHY	CLINICAL STUDY (EDAN)		
		PRESYMPTOMATIC	SYMPTOMATIC	CONTROLS
Age (years)	42±12	34±12	55±5	46±14
Sex				
Men	10(83%)	3(25%)	7(47%)	13(39%)
Women	2(17%)	9(75%)	8(53%)	20(61%)

2.1 MRI acquisition

All participants were scanned on a whole-body Philips Achieva 3T MRI system (Best, the Netherlands) using a 32 channel head coil. Structural 3D T1-weighted (T1-W) images (echo time (TE) 4.6ms, repetition time (TR) 9ms, Flip 8°, field of view (FOV) = 224 × 177 × 168 mm, scan duration ~5mins); a 3D T2*-weighted image with a TE/TR of 31ms/45ms, FOV 250 × 175 × 112mm, matrix 320 × 317, 114 slices, scan duration 155 sec; and BOLD fMRI scans were acquired with a TE/TR of 31ms/1499ms, FOV 220 × 220 × 75 mm, matrix 80 × 80, 25 slices, 130 dynamics,

scan duration 201sec repeated three times. The visual stimulus consisted of 12 blocks of an 8Hz flashing radial black and white checkerboard pattern for 20 seconds alternated with 28 seconds of a fixed grey screen as rest condition [14, 17].

2.2 Preprocessing

2.2.1 Anatomical scans

Anatomical scans were processed using tools available in FSL v 6.0 (FMRIB's Software Library, www.fmrib.ox.ac.uk/fsl). First, non-brain tissue was removed using BET. The T1-W scans were segmented using FMRIB's Automated Segmentation Tool (FAST) [25] and the white matter borders were used for a boundary based linear co-registration with the fMRI scans [26] as contained in FLIRT[27, 28]. Then the structural scans were registered to the standard MNI152 template contained in FSL (MNI152NLIN6Asym) using first linear (FLIRT[27, 28]) and subsequently nonlinear registration (FNIRT[29]). The inverse of these matrices were later applied to transform atlases to the participant's T1-W and subsequently to their fMRI scans.

2.2.2 Functional scans

fMRI data processing was carried out using FEAT (fMRI Expert Analysis Tool) Version 6.00, part of FSL. The following pre-statistics processing were applied: motion correction using MCFLIRT [27]; slice-timing correction using Fourier-space time-series phase-shifting; non-brain removal using the Brain Extraction Tool (BET) [30]; spatial smoothing using a Gaussian kernel of FWHM 3.0mm; grand-mean intensity normalization of the entire 4D dataset by a single multiplicative factor; high-pass temporal filtering (Gaussian-weighted least-squares straight line fitting, with $\sigma=24.0s$). To investigate the possible presence of unexpected artefacts or activation, ICA-based exploratory data analysis was carried out using MELODIC

[31]. The statistical analysis of the time-series was carried out using FILM with local autocorrelation correction [32]. The obtained z-statistic map was used for further analysis.

2.2 ROI determination

To investigate the impact of ROI determination on outcome measures, three previously proposed approaches were compared:

2.2.1 “Structural” ROI

One way of defining the ROI over which the hemodynamic response is averaged, is to transform the standardized atlas of the visual cortex to the subject’s fMRI space. A previous study applied this method of deriving an ROI as a secondary analysis [13]. From the Juelich atlas [33] the V1 visual cortex was selected and transformed from MNI to structural space and subsequently to functional space using the linear and non-linear transformations from the earlier described registration [26-29]. This method is referred to as the “structural” method.

2.2.2 Group-based “functional” ROI

In other studies, a group-based functional ROI was determined based on group-based activation in a subset of the participants [14, 17]. In short, z-statistic maps of the included participants were transformed to a standard cortical ribbon (fsaverage from FreeSurfer) [34]. Mean activation was determined using a one-sample group mean GLM and a contiguous region of activation was created by applying an uncorrected significance threshold of $P < 0.001$. This ROI was then transformed back to the individual fMRI spaces. The procedure is described in detail in Dumas *et al.* [14]. In our study we generated for each dataset a separate functional ROI: for the first datasets (healthy subjects) two separate functional ROIs were created for the first and second visit; for the second (EDAN) dataset, a single functional ROI was created based on the first eight D-CAA mutation carriers

and their eight age- and sex matched control subjects, resulting in a template based on 16 participants. This method will be referred to as the “functional” method.

2.2.3 Activation ROI: “percentile” of z-statistics map

The third proposed method selects an individual ROI based on the participant’s z-statistic map [13, 18, 19, 35]. For each individual, the top percentile or predetermined volume of voxels with the highest z-score is selected as ROI. In this study, we included a region with a volume of 11.5cm^3 , containing the 503 most active voxels [13]. This method is referred to as the “percentile” method.

2.3 Hemodynamic response function models

A further consideration is the hemodynamic response function (HRF), or basis function, to be convoluted with the stimulus profile in the analysis [23]. Using different HRF models as basis function may yield different results in the functional- and activation-based approaches. Therefore, both a gamma and an “optimal” HRF generated by FSL’s FMRIB Linear Optimal Basis Sets (FLOBS) are investigated in this study [36]. Results of these analyses are presented in the supplementary materials. When not mentioned explicitly, data was analyzed with the gamma HRF.

2.4 Comparing ROI methods

The three approaches to define the ROI were compared both at the ROI-level (i.e. overlap and total volume of the ROI) as well as at the outcome level (amplitude and timing parameters of the BOLD response). First, ROIs were generated using the aforementioned methods for all subjects. The average time course of the BOLD response to the visual stimulus for each study participant was calculated by averaging the time-courses of all voxels within the ROI and converting to BOLD percent signal change using the time-course average as baseline value, then averaging across all stimulus blocks. The block responses were subsequently fitted

to a trapezoidal function defined by three parameters: the time to reach peak (TTP) response, the response amplitude (AMP), and the time to return to baseline (TTB) using a previously described fitting algorithm [14, 17].

2.4.1 Comparison at the ROI-level

To assess to what extent the three approaches result in a similar ROI, the DICE coefficient (see Eq. 1: area of the overlapping voxels divided by the sum of the areas of both ROIs) was assessed between all ROIs [37]:

$$DICE = \frac{2 * (|ROI_{method\ 1}| \cap |ROI_{method\ 2}|)}{|ROI_{method\ 1}| + |ROI_{method\ 2}|} \quad [Eq. 1]$$

2.4.2 Comparison at the outcome level

Subsequently, the approaches were compared by testing the impact of the ROI-selection on the ROI-averaged primary outcome measures (TTP, TTB, AMP) using correlation- and Bland-Altman plots. Group differences were assessed using a regression model, adjusting for age and sex, between pre-symptomatic mutation carriers and controls; as well as between symptomatic mutation carriers and controls.

2.4.3 Comparison of reproducibility

The datasets of healthy participants were tested for reproducibility of both the ROIs and outcome measures. Intra-subject inter-session ROIs were tested for each method using DICE coefficient, and outcome measures were tested for reproducibility by calculating Pearson correlation between sessions [38].

2.4.4 Assessment of the influence of lesions

As already mentioned, a complicating matter of measuring the vascular response in neurovascular patients, is the presence of pathological tissue and imaging artifacts due to cerebral hemorrhages. Important to note is that these are much more prevalent in D-CAA than in sporadic CAA patients and different studies deal in different manners with them. Some opt, for example, to disregard the complete hemisphere when an ICH is present, others exclude ICHs based on manual delineation of lesions. To test the influence of the presence of lesions a similar approach as described in Dumas et al. [8] (described in detail in their supplemental material) was used: the BOLD scans were coregistered with T2* weighted images and hemorrhagic lesions were manually masked out on the BOLD scan by an experienced rater (E.K., 5 years of experience); furthermore, these masks were isotropically dilated by 7mm to provide more rigorous masks. All voxels within these masks were then subsequently excluded from the secondary analysis. Relative remaining volumes were determined both when excluding only voxels with presence of hemosiderin as well as with the dilated lesion mask. Outcome measures were assessed again for all participants.

3. RESULTS

3.1 Comparison at the ROI-level

Visual inspection showed that the different methods resulted in different ROI selections with the biggest difference in the number of voxels included, whereas for all methods most of the selected voxels were located in the occipital lobe as expected for a visual paradigm (*Figure 1*). However, in symptomatic patients many spurious voxels were observed, spread throughout the whole brain, when ROI selection was based upon the percentile method (example shown in *Figure 1L*). An example of the effect of using a different HRF is shown in *Supplementary figure 1*. When quantified using the Dice coefficient, it becomes clear that the three methods resulted in quite different selections (*Table 2*). The highest Dice coefficient (with a maximum value of 0.255 in the healthy cohort) was found

between the ROIs based on the group-based functional activations and the ROIs with the highest 11.5cm³ responding voxels of the z-statistic map. The overlap between the ROIs of the different methods was smaller in the dataset of the clinical study compared to the dataset of healthy subjects.

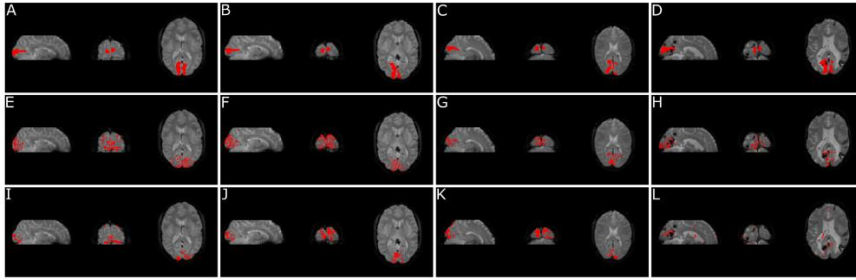


Figure 1: ROIs as determined by the different methods: the first row (A-D) shows the structural method based on the registration of an atlas-based V1 ROI to the subject-space; the second row (E-H) depicts the functional ROI based upon an group-averaged activation map, and the final row (I-L) shows the percentile method that selects for each subject the strongest responding voxels up to an ROI volume of 11.5 cm³. The first column (A,E,I) shows the first visit of a healthy subject, the second column (B,F,J) the second visit of the same healthy subject, the third column (C,G,K) shows a control subject of the EDAN study and the final column (D,H,L) shows a symptomatic D-CAA mutation carrier. Clear differences can be observed between the ROIs selected by the different methods. Furthermore, it can be seen that within the symptomatic mutation carrier some methods include voxels in the ROI that are located within the ICH, and that with the z-statistic based approach a more random pattern is obtained for the ROI, including many voxels not located within the occipital lobe. An example of the effect of using a different HRF is shown in Supplementary figure 1.

Table 2: DICE coefficient showing the overlap between ROIs obtained by different methods. All methods have a low level of overlapping voxels with one another.

	HEALTHY			CLINICAL STUDY (EDAN)		
	STRUCTURAL	FUNCTIONAL	PERCENTILE	STRUCTURAL	FUNCTIONAL	PERCENTILE
STRUCTURAL	-	0.177±0.031	0.184±0.040	-	0.190±0.061	0.156±0.066
FUNCTIONAL	0.177±0.031	-	0.255±0.035	0.190±0.061	-	0.196±0.070
PERCENTILE	0.184±0.040	0.255±0.035	-	0.156±0.066	0.196±0.070	-

3.2 Comparison at the outcome level

Our analysis of the data from the clinical EDAN study are provided in *Figure 2* showing that the ROI-selection method would have impacted the conclusion from a between group comparison. Especially, when using the percentile method no difference between the younger and older control participants was observed, whereas for the other two methods the older control subjects showed a smaller amplitude. Moreover, a more clear response was observed for the percentile method in the symptomatic patients than for the other two methods (*Figure 2*). Mean group BOLD responses when using a different HRF are shown in *Supplementary Figure 2*.

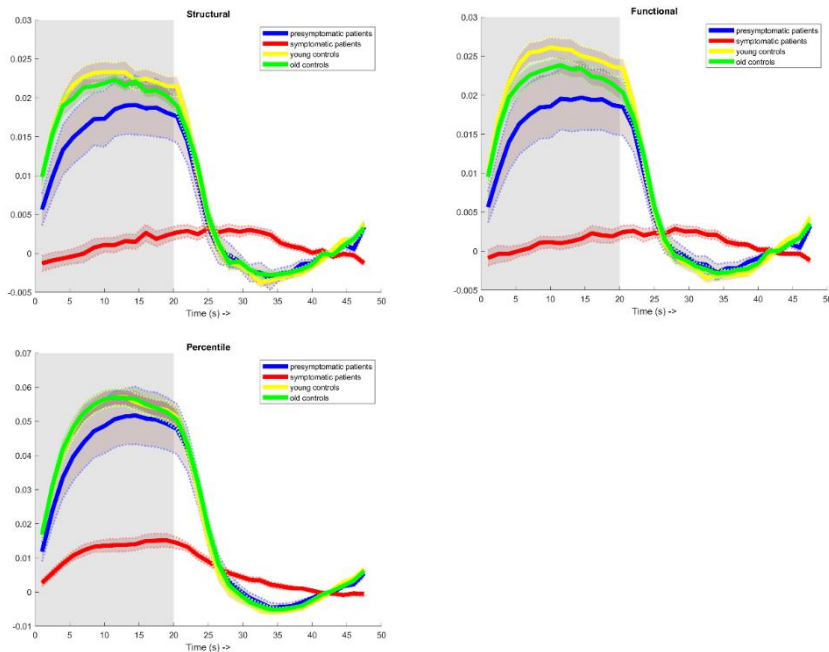


Figure 2: Group averages (solid lines) and standard error of the mean (dashed lines) when applying the different methods for the ROI definition over which the BOLD-response upon visual stimulation is determined. In order (left to right, top to bottom): the different methods for ROI definition, respectively structural, functional and percentile. The blue curves show the average response in pre-symptomatic D-CAA patients (N=12), the yellow curves show the averaged response in control subjects age-matched with the pre-

symptomatic D-CAA carriers, the red curves show the response of symptomatic patients and the green curve the control subjects of the symptomatic subjects. The structural and functional methods yield similar results, whereas the percentile method fails to pick up differences between young and old control subjects. Moreover, the amplitude of all curves of the percentile method is higher compared to the other two ROI-selection approaches and a more pronounced response is found in symptomatic D-CAA patients.

Figure 3 shows two Bland-Altman plots illustrating two typical findings as also observed in many of the other Bland-Altman plots (all Bland-Altman plots can be found as *Supplementary Figure 3*). Firstly, a large variation in differences in timing parameters was observed for higher values of the timing parameters, especially between the structural and functional method (right part of the Bland-Altman plot). Secondly, a proportional error with significant bias was found when the amplitude outcome measure of the percentile ROI-method was compared to either the functional or structural method. Furthermore, group averages for outcome measures are shown in *Table 3*, differences between mutation carriers and control subjects were assessed with a regression model, adjusting for age and sex. While trends seem relatively stable between the structural and functional methods, especially TTP seems to yield different results when using the percentile method: the presymptomatic group is no longer significantly different from control participants, and symptomatic patients have a TTP much closer to control subjects as well.

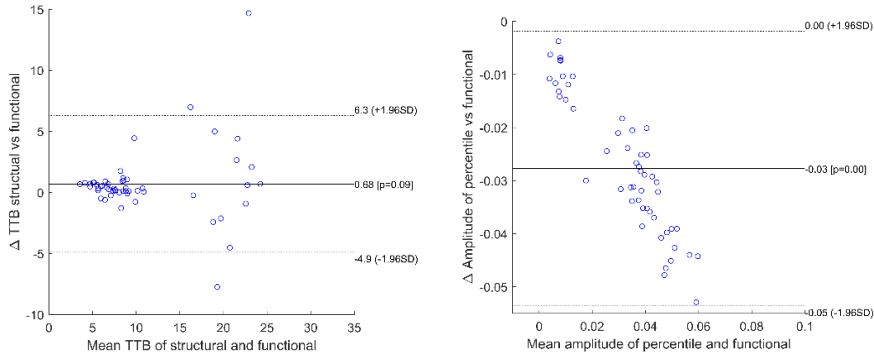


Figure 3: Two example Bland-Altman plots comparing different ROI selection approaches and the influence of this on the different outcome parameters. All other Bland-Altman plots are shown in Supplementary figure 3. The left plot shows how comparable the time-to-baseline (TTB) is when using the structural or functional method. The right plot compares the influence of ROI selection (percentile versus functional method) on the amplitude of the visual reactivity. All Bland-Altman plots have been calculated on the data of the clinical study on D-CAA. Two main observations can be made. First, the variation between the TTB obtained with the structural and functional method, is highly depended on the magnitude of the TTB, showing increased discordance between the methods for higher TTB-values (left plot). Secondly, for the amplitude parameter a proportional error in combination with significant bias can be observed (right plot) when comparing the percentile with functional method.

Table 3: Mean time to peak, time to baseline and amplitude outcome measures for each method, for pre-symptomatic mutation carriers, symptomatic mutation carriers and control subjects. In brackets the beta coefficient is reported. All values reported with standard deviation, significantly different from control subjects at * $P<0.05$, ** $P<0.01$, *** $P<0.001$, ^x indicates a significant result when correcting for multiple comparison using Bonferroni.

		STRUCTURAL	FUNCTIONAL	PERCENTILE
Time to peak	Controls	4.95±1.94	4.70±1.62	6.29±2.07
	Pre-symptomatic	9.83±8.39(0.505)** ^x	8.68±7.54(0.461)** ^x	7.16±1.59(0.194)
	Symptomatic	17.57±10.48(0.743)*** ^x	26.64±14.54(0.821)*** ^x	7.70±2.81(0.337)*
Time to baseline	Controls	7.23±1.78	7.02±2.10	8.27±1.69
	Pre-symptomatic	10.69±7.51(0.462)** ^x	10.25±6.39(0.393)*	9.60±3.60(0.362)** ^x
	Symptomatic	18.47±4.30(0.907)*** ^x	20.94±4.84(0.900)*** ^x	16.85±4.53(0.798)*** ^x
Amplitude	Controls	2.37±0.612	2.50±0.53	5.84±1.21
	Pre-symptomatic	1.87±1.07(-0.521)*** ^x	1.22±0.49(-0.559)*** ^x	4.94±2.60(-0.465)** ^x
	Symptomatic	0.42±0.23(-0.757)*** ^x	0.33±0.25(-0.810)*** ^x	0.63±0.18(-0.799)*** ^x

3.3 Comparison of reproducibility

When comparing the outcome measures on vascular reactivity between two repeated measurements (~3 weeks apart), a good reproducibility was found for all three ROI-selection approaches, see *Table 4* which shows the Pearson's correlation coefficients and P-values. When comparing the three outcome measures, the time-to-baseline was less reproducible than the other two outcome measures. When comparing the three ROI-selection methods, the functional ROI approach performed a bit poorer than the other two methods (*Table 4*).

Table 4: Pearson correlation between the two visits of the healthy participants for each method and each outcome measure. Pearson's coefficients and P-values are displayed with

	<u>Time to peak</u>		<u>Time to baseline</u>		<u>Amplitude</u>	
	Pearson's	P-value	Pearson's	P-value	Pearson's	P-value
STRUCTURAL	0.737	0.006	0.623	0.030	0.801	0.002
FUNCTIONAL	0.726	0.007	0.486	0.109	0.796	0.002
PERCENTILE	0.648	0.023	0.680	0.015	0.855	0.000

the highest Pearson's coefficient depicted in bold.

3.4 Assessment of the influence of lesions

Figure 4 shows an example of a patient with a hemorrhage in the visual cortex. All three ROI selection algorithms resulted in inclusion of voxels located within the hemorrhagic lesion, which was outlined on a co-registered SWI sequence. While the functional and structural methods showed a similar number of voxels within the ICH (15.7% and 17.1%, respectively), the ROI obtained by the percentile method contained less voxels within or near the lesions. The fraction of voxels remaining after exclusion of hemorrhagic lesions and when using a dilated lesion mask are shown in *Supplementary Figure 4*.

At group level, the exclusion of hemorrhagic voxels, both with and without dilation of the ROIs, seems to only have a minor impact on outcome measures.

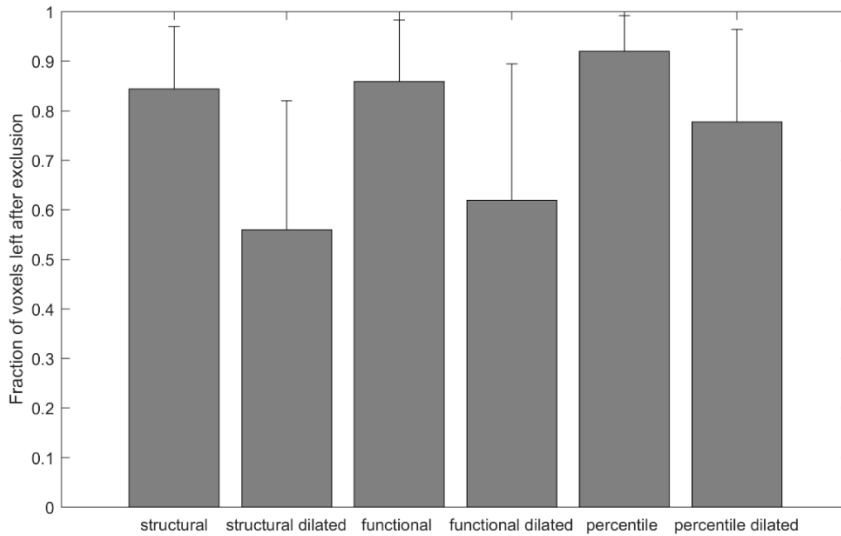


Figure 4.: The bar graphs indicate the mean fraction of voxels remaining after excluding voxels within the ICH or after dilating the ICH-segmentation with a 7mm isotropic kernel. Error bars indicate standard deviation. For this graph only subjects who had one or more voxels were included.

4. DISCUSSION

The findings of this study confirm that different ROI-selection approaches for calculating visual task based vascular reactivity significantly affect the outcome: we showed that it results in different voxels included for analysis, that the inclusion of these voxels lead to different outcome measures, that it can affect trends as observed in group analyses, and that the impact of pathology on these outcome measures differs between the approaches.

When applying three previously proposed postprocessing methods, different ROIs are selected with only very moderate Dice overlap scores between them. This would not per definition lead to differences in outcome measures: e.g. if these subsets of voxels are in fact part of a larger region with a similar response to the

stimulus, one would still obtain similar outcome measures. However, this work showed that the different ROIs do not only have little overlap, but they also lead to differences in outcome measures (see *Table 3*). Furthermore, whereas all three methods also selected voxels within hemorrhagic lesions as identified on SWI, the impact of this as measured by the percentage of selected voxels within or just outside the ICH-mask was much lower for one approach, the percentile method, compared to the other two methods. However, exclusion of ICH-voxels from the ROIs only had a small effect on the outcome measures.

These findings point to a dependency on the ROI-selection approach, but it is more difficult to decide on the best approach. Visual inspection of the ROIs selected in symptomatic D-CAA patients by the percentile method, points to the intrinsic vulnerability of the approach towards circular analysis, or “double-dipping”. In these symptomatic D-CAA patients the vascular response to a visual stimulus as measured by BOLD is very low, or on average even close to be absent [17]. Due to this almost absence of a BOLD-response in the visual cortex, selection of voxels with highest z-score resulted in the inclusion of many voxels outside of the occipital cortex, which probably by chance showed some correlation with the stimulus. While these voxels are very low in their z-score, the probability that the signal fluctuation found in these voxels is representative of a true vascular response to the visual stimulus is rather small. This can also be deduced from the fact that some of these voxels are even found in regions where no vessel or brain tissue is present (e.g. inside the lateral ventricles, *Figure 1L*). Therefore, it can be assumed that mainly voxels are included with a similar pattern in the noise/artifact profile rather than voxels with a true vascular response. When averaging these voxels, a trend towards a response can be deduced from the data, just because we selected noise voxels correlating mildly with the stimulus paradigm: a clear example of a ‘double dipping’ error and inclusion bias. The fact that this method seems to also change average group measures leads to a word of caution when applying this method in patients with severely disturbed vascular reactivity

(supplementary data). Even though this approach is very robust against the presence of lesions (i.e. it selected the lowest percentage of voxels from within the ICH regions, e.g. *Supplementary figure 4*), we would only advise the use of this approach in populations with normal or only relative mildly impaired vascular responses and thus not in symptomatic D-CAA patients. Furthermore, one could argue that an improved selection algorithm could easily be proposed by adding a constraint that only voxels in predetermined (posterior) parts of the brain are included. One could expect such a hybrid method would yield also hybrid results, i.e. a less pronounced hemodynamic response in mutation carriers than without such constraints, but more pronounced than the other methods. For this study, we decided to only include selection criteria that have been applied before, but hope that the results will stimulate proposal of new methods.

While for the structural and functional ROI determination the shape of the HRF has no to little impact, respectively, on the final results, there may be different voxels included when a different HRF is applied to the percentile approach. For example, we did notice a more visual cortex based distribution in some (but not all) symptomatic D-CAA patients when using a different HRF (*Supplementary Figure 1*). On a group level this did not lead to different results. However, further research should be conducted on how and why the HRF of these patients is changed [23].

Another word of caution is related to the influence of the ROI-selection procedure on the more extreme values of outcome measures. From the increased variance in the Bland-Altman plots for delayed timings (see e.g. right panel of *Figure 3*), it is clear that the selection process especially influences these measurements. Due to the very low response measured in the most affected patients, it becomes on one hand more arbitrary which voxels to include and on the other hand the inclusion of voxels with some response will have a more prominent influence on the mean shape of the response. In such cases, the fitted trapezoid may no longer be a good reflection of the real response and whereas the amplitude might still reflect a

correct measure (i.e. a small response), the timing parameters of the trapezoid may no longer be reflecting the true onset and recovery timings of the vascular response. Further research is needed how to deal with such data. For example, abstaining from calculation of timing parameters for subjects in whom the amplitude of the response is below a certain threshold is one possible solution, whereas using a ceiling value on the timing parameters could be another approach.

Finally, it should be considered how to deal with pathology in patient studies. This is especially relevant in CAA-patients, since ICH in the occipital lobe is a hallmark of the disease. In a previous study in sporadic CAA patients, a sub-analysis was applied to exclude ICHs from the ROIs: a mask containing hemorrhagic lesions was made by an experienced observer based on a co-registered T2* weighted sequence. [14] This mask was subsequently dilated and those voxels were excluded from the secondary analysis. The exclusion of ICH-affected voxels was found to be of little influence on the outcome markers. Another solution is the exclusion of the complete hemisphere from analysis when an ICH is present. As ICH is even more prevalent in D-CAA compared to sporadic CAA, we did not exclude hemispheres in this study, nor in previous publications with this dataset. [17] In our study we found differences in included voxels, at times ranging up to a reduction of up to 80% when using a dilated lesion mask. The amount of voxels excluded by this method was smallest in the percentile method, as the chance that voxels in a hypointense region to correlate with the visual stimulus paradigm is small. However, the impact on outcome measures was not significant. Furthermore, it should be mentioned that the processing time for the functional ROI approach was found to be much longer than the other two methods, especially in the presence of cortical ICH, as each subject had to be processed by FreeSurfer.

There are some limitations to this study that need to be considered. First, we did not correct for confounding factors on the BOLD response such as heart rate and breathing that may influence the BOLD signal.[39, 40] Furthermore, there were no instructions for participants regarding diet, caffeine use, or other habits that may impact their vascular response. Lastly, this study only looked at the effect of post-processing. Different acquisition parameters, MRI hardware, paradigms and trapezoidal fitting may also lead to different results. Strengths of our study are that the differences between currently applied models in this field of research were not only tested in healthy subjects, but also in patients with different levels of vascular impairment. With the increasingly recognized importance of vascular reactivity measures in CAA research, our studies aids in making informed choices on what approach to apply in future studies. Another limitation is that the group-based functional method is based on a subset of the participants, similar as done previously [14, 17]. This might have introduced a bias in the analysis. We did investigate whether using the second visit of the healthy participants or a different set of mutation carriers/healthy subjects would have led to significantly different ROIs. We observed Dice coefficient of 0.75 for both experiments (Data not shown), showing a large overlap and thus little influence on the ROI-selection.

Our findings are limited to D-CAA patients, who have a much broader range of pathology than sporadic CAA patients, including the complete spectrum of pre-symptomatic patients up to patients with very severe pathology. Sporadic CAA patients get most often only diagnosed after entering the symptomatic phase, while frequently exhibiting a less severe form of pathology. On the other hand, sporadic CAA patients are on average older than the participants in our cohort, which may lead to additional confounding factors. However, in histopathology as well as radiologically the two are considered similar [41, 42]. Furthermore, when we compare vascular reactivity findings from D-CAA cohorts [17] with findings of sporadic CAA patients [13, 14], very similar changes can be observed. Therefore,

we feel confident that the findings of this study on optimal post-processing strategies can directly be translated to sporadic CAA.

Finally, it is important to recognize that these findings are not only relevant to study neurovascular functioning in CAA, but also for other brain diseases, such as Alzheimer's Disease, Huntington Disease, and CADASIL [35, 43, 44]. With this broader application of such measures, it is increasingly important to create a more homogeneous approach for defining the region of interest when performing these measurements.

In conclusion, to avoid the issue of circular analysis ("double-dipping") a transformed structural method or a functional method is recommended for neurovascular reactivity measurements. Both these methods appear to give similar results with the structural method being more reproducible, whereas the functional method is more robust in the presence of hemorrhagic lesions in the occipital lobe. The poorer reproducibility of the functional method might be explained by inter-study changes of the mean activation mask, whereas a functional atlas exploits the same mask for all studies.

Funding

This research has been made possible by the Dutch Heart Foundation and the Netherlands Organisation for Scientific Research (NWO), as part of their joint strategic research programme: "Earlier recognition of cardiovascular diseases". This project is partially financed by the PPP Allowance made available by Top Sector Life Sciences & Health to the Dutch Heart foundation to stimulate public-private partnerships.

5. REFERENCES

1. Smoliński, Ł., et al., *Cerebrovascular reactivity and disease activity in relapsing-remitting multiple sclerosis*. Advances in clinical and experimental medicine : official organ Wrocław Medical University, 2020. **29**(2): p. 183-188.
2. Yeh, M.Y., et al., *Cerebrovascular Reactivity Mapping Using Resting-State Functional MRI in Patients With Gliomas*. J Magn Reson Imaging, 2022. **56**(6): p. 1863-1871.
3. Thrippleton, M.J., et al., *Cerebrovascular reactivity measurement in cerebral small vessel disease: Rationale and reproducibility of a protocol for MRI acquisition and image processing*. Int J Stroke, 2018. **13**(2): p. 195-206.
4. Viswanathan, A. and S.M. Greenberg, *Cerebral amyloid angiopathy in the elderly*. Ann Neurol, 2011. **70**(6): p. 871-80.
5. Boulouis, G., A. Charidimou, and S.M. Greenberg, *Sporadic Cerebral Amyloid Angiopathy: Pathophysiology, Neuroimaging Features, and Clinical Implications*. Semin Neurol, 2016. **36**(3): p. 233-43.
6. Charidimou, A., et al., *Emerging concepts in sporadic cerebral amyloid angiopathy*. Brain, 2017. **140**(7): p. 1829-1850.
7. Knudsen, K.A., et al., *Clinical diagnosis of cerebral amyloid angiopathy: validation of the Boston criteria*. Neurology, 2001. **56**(4): p. 537-9.
8. van Rooden, S., et al., *Descriptive analysis of the Boston criteria applied to a Dutch-type cerebral amyloid angiopathy population*. Stroke, 2009. **40**(9): p. 3022-7.
9. Fotiadis, P., et al., *Cortical atrophy in patients with cerebral amyloid angiopathy: a case-control study*. Lancet Neurol, 2016. **15**(8): p. 811-819.
10. Subotic, A., et al., *Cortical Thickness and Its Association with Clinical Cognitive and Neuroimaging Markers in Cerebral Amyloid Angiopathy*. Journal of Alzheimer's disease : JAD, 2021. **81**(4): p. 1663-1671.
11. Wermer, M.J.H. and S.M. Greenberg, *The growing clinical spectrum of cerebral amyloid angiopathy*. Current Opinion in Neurology, 2018. **31**(1): p. 28-35.
12. Reijmer, Y.D., et al., *Relationship between white matter connectivity loss and cortical thinning in cerebral amyloid angiopathy*. Human brain mapping, 2017. **38**(7): p. 3723-3731.
13. Switzer, A.R., et al., *Longitudinal decrease in blood oxygenation level dependent response in cerebral amyloid angiopathy*. NeuroImage. Clinical, 2016. **11**: p. 461-467.
14. Dumas, A., et al., *Functional MRI Detection of Vascular Reactivity in Cerebral Amyloid Angiopathy*. Annals of neurology, 2012. **72**(1): p. 76-81.
15. Smith, E.E., et al., *Impaired visual evoked flow velocity response in cerebral amyloid angiopathy*. Neurology, 2008. **71**(18): p. 1424-30.
16. Nortley, R., et al., *Amyloid β oligomers constrict human capillaries in Alzheimer's disease via signaling to pericytes*. 2019. **365**(6450): p. eaav9518.
17. van Opstal, A.M., et al., *Cerebrovascular function in pre-symptomatic and symptomatic individuals with hereditary cerebral amyloid angiopathy: a case-control study*. The Lancet. Neurology, 2017. **16**(2): p. 115-122.
18. van Dijk, S.E., et al., *Aging Effect, Reproducibility, and Test-Retest Reliability of a New Cerebral Amyloid Angiopathy MRI Severity Marker-Cerebrovascular Reactivity to Visual Stimulation*. J Magn Reson Imaging, 2022.
19. van Dijk, S.E., et al., *Longitudinal Progression of Magnetic Resonance Imaging Markers and Cognition in Dutch-Type Hereditary Cerebral Amyloid Angiopathy*. Stroke, 2022. **53**(6): p. 2006-2015.
20. Sleight, E., et al., *Cerebrovascular Reactivity Measurement Using Magnetic Resonance Imaging: A Systematic Review*. Front Physiol, 2021. **12**: p. 643468.
21. Beaudin, A.E., et al., *Cerebrovascular Reactivity Across the Entire Brain in Cerebral Amyloid Angiopathy*. Neurology, 2022. **98**(17): p. e1716-e1728.
22. Peca, S., et al., *Neurovascular decoupling is associated with severity of cerebral amyloid angiopathy*. Neurology, 2013. **81**(19): p. 1659-65.

23. Williams, R.J., et al., *Identification of neurovascular changes associated with cerebral amyloid angiopathy from subject-specific hemodynamic response functions*. J Cereb Blood Flow Metab, 2017. **37**(10): p. 3433-3445.
24. Greenberg, S.M., et al., *Outcome markers for clinical trials in cerebral amyloid angiopathy*. Lancet Neurol, 2014. **13**(4): p. 419-28.
25. Zhang, Y., M. Brady, and S. Smith, *Segmentation of brain MR images through a hidden Markov random field model and the expectation-maximization algorithm*. IEEE Trans Med Imaging, 2001. **20**(1): p. 45-57.
26. Greve, D.N. and B. Fischl, *Accurate and robust brain image alignment using boundary-based registration*. Neuroimage, 2009. **48**(1): p. 63-72.
27. Jenkinson, M., et al., *Improved optimization for the robust and accurate linear registration and motion correction of brain images*. Neuroimage, 2002. **17**(2): p. 825-41.
28. Jenkinson, M. and S. Smith, *A global optimisation method for robust affine registration of brain images*. Med Image Anal, 2001. **5**(2): p. 143-56.
29. Andersson JLR, J.M., Smith S *Non-linear registration, aka spatial normalisation*. . FMRIB technical report TR07JA2, 2010.
30. Smith, S.M., *Fast robust automated brain extraction*. Hum Brain Mapp, 2002. **17**(3): p. 143-55.
31. Beckmann, C.F. and S.M. Smith, *Probabilistic independent component analysis for functional magnetic resonance imaging*. IEEE Trans Med Imaging, 2004. **23**(2): p. 137-52.
32. Woolrich, M.W., et al., *Temporal autocorrelation in univariate linear modeling of fMRI data*. Neuroimage, 2001. **14**(6): p. 1370-86.
33. Amunts, K., et al., *Brodman's areas 17 and 18 brought into stereotaxic space-where and how variable?* Neuroimage, 2000. **11**(1): p. 66-84.
34. Fischl, B., *FreeSurfer*. Neuroimage, 2012. **62**(2): p. 774-81.
35. Coppen, E.M., et al., *Structural and functional changes of the visual cortex in early Huntington's disease*. Hum Brain Mapp, 2018. **39**(12): p. 4776-4786.
36. Woolrich, M.W., T.E. Behrens, and S.M. Smith, *Constrained linear basis sets for HRF modelling using Variational Bayes*. Neuroimage, 2004. **21**(4): p. 1748-61.
37. Bonar, D.C., et al., *Graphical analysis of MR feature space for measurement of CSF, gray-matter, and white-matter volumes*. J Comput Assist Tomogr, 1993. **17**(3): p. 461-70.
38. Koo, T.K. and M.Y. Li, *A Guideline of Selecting and Reporting Intraclass Correlation Coefficients for Reliability Research*. Journal of chiropractic medicine, 2016. **15**(2): p. 155-163.
39. Birn, R.M., et al., *The respiration response function: the temporal dynamics of fMRI signal fluctuations related to changes in respiration*. NeuroImage, 2008. **40**(2): p. 644-654.
40. Chang, C., J.P. Cunningham, and G.H. Glover, *Influence of heart rate on the BOLD signal: the cardiac response function*. NeuroImage, 2009. **44**(3): p. 857-869.
41. Bornebroek, M., et al., *Hereditary cerebral hemorrhage with amyloidosis-Dutch type (HCHWA-D): I--A review of clinical, radiologic and genetic aspects*. Brain Pathol, 1996. **6**(2): p. 111-4.
42. Maat-Schieman, M.L., et al., *Hereditary cerebral hemorrhage with amyloidosis-Dutch type (HCHWA-D): II--A review of histopathological aspects*. Brain Pathol, 1996. **6**(2): p. 115-20.
43. Switzer, A.R., et al., *Cerebrovascular reactivity in cerebral amyloid angiopathy, Alzheimer disease, and mild cognitive impairment*. Neurology, 2020. **95**(10): p. e1333-e1340.
44. Huneau, C., et al., *Altered dynamics of neurovascular coupling in CADASIL*. Ann Clin Transl Neurol, 2018. **5**(7): p. 788-802.

Chapter 4

High temporal resolution fMRI for visual-activation induced vascular reactivity measurements in D-CAA mutation carriers

T.W. van Harten, M.R. Schipper, S. Voigt, E.A. Koemans, I. Rasing, H.J.A. van Os, M.A.A. van Walderveen, M.J.H. Wermer, M.J.P. van Osch

ABSTRACT

Both in sporadic as well as in Dutch type hereditary Cerebral Amyloid Angiopathy (CAA) cerebral vascular reactivity upon a visual stimulus is decreased and delayed. Currently, most fMRI experiments employ a BOLD scan with a visual stimulus of around 20s and a temporal resolution of 1.5-2s. However, CAA-induced changes in the timing parameters happen on a much smaller timescale than the event-duration of the visual stimulus, whereas the sampling rates of employed sequences are of the same order of magnitude. To further elucidate the CAA associated changes in vascular reactivity, shorter visual stimulus periods and a higher sampling rate may be warranted. By monitoring the BOLD response to a short visual stimulus (3s) with high temporal resolution scanning (0.1s TR), we show that robust hemodynamic responses can be obtained with even responses in subjects who do not exhibit clear responses on more conventional protocols. The new data support conclusions from earlier studies that the main, positive BOLD response in D-CAA mutation carriers is both decreased as well as delayed, whereas this study adds to the literature the observation that the post-stimulus undershoot is less affected.

1. Introduction

Cerebral Amyloid Angiopathy (CAA) is a major cause of intracerebral hemorrhages (ICH) and cognitive decline in elderly [1]. In CAA the protein amyloid-beta accumulates in the vessel wall of leptomeningeal arteries [2]. The current diagnosis of CAA focusses primarily on hemorrhagic imaging hallmarks combined with clinical symptoms [3-7]. Furthermore, a multitude of ischemic processes are observed: there is a strong association with cortical thinning [8, 9], white matter hyperintensities, microinfacts [10] and changes in diffusion tensor measures [11]. Importantly, the aforementioned amyloid- β depositions are already starting to accumulate in vessel walls before the onset of symptoms of disease [12], leading to impaired cerebrovascular function [13-15]. More specifically, in Dutch-type hereditary CAA (D-CAA) patients changes in vascular reactivity have been found prior to the first ICH [16]. Furthermore, vascular reactivity decreased over time in D-CAA patients in a longitudinal study [17]. This effect has also been shown for sporadic CAA patients [13], just as the ageing effect in healthy participants has also been confirmed [18]. Therefore, vasoreactivity is a promising (early) marker to monitor CAA progression over time, for example as outcome measure in clinical trials, especially because hemodynamic changes may be present in early stages of the disease.

Because CAA tends to start in the occipital lobe [19-21], most studies employed a visual stimulus to measure vasoreactivity [13-16, 22]. The hemodynamic response to that stimulus is generally measured by blood oxygenation level dependent (BOLD) MRI. In such reactivity experiments, response characteristics, such as the amplitude, time-to-peak and time-to-baseline, are used as outcome measures. However, changes in the timing parameters happen on a much smaller timescale than the event-duration of the visual stimulus, whereas the sampling rates of employed sequences are on the same order of magnitude [23]. To further

elucidate the CAA associated changes in vascular reactivity, we propose the use of shorter visual stimulus periods in combination with a higher sampling rate.

The goal of the current study was to assess the added value of high temporal resolution BOLD MRI in combination with short visual stimuli to monitor the vascular reactivity in healthy subjects and D-CAA subjects.

2. Methods

Participants

High temporal BOLD data were obtained from female participants between the ages of 40 and 60 years, who were participating in ongoing research studies in the LUMC on D-CAA and vascular risk factors in women. The final group of participants consisted of 15 DNA confirmed D-CAA mutation carriers of which 3 were symptomatic, 5 possible D-CAA mutation carriers, and 36 healthy control participants. D-CAA mutation carrier status was established by DNA analysis confirming the codon 693 point mutation in the amyloid- β precursor protein gene. Mutation carriers were considered as symptomatic when they experienced at least one symptomatic ICH. The “possible mutation carrier” group consisted of participants who participated in the study, but elected to not be informed about their mutation status. These participants have 50% chance to be mutation carrier (i.e. one of the parents was DNA confirmed D-CAA mutation carrier), but were not tested and therefore excluded from the comparison between mutation carriers versus healthy control subjects, but the scans were still included for comparisons between scanners and sequences.

All participants provided written informed consent and all protocols were approved by the ethics committee of the LUMC.

Scans

All participants were scanned on a Philips human 7T Achieva MR-system (Philips Healthcare, Best, The Netherlands) using a quadrature transmit and 32-channel receive head coil (Nova Medical, Wilmington, MA, USA). The protocol included a 3DT1 weighted scan (scan parameters: repetition time (TR) 4.15 ms, echo time (TE) 1.86 ms, flip angle 7°, field of view (FOV) 240 x 255 x 246 mm, 250 slices, slice thickness 0.9 mm, matrix size 288 x 288, and scan duration 142 s) and a coronal single slice high temporal resolution fMRI scan through the occipital cortex (scan parameters: dynamic resolution of 100 ms, TR 100 ms, TE 22ms, flip angle 20°, FOV 100 x 141 mm, slice thickness 1.5 mm, matrix size 128 x 128, single shot EPI, SENSE factor of 2.8, 3360 dynamics, total scan duration 336 s) with a visual stimulus of seven 48s blocks consisting of 3 seconds flashing black and white radial checkerboard pattern at 8 Hz, followed by 45 seconds of grey screen.

The protocol for (possible) D-CAA mutation carriers also included a low temporal resolution scan (scan parameters: TR 1500ms, TE 22ms, flip angle 78°, FOV 190 x 220 x 45 mm, slice thickness 2.5mm, matrix size 76 x 85, single shot EPI, SENSE factor of 2.8, 224 dynamics, total scan duration 336s) with a visual stimulus of seven 48s blocks consisting of a 8-Hz flashing black and white radial checkerboard pattern for 20 seconds, followed by 28 seconds of grey screen. Moreover, these participants were also scanned on the same day on a Philips human whole body 3T Achieva MR-system (Philips Healthcare, Best, The Netherlands) using the manufacturer supplied 32-channel head coil. This protocol included a 3DT1 weighted scan (scan parameters: TR 9.75ms, TE 4.59ms, flip angle 8°, FOV 218 x 156 x 172 mm, 130 slices, slice thickness 1.2 mm, matrix size 256 x 256, total scan duration 168 s) and a low temporal resolution scan similar to the one used on the 7T system (scan parameters: TR 1500ms, TE 38ms, flip angle 78°, FOV 190 x 220 x 45 mm, slice thickness 2.5mm, matrix size 76 x 85, 224 dynamics, total scan duration 336s), also with the same visual stimulation paradigm.

Processing: visual cortex ROI definition

Anatomical scans were processed using tools available in FSL v 6.0 (FMRIB's Software Library, www.fmrib.ox.ac.uk/fsl). First, non-brain tissue was removed using BET. Then the structural scans were registered to a standard MNI152 template using linear and nonlinear registration (FLIRT [24, 25] and FNIRT [26], respectively). The inverse of these matrices were later applied to transform atlases to the participant's T1 and subsequently to their fMRI scans. To define the region of interest (ROI), an anatomically defined area centered on the primary visual cortex region was used [27]. The V1 region was derived from the Juelich Histological Atlas and overlaid on the participants' anatomical MRI scans using the aforementioned inverse matrices. The resulting ROI was subsequently resampled into the coordination space of the fMRI-scans.

Processing: BOLD-response from high temporal resolution scans

fMRI data were processed using FMRIB Software Library (FSL version 6.00, Oxford, UK). First, the BOLD MRI images were pre-processed using the following steps: motion correction with MCFLIRT [24]; non-brain removal using BET [28]; grand-mean intensity normalization of the entire 2D-time dataset by a single multiplicative factor; spatial smoothing using a Gaussian kernel of full-width-half-maximum (FWHM) of 3.0 mm; and temporally filtered using a high-pass temporal filter with $\sigma=24.0s$. Voxel-wise analysis was then performed using a general linear modelling approach FILM as implemented in the fMRI Expert Analysis Tool (FEAT) of FSL [29]. After preprocessing the mean timeseries was calculated over all voxels within the transformed V1 area.

The mean BOLD response was calculated using Matlab (Mathworks, Natick, MA, USA) by averaging across the seven stimulus blocks within the ROI. Mean BOLD responses were visually inspected for artifacts and artefacts were excluded when

needed. Participants' block responses were fitted to a double Gaussian curve (Eq. 1) with a least squares fitting algorithm with six parameters:

$$f(x) = a * e^{-\frac{(x-b)^2}{2c^2}} - d * e^{-\frac{(x-f)^2}{2g^2}}$$

[Eq. 1]

The vascular reactivity was quantified using the mean BOLD signal amplitude, time to peak and time to baseline derived from the fitted curve. Time to peak (TTP) was defined as time from the start of the stimulus to the peak of the curve, and time to baseline (TTB) as the time between end of the stimulus and the point where the curve reaches the baseline value (note that this could also be defined as the start of the BOLD-undershoot, i.e. after TTB a negative signal changes occurs that gradually recovers to the baseline value).

Processing: BOLD-response from low temporal resolution scans

Processing of both 3T (high field) and 7T (ultra-high field) low temporal resolution scans were performed in the same manner as the high temporal resolution scans with the following differences. Slice-timing correction was performed using Fourier-space time-series phase-shifting; to investigate the possible presence of unexpected artefacts or activation, ICA-based exploratory data analysis was carried out using MELODIC [30]. After preprocessing the mean timeserie was calculated over all voxels situated in the mask of the V1 area. Subsequently, the mean BOLD response was calculated using Matlab 2016a (Mathworks, Natick, MA, USA) by averaging across the seven stimulus blocks. To calculate the outcome measures for these scans a trapezoid was fitted to the resulting mean response curve following the procedures from Dumas et al. [14, 16] The vascular reactivity was

operationalised by the mean BOLD signal amplitude, time to peak and time to baseline derived from the trapezoid.

Statistics

Statistical analyses were performed using SPSS Statistics, Version 25.0 (IBM Corp., Armonk, NY, USA). When normally distributed, continuous baseline characteristics were assessed using a student's t-test; otherwise a Mann-Whitney U test was used. Categorical baseline characteristics were assessed using Fischer's exact test.

Correlations of results between scans of the same subject were tested using Pearson's correlation and all data were plotted in a Bland-Altman plot. Differences in vascular reactivity between mutation carriers and control subjects were assessed with a regression model adjusted for age.

3. Results

Patient characteristics are summarized in *Table 1*. Mutation carriers had significantly more ICHs ($P=0.041$) and were significantly younger than the healthy participants ($P>0.001$). Possible mutation carriers did not have a significantly different age than the healthy participants ($P=0.746$). No significant differences between mutation carriers and healthy participants or between possible mutation carriers and healthy participants were found with regard to presence of hypercholesterolemia, hypertension or diabetes.

Table 1: Patient characteristics Significantly different from healthy participants at *P<0.05, **P<0.01 and ***P<0.001, Montreal Cognitive Assessment (MoCA), intracerebral hemorrhage (ICH)

	Mutation carriers	Possible mutation carriers	Healthy participants
Age	46.4±1.4***	53.7±4.16	52.5±0.8
Sex (%)	Female (100%)	Female(100%)	Female (100%)
Symptomatic (%)	21.4%*	-	-
Hypercholesterolemia	13.3%	20.0%	5.6%
Hypertension	33.3%	20.0%	25%
Diabetes	-	-	-
MoCA	27.7±0.56	27.7±2.08	27.0±0.48
ICH	3 (21.4%)*	-	-

Example mean BOLD responses as measured by the high temporal resolution scan after a 3s visual stimulus are shown in Figure 1 for a control participant, a presymptomatic mutation carrier and a symptomatic mutation carrier. All show a clear hemodynamic response, but both mutation carriers had a lower amplitude and delayed response, with the symptomatic mutation carrier having the lowest amplitude and most delayed response. Figure 2 shows subsequently the group averaged data: in both control subjects and D-CAA participants a clear BOLD response upon 3s visual activation can be observed including the well-known undershoot after the main peak. When comparing the curves, it is clear that the mutation carriers show a lower amplitude as well as a tendency to a delayed peak of the response compared to the healthy control subjects. Remarkably, the post-bolus undershoot seems to be relatively unaffected. Subsequently, the data were fitted with two Gaussian functions allowing quantification of TTP, TTB, and the amplitude (see Figure 3 as a function of participant's age and Table 2). When looking at group differences between D-CAA subjects and healthy participants, a significantly higher TTP (P<0.001), TTB (P=0.001), and a significantly lower amplitude (P<0.001) were found for D-CAA mutation carriers (statistics corrected for age). These differences appear to be highly age correlated in mutation carriers,

suggesting an aggravating effect over the disease course. These findings are in line with previous research with low temporal resolution BOLD and longer visual stimuli [16, 27].

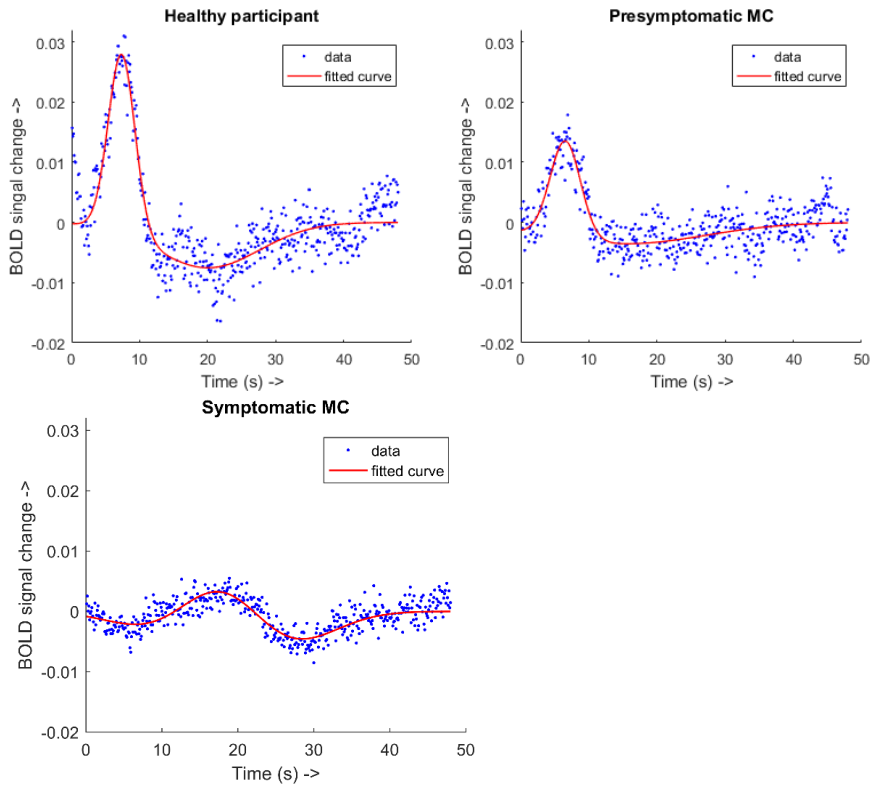


Figure 1: Fitting of double Gaussian for a healthy participant (top left), a presymptomatic D-CAA mutation carrier (MC) (top right), and a symptomatic D-CAA MC (bottom)

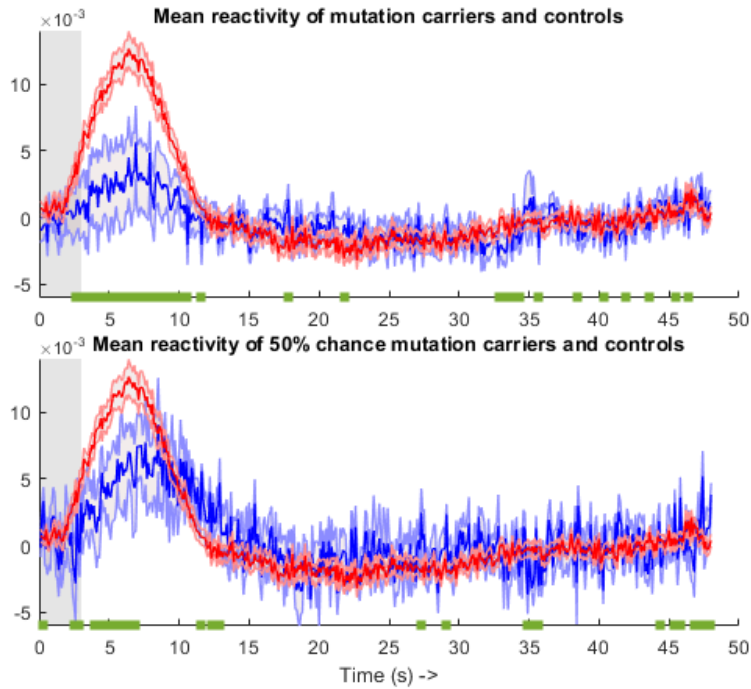


Figure 2: Mean reactivity of D-CAA participants (blue) and healthy participants (red). Shaded area indicates standard error of the mean. Grey area indicates timing of the stimulus. Green point on the x-axis depict timepoints where a significant difference was observed between D-CAA participants and control subjects ($P < 0.05$, uncorrected for multiple comparison). In 2A, the blue curve represents the participants with DNA confirmed D-CAA. In 2B, the blue curve is the mean over the 6 participants with a 50% chance of carrying the D-CAA mutation.

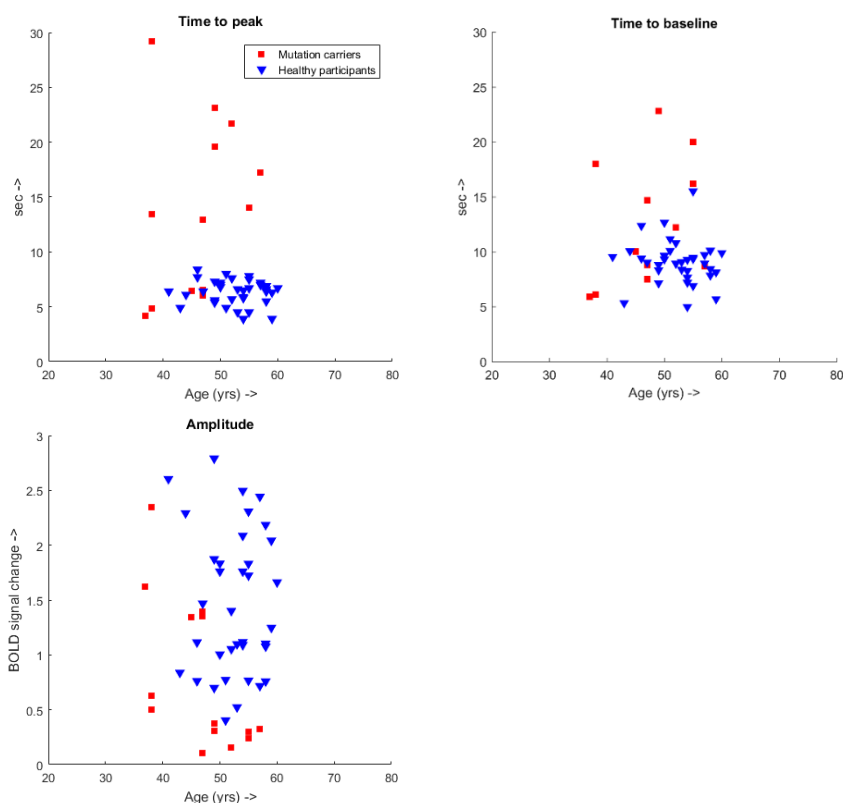


Figure 3: outcome measures (time to peak, time to baseline and amplitude of BOLD signal changes) as a function of age in mutation carriers and healthy participants.

Table 2: Mean values for time to peak, time to baseline and BOLD amplitude with SEM. Significantly different from healthy participants at * $P < 0.05$, ** $P < 0.01$ and *** $P < 0.001$,

	Mutation carriers	Healthy participants
Time to peak (s)	13.79±2.06***	6.46±0.22
Time to baseline (s)	17.22±3.44**	9.10±0.33
Amplitude (A.U.)	0.79±0.19**	1.46±0.11

Figure 4 show the mean BOLD response for three different scans, i.e. the low temporal resolution scans on 3T and 7T with a long stimulus, as well as the high

temporal resolution scan with short stimulus. This figure demonstrates clearly that the high temporal resolution protocol provides much more insight into the dynamic response, than the conventional approaches.

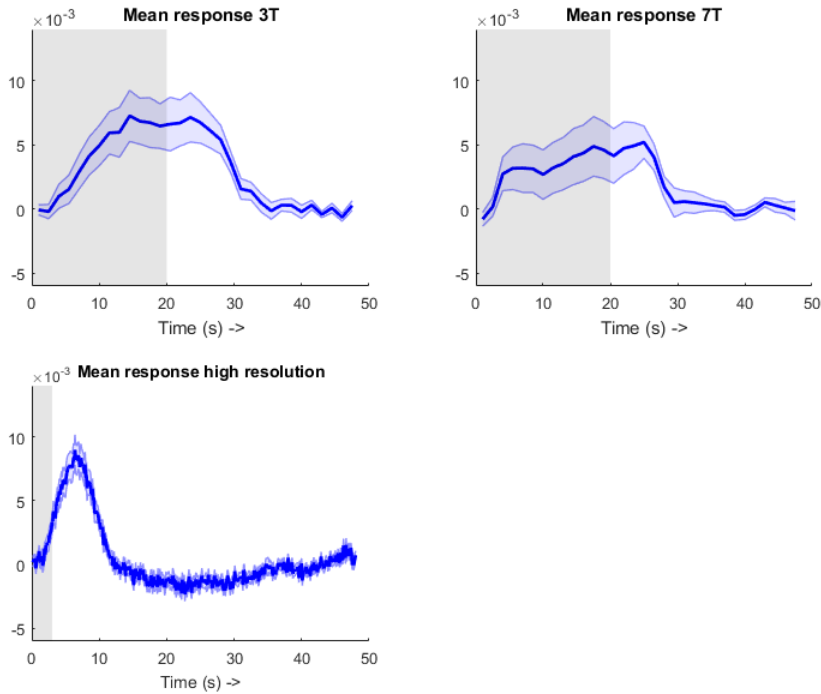


Figure 4: Mean BOLD response after stimulus in all paradigms. Grey area indicates the timing of the stimulus. On top the mean BOLD response is shown for a 20 second stimulus with low temporal resolution with 3T left and 7T right. Bottom shows the BOLD response on high temporal resolution scan with 3 second stimulus.

Whereas in most mutation carriers, a clear BOLD-response could be measured, in five an absent or only very small response was observed at 3T where vascular reactivity was measured with the long stimulus paradigm. Interestingly, the same subjects also had an absent response at 7 Tesla when measured with the 1.5s resolution sequence in combination with the long stimulus paradigm. However, in

three subjects a significant response could be identified when measured with the high temporal resolution scan in combination with a short (3s) visual stimulus. The measured BOLD responses of one of these three subjects is shown in Figure 5 for the three different protocols. In both scans with a 20s stimulus followed by a 28s rest period a noisy signal is observed, without a real discernable hemodynamic response curve, regardless of field strength (3T or 7T). This is in contrast with the third condition (3s stimulus with a 45s rest period monitored with a high temporal resolution scan) where a response is still detectable following the stimulus.

From all experiments the lower amplitude and delayed BOLD response for D-CAA subjects can be observed when comparing this group to the control group. When comparing the fitted parameters, we observed in mutation carriers high correlations for both TTP as well as for the amplitude of the BOLD-response between the short and long stimulus protocols, whereas TTB measured with high temporal resolution at 7T was not significantly correlated to TTB acquired at 3T (see Table 3). The differences between the high temporal resolution scan with short stimulus and the traditional paradigm 3T and 7T scans are further shown in the Bland-Altman plots in Figure 6.

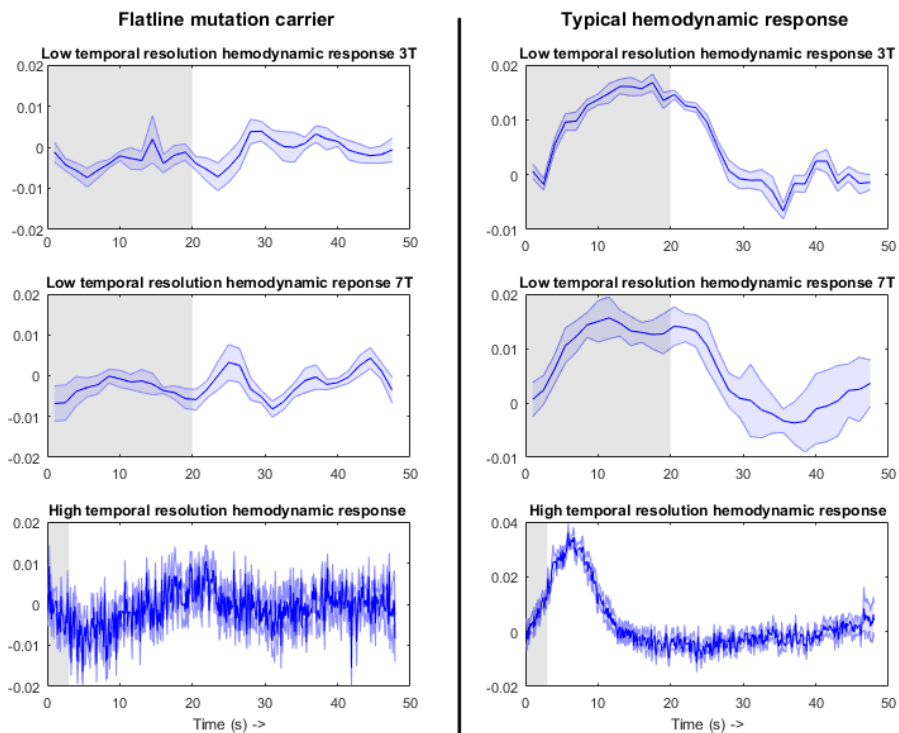


Figure 5: Hemodynamic responses shown from a symptomatic mutation carrier (left) and a more typical hemodynamic response (right). Top row shows the low temporal resolution 3T response, middle row the low temporal resolution 7T and bottom row high temporal resolution with short stimulus. Shaded area indicates standard error of the mean. Grey area indicates timing of the visual stimuli.

Table 3: Pearson's correlation of the short stimulus high temporal resolution outcome measures with those from the low temporal resolution scans measured in the mutation carrier population. Significantly correlated at * $P < 0.05$ and ** $P < 0.01$

	7T low temporal resolution	3T low temporal resolution
Time to peak	0.758**	0.724**
Time to baseline	0.544*	0.324
Amplitude	0.768**	0.565*

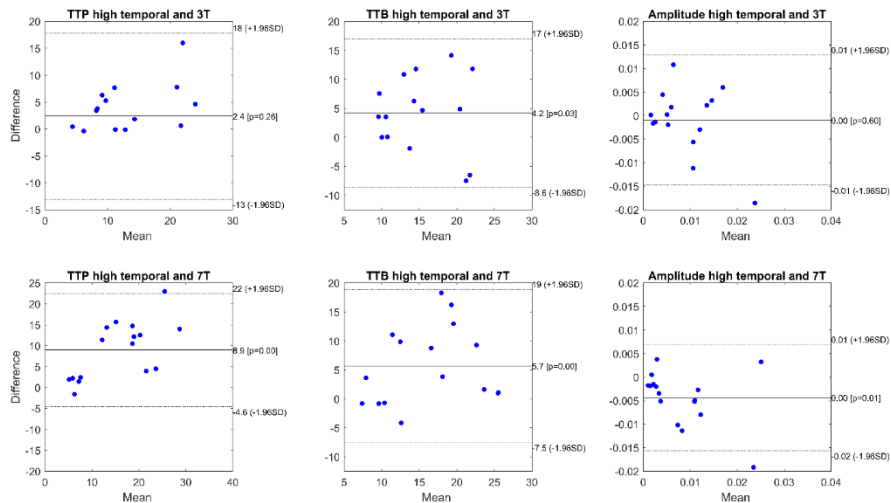


Figure 6: Bland-Altman plots for outcome measures time to peak (TTP), time to baseline (TTB) and amplitude of available mutation carriers between the high temporal resolution scan with short 3s stimulus and the traditional low temporal 3T scan (top row) with long stimulus, and the low temporal 7T scan (bottom row).

4. Discussion

In this work we explored the additional value of a high temporal resolution fMRI scan in conjuncture with a short visual stimulus to measure visually-evoked vascular reactivity in (D-)CAA patients. More specifically, we studied this in young female mutation carriers and control participants within a similar age-range. Our main findings are threefold. Firstly, we were able to detect clear hemodynamic responses and thus vascular reactivity with this method, with a higher confidence in cases where the conventional method failed in inducing a clear response. Secondly, in our patient cohort outcome measures from this new method correlated significantly with more conventional methods measured at 3T and 7T. Lastly, this new measurement protocol confirmed that the vascular response to a

visual stimulus is altered in this patient cohort of D-CAA subjects when compared to healthy control subjects, and we add to this observation that the most prominent differences occur during the main response, whereas the post-stimulus undershoot is rather similar for D-CAA and control subjects.

The high temporal resolution BOLD data in combination with a short visual stimulus provided a clear response without the need for jittering procedures of the stimulus paradigm to obtain direct insight into the hemodynamic response function (HRF). This provides the possibility to look in more detail how the BOLD response is affected by small vessel diseases, like CAA, and thus to also increase our understanding of these diseases. Contrarily to our expectation, we also observed that it allowed more clear responses in patients who were 'non-responders' or 'flat-liners' at our traditional low-temporal sequence with longer stimulus blocks on 3T and 7T. For example, with the high temporal resolution protocol we could clearly observe a hemodynamic response curve in the symptomatic D-CAA carrier shown in Figure 1 and 5, although such a response could not be observed by the traditional approaches [16-18]. The absence of a clear response following a long stimulus paradigm, was both observed at 3T and 7T. This is an important finding, because a too low BOLD-response, also makes it impossible to accurately measure the timing parameters. This implies that these timing parameters could not be used to follow disease progression in the most affected CAA subjects and would limit the value of these in e.g. treatment trials. In previous studies, we did show that TTP was the parameter most significantly related to disease progression in D-CAA subjects [17, 18]. Since this response was absent in 5 subjects when measured with a long stimulus paradigm both at 3T and 7T, the higher sensitivity to the BOLD effect at stronger magnetic field strength MRI scanners cannot alone explain these findings [31]. However, two main differences exist between the two approaches: both the duration of the visual stimulus (3s versus 20s) as well as the temporal resolution (100ms versus 1.5s) were different. It is known that the BOLD response shows non-linear behavior with

respect to stimulus duration. In healthy subjects, shorter stimulus durations have shown to result in a stronger HRF, whereas a longer stimulus durations would still lead to higher BOLD-responses due to the cumulative effect over the longer stimulus period [32-35]. The fact that in our patients shorter duration led to a more clear response might point towards microvascular changes that impact this non-linear behavior, e.g. the cumulative response might be less effective. In our opinion it is less likely that the higher temporal resolution could explain the difference in observations as it is clear from *Figure 5* that the BOLD-signal was found to be increased for a much longer period than the 1.5s temporal resolution.

Our second finding is that the obtained reactivity parameters with the high temporal resolution BOLD scan and short stimulus duration, correlated significantly with the lower temporal resolution protocols at 3T and 7T that both applied a longer stimulus. This high degree of correlation was found for TTP and BOLD amplitude, whereas the time to baseline was less correlated. This may suggest that this last-mentioned variable is inherently more noisy and difficult to measure. This is in agreement with previous research that reported a poorer reproducibility for time to baseline, even in healthy adults, when measured with the more traditional approach [18]. It is important to mention that these results also can be considered as strong evidence that TTP and amplitude of the BOLD response could act as valuable outcome markers in clinical studies: the strong correlation between 3T and 7T parameters, which are per definition measured in different sessions, proves temporal stability, whereas the correlation also show insensitivity to exact fitting procedures, since the short stimulus data is evaluated with a different model (two Gaussian function) than the long stimulus data (trapezoid).

In agreement with findings of earlier studies on vascular reactivity in D-CAA, we found decreased amplitude and delayed timing parameters in our D-CAA participants compared to healthy control participants [13-16]. Additionally, with

the shorter visual stimulus paradigm and high temporal resolution acquisition, we were able to more accurately visualize the hemodynamic response. For example, the post-activation undershoot could now clearly be observed and interestingly the most prominent differences in the mean hemodynamic response are happening during the peak (positive) response, rather than during the undershoot (*Figure 2*). The origin of the post-activation undershoot has been fiercely debated over the last two decades with slow recovery of CBV (the ‘balloon model’ [35]) and sustained CMRO₂-increases (possibly in combination with CBF decreases) as the two dominant hypotheses [36]. Within the balloon model, the venous CBV is thought to be relatively increased during the undershoot, and this could explain our observation that the post-activation undershoot was less affected in CAA, because CAA-pathology is mainly located on the arterial side of the vascular bed. This preferential arterial location has been corroborated in post-mortem pathology of amyloid depositions [37], as well as by the absence of anatomical changes of the venous vasculature in D-CAA patients [38], as opposed to observations in Alzheimer’s patients [39]. However, literature seems to side on the second hypothesis, which could also explain our observations in the sense that CAA could mainly affect the vasodilatory capacity of the vascular bed leading to the peak BOLD response, whereas the recovery period with only minor CBF decreases (if any) remain relatively unaffected. However, further research is required to further elucidate such claims.

Our newly proposed approach for measuring vascular reactivity in CAA, has also some important limitations, which need to be discussed. First of all, the high temporal resolution scans consists of only a single, coronal slice and is therefore more susceptible to motion. Not only does this limit the possibility for retrospective motion correction, but motion would also lead to strong increases in signal intensity when fully relaxed longitudinal magnetization (“fresh spins”) of neighboring tissue would enter the imaging slice. This effect, however, can also be exploited to identify motion artefacts followed by exclusion of data-points from

the mean timeseries. However, this scanning approach may be less suitable in restless populations, since too little data may remain to obtain robust hemodynamic response measurements. Another limitation of a single slice approach, is that such a method is more sensitive to planning by the scanner operator, due to its limited coverage. Slightly different planning will lead to varying inclusion of cortical layers and structures into the field-of-view. It remains to be elucidated whether or not this has a substantial impact on outcome measures and assessing the reproducibility would be an important topic for future research. The fact that the amplitude and TTP did correlate significantly correlated with the outcome parameters of more traditional approaches, might point to a limited influence of such planning variations.

In conclusion, we showed that by monitoring the BOLD response to a short visual stimulus with high temporal resolution scanning, robust hemodynamic responses can be obtained, showing even responses in subjects without clear responses on more conventional protocols. The new data support conclusions from earlier studies that the hemodynamic response in D-CAA mutation carriers is both decreased as well as delayed. We add to these observations, that the post-stimulus undershoot is less affected than the main (positive) BOLD-response. Potentially additional information may be extracted due to the higher sampling rate (150-200x more timepoints) and improved monitoring of the complete BOLD-response.

REFERENCES

1. Jäkel, L., et al., *Prevalence of cerebral amyloid angiopathy: A systematic review and meta-analysis*. *Alzheimers Dement*, 2022. **18**(1): p. 10-28.
2. Biffi, A. and S.M. Greenberg, *Cerebral amyloid angiopathy: a systematic review*. *J Clin Neurol*, 2011. **7**(1): p. 1-9.
3. Knudsen, K.A., et al., *Clinical diagnosis of cerebral amyloid angiopathy: validation of the Boston criteria*. *Neurology*, 2001. **56**(4): p. 537-9.
4. van Rooden, S., et al., *Descriptive analysis of the Boston criteria applied to a Dutch-type cerebral amyloid angiopathy population*. *Stroke*, 2009. **40**(9): p. 3022-7.
5. Rodrigues, M.A., et al., *The Edinburgh CT and genetic diagnostic criteria for lobar intracerebral haemorrhage associated with cerebral amyloid angiopathy: model*

- development and diagnostic test accuracy study. *The Lancet. Neurology*, 2018. **17**(3): p. 232-240.
6. van Etten, E.S., et al., *Sensitivity of the Edinburgh Criteria for Lobar Intracerebral Hemorrhage in Hereditary Cerebral Amyloid Angiopathy*. *Stroke*, 2020. **51**(12): p. 3608-3612.
 7. Charidimou, A., et al., *The Boston criteria version 2.0 for cerebral amyloid angiopathy: a multicentre, retrospective, MRI-neuropathology diagnostic accuracy study*. *Lancet Neurol*, 2022. **21**(8): p. 714-725.
 8. Fotiadis, P., et al., *Cortical atrophy in patients with cerebral amyloid angiopathy: a case-control study*. *Lancet Neurol*, 2016. **15**(8): p. 811-819.
 9. Subotic, A., et al., *Cortical Thickness and Its Association with Clinical Cognitive and Neuroimaging Markers in Cerebral Amyloid Angiopathy*. *Journal of Alzheimer's disease : JAD*, 2021. **81**(4): p. 1663-1671.
 10. Wermer, M.J.H. and S.M. Greenberg, *The growing clinical spectrum of cerebral amyloid angiopathy*. *Current Opinion in Neurology*, 2018. **31**(1): p. 28-35.
 11. Reijmer, Y.D., et al., *Relationship between white matter connectivity loss and cortical thinning in cerebral amyloid angiopathy*. *Human brain mapping*, 2017. **38**(7): p. 3723-3731.
 12. Alonzo, N.C., et al., *Progression of cerebral amyloid angiopathy: accumulation of amyloid-beta40 in affected vessels*. *J Neuropathol Exp Neurol*, 1998. **57**(4): p. 353-9.
 13. Switzer, A.R., et al., *Longitudinal decrease in blood oxygenation level dependent response in cerebral amyloid angiopathy*. *NeuroImage. Clinical*, 2016. **11**: p. 461-467.
 14. Dumas, A., et al., *Functional MRI Detection of Vascular Reactivity in Cerebral Amyloid Angiopathy*. *Annals of neurology*, 2012. **72**(1): p. 76-81.
 15. Smith, E.E., et al., *Impaired visual evoked flow velocity response in cerebral amyloid angiopathy*. *Neurology*, 2008. **71**(18): p. 1424-30.
 16. van Opstal, A.M., et al., *Cerebrovascular function in pre-symptomatic and symptomatic individuals with hereditary cerebral amyloid angiopathy: a case-control study*. *The Lancet. Neurology*, 2017. **16**(2): p. 115-122.
 17. van Dijk, S.E., et al., *Longitudinal Progression of Magnetic Resonance Imaging Markers and Cognition in Dutch-Type Hereditary Cerebral Amyloid Angiopathy*. *Stroke*, 2022. **53**(6): p. 2006-2015.
 18. van Dijk, S.E., et al., *Aging Effect, Reproducibility, and Test-Retest Reliability of a New Cerebral Amyloid Angiopathy MRI Severity Marker-Cerebrovascular Reactivity to Visual Stimulation*. *J Magn Reson Imaging*, 2022.
 19. Rasing, I., et al., *Occipital Cortical Calcifications in Cerebral Amyloid Angiopathy*. *Stroke*, 2021. **52**(5): p. 1851-1855.
 20. Johnson, K.A., et al., *Imaging of amyloid burden and distribution in cerebral amyloid angiopathy*. *Ann Neurol*, 2007. **62**(3): p. 229-34.
 21. Vinters, H.V. and J.J. Gilbert, *Cerebral amyloid angiopathy: incidence and complications in the aging brain. II. The distribution of amyloid vascular changes*. *Stroke*, 1983. **14**(6): p. 924-8.
 22. Nortley, R., et al., *Amyloid β oligomers constrict human capillaries in Alzheimer's disease via signaling to pericytes*. 2019. **365**(6450): p. eaav9518.
 23. Walz, J.M., et al., *Simultaneous EEG-fMRI Reveals a Temporal Cascade of Task-Related and Default-Mode Activations During a Simple Target Detection Task*. *NeuroImage*, 2014. **102**(0 1): p. 229-239.
 24. Jenkinson, M., et al., *Improved optimization for the robust and accurate linear registration and motion correction of brain images*. *Neuroimage*, 2002. **17**(2): p. 825-41.
 25. Jenkinson, M. and S. Smith, *A global optimisation method for robust affine registration of brain images*. *Med Image Anal*, 2001. **5**(2): p. 143-56.
 26. Andersson JLR, J.M., Smith S *Non-linear registration, aka spatial normalisation*. . FMRIB technical report TR07JA2, 2010.
 27. van Harten, T.W., et al., *Impact of ROI definition on visual stimulation based cerebral vascular reactivity fMRI with a special focus on applications in Cerebral Amyloid Angiopathy*. *NMR Biomed*, 2023: p. e4916.

28. Smith, S.M., *Fast robust automated brain extraction*. Hum Brain Mapp, 2002. **17**(3): p. 143-55.
29. Woolrich, M.W., et al., *Temporal autocorrelation in univariate linear modeling of fMRI data*. Neuroimage, 2001. **14**(6): p. 1370-86.
30. Beckmann, C.F. and S.M. Smith, *Probabilistic independent component analysis for functional magnetic resonance imaging*. IEEE Trans Med Imaging, 2004. **23**(2): p. 137-52.
31. Thulborn, K.R., et al., *Oxygenation dependence of the transverse relaxation time of water protons in whole blood at high field*. Biochim Biophys Acta, 1982. **714**(2): p. 265-70.
32. Lewis, L.D., et al., *Stimulus-dependent hemodynamic response timing across the human subcortical-cortical visual pathway identified through high spatiotemporal resolution 7T fMRI*. Neuroimage, 2018. **181**: p. 279-291.
33. Yeşilyurt, B., K. Uğurbil, and K. Uludağ, *Dynamics and nonlinearities of the BOLD response at very short stimulus durations*. Magn Reson Imaging, 2008. **26**(7): p. 853-62.
34. Buxton, R.B., et al., *Modeling the hemodynamic response to brain activation*. Neuroimage, 2004. **23 Suppl 1**: p. S220-33.
35. Buxton, R.B., E.C. Wong, and L.R. Frank, *Dynamics of blood flow and oxygenation changes during brain activation: the balloon model*. Magn Reson Med, 1998. **39**(6): p. 855-64.
36. van Zijl, P.C., J. Hua, and H. Lu, *The BOLD post-stimulus undershoot, one of the most debated issues in fMRI*. Neuroimage, 2012. **62**(2): p. 1092-102.
37. Vonsattel, J.P., et al., *Cerebral amyloid angiopathy without and with cerebral hemorrhages: a comparative histological study*. Ann Neurol, 1991. **30**(5): p. 637-49.
38. van Harten, T.W., et al., *Brain Deep Medullary Veins on 7T MRI in Dutch-Type Hereditary Cerebral Amyloid Angiopathy*. J Alzheimers Dis, 2022. **90**(1): p. 381-388.
39. Bouvy, W.H., et al., *Abnormalities of Cerebral Deep Medullary Veins on 7 Tesla MRI in Amnesic Mild Cognitive Impairment and Early Alzheimer's Disease: A Pilot Study*. J Alzheimers Dis, 2017. **57**(3): p. 705-710.

Chapter 5

Quantitative measurement of cortical Superficial Siderosis in Cerebral Amyloid Angiopathy

T.W. van Harten, E.A. Koemans, S. Voigt, I. Rasing, M.J.P. van Osch, M.A.A. van Walderveen, M.J.H. Wermer

This chapter has been published Neuroimage Clin. 2023; 38: 103447. doi: 10.1016/j.nicl.2023.103447.

ABSTRACT

Cerebral amyloid angiopathy (CAA) is a cerebrovascular disease affecting the small arteries in the brain with hallmark depositions of amyloid- β in the vessel wall, leading to cognitive decline and intracerebral hemorrhage (ICH). An emerging MRI marker for CAA is cortical superficial siderosis (cSS) as it is strongly related to the risk of (recurrent) ICH. Current assessment of cSS is mainly done on T2*- weighted MRI using a qualitative score consisting of 5 categories of severity which is hampered by ceiling effects. Therefore, the need for a more quantitative measurement is warranted to better map disease progression for prognosis and future therapeutic trials. We propose a semi-automated method to quantify cSS burden on MRI and investigated it in 20 patients with CAA and cSS. The method showed excellent inter-observer (Pearson's 0.991, $P < 0.001$) and intra-observer reproducibility (ICC 0.995, $P < 0.001$). Furthermore, in the highest category of the multifocality scale a large spread in the quantitative score is observed, demonstrating the ceiling effect in the traditional score. We observed a quantitative increase in cSS volume in two of the 5 patients who had a 1 year follow up, while the traditional qualitative method failed to identify an increase because these patients were already in the highest category. The proposed method could therefore potentially be a better way of tracking progression.

In conclusion, semi-automated segmenting and quantifying cSS is feasible and repeatable and may be used for further studies in CAA cohorts.

1. INTRODUCTION

Cerebral amyloid angiopathy (CAA) is a neurovascular disease characterized by progressive accumulation of the protein amyloid β in the walls of small cortical and leptomeningeal vessels. CAA is a common cause of lobar intracerebral hemorrhage (ICH) and cognitive decline in the elderly.[1-3] A diagnosis of probable or possible CAA can be established with the Boston criteria which are mainly based on clinical symptoms together with hemorrhagic and white matter MRI markers. [4, 5] An important MRI marker of CAA is cortical superficial siderosis (cSS). [6, 7] Although the cause of cSS is not entirely clear, the prevailing hypothesis include previous acute convexity subarachnoid hemorrhage leading to hemosiderin deposited in the subpial space [6]. On T2(*) or susceptibility weighted MRI, cSS is visible as a hypointense band following the outer layer of the cortex. Presence, extent and progression of cSS on MRI are all associated with increased risk of future ICH [8-11], and are considered important prognostic markers in clinical practice.

For scoring the severity of cSS, the cSS multifocality rating scale has been developed and this score has extensively been employed to evaluate and monitor extent and progression of cSS. In this scale, each hemisphere is scored separately for cSS and subsequently the scores of both hemispheres are added to yield a total multifocality score ranging from 0 – 4. Although the multifocality rating scale has proven to be an important predictor of future ICH risk over its entire range [12], it cannot be used to monitor future progression of cSS in patients who are already categorized as having severe and multifocal cSS (ceiling effect). Also, subtle increases in cSS within sulci that are already affected by cSS will not be reflected in the multifocality scale.

A more sensitive and quantitative measure of cSS is therefore much needed. A score reflecting the total cortical area affected by cSS seems a logical extension of the visual score that would not suffer from the drawbacks of a categorical score.

The aim of the current study is to develop a semi-automatic tool for the quantification of cSS in patients with CAA.

2. MATERIALS AND METHODS

For this study we used MRI data from patients with Dutch-type hereditary CAA (D-CAA) and sporadic CAA (sCAA) who participated in two ongoing longitudinal natural history studies (FOCAS and AURORA) in the Leiden University Medical Center (LUMC, Leiden, The Netherlands). MRI data from 20 patients (15 D-CAA and 5 sCAA) with a varying range of cSS severity on the multifocality rating scale were selected. Of the 5 sCAA patients 1 year follow-up scans were available. Both FOCAS and AURORA are performed in accordance with the declaration of Helsinki. Informed consent was obtained from all participants and study protocols were approved by the local IRB.

All participants were scanned on a 3.0 Tesla MRI scanner (Philips Achieva, Best, the Netherlands) and data was acquired using a standard 32-channel head coil. The protocol included SWI acquired with the following parameters: 4 echoes, TR/first TE/echospace of 31/7.2/6.2ms, flip angle 17 degrees, 130 slices and an FOV of 230 x 190 x 130 mm with a voxel size of 0.6 x 0.6 x 1 mm resulting in a scan duration of 3:31 min. cSS was assessed using the multifocality scale as described in Charidimou *et al.*[12] In short: each hemisphere was scored separately with a score of 0-2; where 0 represents no cSS present, 1 represents one sulcus or up to three immediately adjacent sulci with cSS and 2 represents two or more non-adjacent sulci or more than 3 adjacent sulci with cSS. Scores of both hemispheres are added to get a 0-4 scale. cSS potentially connected to lobar ICH were not included in this rating.

2.1 Development and performance of the cSS tool

SWI-images were processed using a custom pipeline created in MeVisLab 3.2 (Bremen, Germany). Images were preprocessed with a 2D-vesselness filter using a single scale with a sigma of one voxel [13]. In short, the vesselness filter is based upon the Hessian matrix with the output showing how similar the local

neighborhood is to a hypointense tubular structure. The resulting segmentation was then visually evaluated and seed points for a 3D-6-Neighborhood (x,y,z) growing region algorithm were placed within a cSS region. The resulting mask was again visually inspected, corrected for any false positives and the volume of cSS was calculated. This semi-automatic segmentation process was executed by an experienced rater (E.K., 5 years of experience in the field), blind to clinical data, on two separate occasions within a four-month period, to assess intra-observer agreement. The code for this tool will be made available upon reasonable request. Reproducibility between these sessions was determined by calculating the Pearson's correlation coefficient on the resulting cSS volume using SPSS software version 25.0 (*IBM*, Chicago, IL, USA). Agreement was also plotted in an R^2 correlation plot and a Bland-Altman plot in Matlab 2016a (*Mathworks*, Natick, MA, USA). Furthermore, to assess inter-observer agreement, a second experienced rater (S.V., 5 years of experience in the field) rated the same dataset as the first rater, blind to clinical data and the outcome of the assessment by the first rater. The two raters were compared with an absolute agreement intraclass correlation coefficient (ICC) on the resulting cSS volume using SPSS software version 25.0 (*IBM*, Chicago, IL, USA). The second rater was trained on example data of three patients (not included in the final evaluation dataset) while providing the output of the first rater as ground truth.

To assess to what extent segmentations were in exact agreement on the voxel-level, the Dice similarity coefficient (DSC) (see Eq. 1: area of overlapping voxels divided by the sum of the areas of both ROIs) [14] was calculated:

$$DSC = \frac{2 * (|ROI_{observation1}| \cap |ROI_{observation2}|)}{|ROI_{observation1}| + |ROI_{observation2}|}$$

[Eq. 1]

Finally, the volumes of cSS measured with the newly developed tool were plotted against the standard cSS multifocality rating scale.

To assess the effectiveness of such a quantitative marker for follow-up research, the 1-year follow-up scans of the sCAA patients were processed by the same experienced rater (E.K.), blind to any clinical data. These volumes were compared to the baseline volumes and to a previous developed visual progression scale that has been derived and validated to be sensitive to change over time and predictive of future ICH[15].

3. RESULTS

Mean age of the patients was 60 ± 13 years (54 ± 9 years for D-CAA and 79 ± 4 years for sCAA) and 35% were women. Fourteen of the 20 patients had a history of ICH and three a history of TFNEs.

Processing of the SWI files by use of the 2D-vesselness filter resulted in a suppression of all non-tubular shapes; as shown on the white overlay in the middle pane of *Figure 1*. This middle pane shows that application of this vesselness filter allows segmentation of all cSS, but also of several other hypointense tubular structures such as some veins. A slice of the same patient, processed by the vesselness filter, at the height of the Sylvian fissure is shown in Supplementary data, only false positives are seen in this figure. Placement of seed points within the cSS and execution of the growing region algorithm resulted in a good segmentation of the cSS lesions with the resulting mask shown on the right in *Figure 1*. Intra-observer agreement was excellent for cSS volume (Pearson's 0.991, $P < 0.001$), high for r^2 (0.98) and agreement was good in the Bland Altman-plot (*Figure 2*). Also, inter observer agreement was excellent with an ICC of 0.995 ($P < 0.001$, 95%CI: 0.984-0.998), a high r^2 (0.98) and good agreement in the Bland Altman-plot (*Figure 3*).

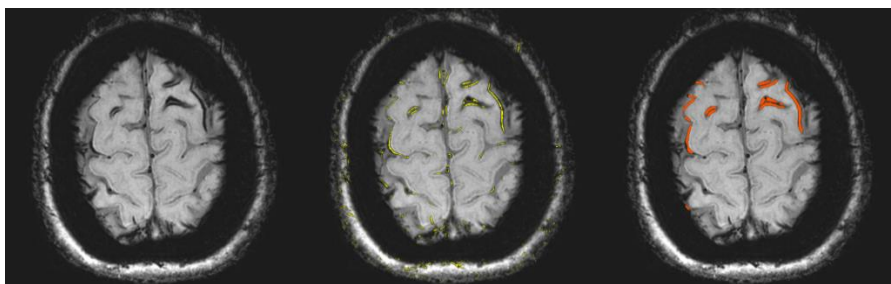


Figure 1: Susceptibility weighted scan of a patient with CAA showing cSS in multiple sulci in both hemispheres. On the left panel the unprocessed image is shown. On the middle panel, the image processed with a 2D-vesselness filter is shown with voxels in yellow that have an above threshold value of vesselness, i.e. similarity to a hypointense tubular structure. In this

initial segmentation, many false positives can be observed. Subsequently to this initial segmentation seed-points were placed followed by a 3D region-growing algorithm. On the right panel, the resulting segmentation is shown in red highlighted areas. These are then used for further analysis.

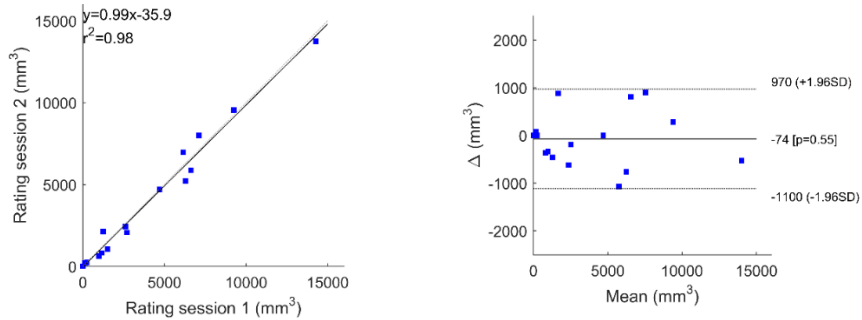


Figure 2: Correlation and Bland Altman plot for volumes recorded in rating session 1 versus rating session 2. The correlation plot shows good agreement and in the Bland Altman plot no large outliers or trends are observed between the two scoring sessions.

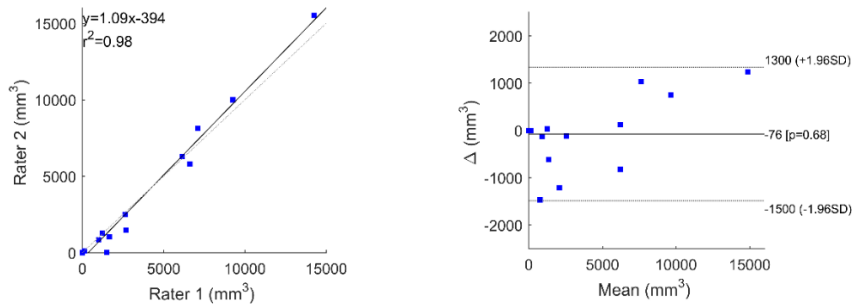


Figure 3: Correlation and Bland Altman plot for volumes recorded by rater 1 versus rater 2. The correlation plot shows good agreement and in the Bland Altman plot no large outliers or trends are observed between the two raters.

While total cSS volume was highly reproducible, the voxels included in segmentations on separate occasions were not always the same (mean DSC 0.75 ± 0.15); we consider this DSC values a reflection of good agreement, due to the sparseness and small sizes of the segmented areas.

According to the cSS multifocality rating scale, two of the 20 participants were classified as score 1, one as 2, five as 3 and eight as 4. The relationship between this categorical classification and the quantified cSS volumes is shown in *Figure 4*. The eight participants who were classified as having the most severe cSS score (score 4) showed a wide range of quantified cSS volumes, ranging from 2.7 mL to 14.3 mL. Also, one individual showed a high quantified cSS volume despite being classified in the third category, because of extensive cSS mainly localized in the right hemisphere (adding two points to the categorical score), while the left hemisphere only had a minor quantity of cSS (adding only one additional point).

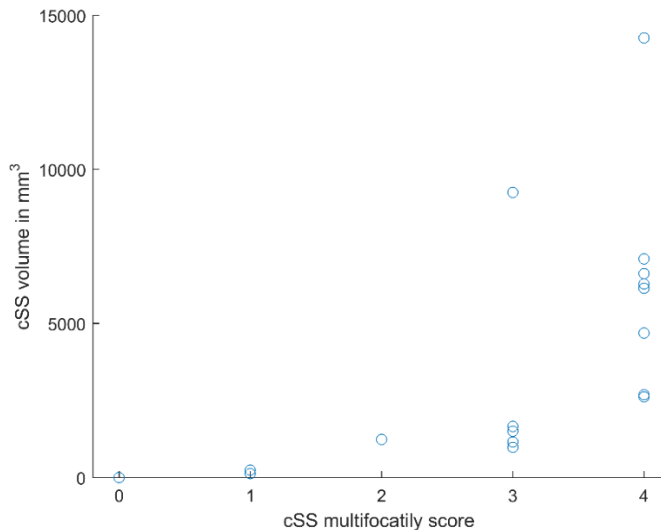


Figure 4: Volume of cortical superficial siderosis plotted against the multifocality rating score; in the highest multifocality rating scale categories a large spread in cSS volume is

demonstrated, suggesting that in patients with severe cSS, this segmentation and quantification method may prove to be a valuable tool in tracking progression.

Results of segmentation of baseline and follow-up scans are shown in *Figure 5*: increase in volume as an increase in cSS was found as described the progression scale [15] shown in blue, whereas scans absent of this observation are shown in red. Two of the patients who showed an increase in cSS were already in category 4 of the multifocality scale[12].

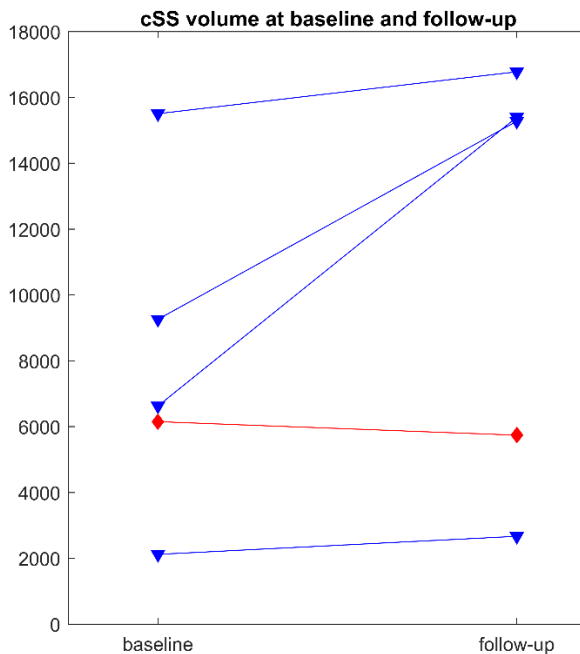


Figure 5: volumes of cSS segmentation at baseline and follow-up of the 5 sCAA patients. Blue triangles indicate patients in whom an increase in cSS was found as described by the progression scale, red diamonds indicate subjects in whom no cSS increase was reported. A marked increase in volume is found only for those patients in whom the neuroradiologist reported an increase in cSS.

4. DISCUSSION

Our proof-of-principle study demonstrates in a group of patients with CAA with varying cSS severity that quantification of cSS volume can be achieved in a reproducible way by a relatively simple, semi-automatic tool based upon region growing of vesselness-enhanced SWI images. Clear advantages of cSS volume quantification as compared to a categorical scale are twofold: it does not exhibit a ceiling effect and it can also identify minor progression. Quantification of cSS volume is important as many patients with advanced CAA readily fall into the highest category of the multifocality rating scale; further progression of cSS in these patients cannot be reflected in this scale and will therefore remain unnoticed. Also, our study showed that in patients with the highest score on the categorical scale a wide variability of cSS volumes was present, suggesting that subjects in this category are more heterogeneous than implied by their similar cSS score. Furthermore, in the two patients in whom our neuroradiologist identified an increase in cSS on the 1-year follow-up scans, our tool also identified an increase in volume, even while the categorical scale remained unchanged since these subjects were already in the highest category. Whether the use of our quantitative score will show that these subjects also differ with respect to clinical disease progression needs to be studied in future research.

The semi-automatic approach enables quantification of cSS in an accurate manner and can be applied accurately by experienced raters with good agreement: usage of this method showed excellent intra- and inter-observer reliability. Our data suggests that the automatic segmentation using a 2D-vesselness filter combined with a 3D growing region algorithm, with elimination of false positives by a human rater, yields sufficient quality to be used in further clinical validation studies.

While this method of quantification seems highly relevant in cSS related research, the added value in clinical practice is hard to assess. This caveat is similar to the multifocality scale which also only finds its place in a research setting. Furthermore, as a proof of principle paper we did not include any correlations with

clinical data or outcomes, and therefore it is unclear if the extra time spent making segmentations is warranted and feasible for clinical practice.

A weakness of MRI is that the hypointense area caused by cSS is dependent on field strength, sequence-parameters and post-processing approaches. [16, 17] Therefore, our quantitative score may be difficult to compare between centers and it would be important to standardize imaging parameters and post-processing. Luckily, many patients will be followed-up in a single center, making it easier to guarantee consistent identification of cSS volume change. To increase comparability of scans obtained with different settings, one could envision calibration scales based upon MR-physics theory predicting the relative amplification of the hypointense area due to the presence of hemosiderin. However, magnetic susceptibility characteristics of hemosiderin are variable and the influence on the magnetic field distribution will be shape and orientation dependent [18], ultimately limiting the performance of such recalibration efforts. Alternatively, repeated in vivo scanning sessions could be used for such a calibration scale, or measurements on dedicated phantoms. Another option would be to use internal calibration measures, such as percentage of total sulci length affected. Such an internally calibrated measure could be an improvement over volume, since the influence of sequence parameters and field strengths will be more pronounced in the perpendicular, than in the longitudinal direction of the sulcus. Furthermore, measures like surface area of the cortex affected may prove to be a more useful or accurate measure than volume. However, this will almost certainly lead to an increase in processing time and the chance of errors in segmentation of the sulci and cortical surface, especially in a population with many lobar bleeds. From our largely cross-sectional dataset it is not possible to determine which of these measures would perform best with respect to clinical outcome and/or as a measure of disease progression. However, the cSS segmentations of our method, prior to quantification of the volume, can be used as input for more advanced processing and subsequently provide more useful

outcome measures, like surface area. As our study was conducted on a single center 3T system, this impact has to be investigated in other studies, for example in multi-center studies on CAA progression.

Our study has a relatively small sample size. However, despite this small sample size we are able to show a large heterogeneity in the higher categories of the multifocality scale, and we are able to show that our novel method can indeed identify progression. A more accurate assessment of cSS progression might improve prediction of future ICH which is of clinical importance for example to better inform patients about prognosis or in case patients are on antiplatelet therapy or on anticoagulation. Also, for research purposes, a quantitative score might be preferable for example when progression of cSS is used as a biomarker. Future studies are needed to investigate the clinical relevance of our new scale.

Another limitation of this method is that it can be more time consuming than applying a multifocality scale: in the high resolution images produced in this MRI protocol processing may take up to an hour in patients with extensive cSS. Furthermore, we also did not assess the scan-rescan variability of the method. However, due to the high quality and resolution of the scans used in our protocol we expect the scan-rescan variability to be less important than the inter-observer variability. Should this method be applied to data with a lower resolution, planning and partial voluming effects will start to have an impact on the final quantification. Also, no one-to-one comparison was made between manual segmentations and cSS-segmentations based on our semi-automatic approach. However, because both methods are observer-based, little deviations should be expected. Future studies will also have to elucidate the association between quantified cSS volume and other MRI markers of CAA pathology, together with its prognostic value for future ICH risk in clinical practice. The availability of cSS masks also present the possibility of further research with respect to localized clinical features (i.e. distance of other pathological processes to cSS), as well as even more detailed

analyses of cSS (i.e. shape features). Furthermore, longitudinal studies performed in similar scanning conditions potentially can further show how cSS progresses in the course of CAA. Lastly, the additional *clinical* value of quantification of cSS compared with the categorical classification for prognosis has to be investigated.

In conclusion, semi-automatic segmentation and quantification of cSS on SWI-MRI is feasible and reproducible and may be used as a more continuous variable of cSS severity, although it should only be used on images acquired under similar conditions.

Acknowledgements

This research has been made possible by the Dutch Heart Foundation and the Netherlands Organisation for Scientific Research (NWO), as part of their joint strategic research programme: “Earlier recognition of cardiovascular diseases”.

This project is partially financed by the PPP Allowance made available by Top Sector Life Sciences & Health to the Dutch Heart Foundation to stimulate public–private partnerships. This work is further supported by a grant of the Dutch Heart Foundation to M.J.H. Wermer (2016T86).

References

1. Vinters, H.V., *Cerebral amyloid angiopathy. A critical review*. Stroke, 1987. **18**(2): p. 311-24.
2. Charidimou, A., et al., *Emerging concepts in sporadic cerebral amyloid angiopathy*. Brain, 2017. **140**(7): p. 1829-1850.
3. Jäkel, L., et al., *Prevalence of cerebral amyloid angiopathy: A systematic review and meta-analysis*. Alzheimers Dement, 2022. **18**(1): p. 10-28.
4. Knudsen, K.A., et al., *Clinical diagnosis of cerebral amyloid angiopathy: validation of the Boston criteria*. Neurology, 2001. **56**(4): p. 537-9.
5. Charidimou, A., et al., *The Boston criteria version 2.0 for cerebral amyloid angiopathy: a multicentre, retrospective, MRI-neuropathology diagnostic accuracy study*. Lancet Neurol, 2022. **21**(8): p. 714-725.
6. Linn, J., et al., *Prevalence of superficial siderosis in patients with cerebral amyloid angiopathy*. Neurology, 2010. **74**(17): p. 1346-50.
7. Wermer, M.J.H. and S.M. Greenberg, *The growing clinical spectrum of cerebral amyloid angiopathy*. Current Opinion in Neurology, 2018. **31**(1): p. 28-35.
8. Charidimou, A., et al., *Cortical superficial siderosis and first-ever cerebral hemorrhage in cerebral amyloid angiopathy*. Neurology, 2017. **88**(17): p. 1607-1614.
9. Greenberg, S.M. and E.E. Smith, *Implications of cortical superficial siderosis in CAA. Superficial relationships*, 2019. **92**(8): p. 360-361.
10. Greenberg, S.M., et al., *The clinical spectrum of cerebral amyloid angiopathy: presentations without lobar hemorrhage*. Neurology, 1993. **43**(10): p. 2073-9.
11. Charidimou, A., et al., *Cortical Superficial Siderosis Evolution*. Stroke, 2019. **50**(4): p. 954-962.
12. Charidimou, A., et al., *Cortical superficial siderosis multifocality in cerebral amyloid angiopathy: A prospective study*. Neurology, 2017. **89**(21): p. 2128-2135.
13. Frangi, A.F., et al. *Multiscale vessel enhancement filtering*. 1998. Berlin, Heidelberg: Springer Berlin Heidelberg.
14. Bonar, D.C., et al., *Graphical analysis of MR feature space for measurement of CSF, gray-matter, and white-matter volumes*. J Comput Assist Tomogr, 1993. **17**(3): p. 461-70.
15. Pongpitakmetha, T., et al., *Cortical superficial siderosis progression in cerebral amyloid angiopathy: Prospective MRI study*. Neurology, 2020. **94**(17): p. e1853-e1865.
16. Nandigam, R.N., et al., *MR imaging detection of cerebral microbleeds: effect of susceptibility-weighted imaging, section thickness, and field strength*. AJNR Am J Neuroradiol, 2009. **30**(2): p. 338-43.
17. Greenberg, S.M., et al., *Cerebral microbleeds: a guide to detection and interpretation*. The Lancet. Neurology, 2009. **8**(2): p. 165-174.
18. Salomir, R., B.D. de Senneville, and C.T. Moonen, *A fast calculation method for magnetic field inhomogeneity due to an arbitrary distribution of bulk susceptibility*. 2003. **19B**(1): p. 26-34.

Chapter 6

Brain Deep Medullary Veins on 7T MRI in Dutch-Type Hereditary Cerebral Amyloid

T.W. van Harten, A. Heijmans, S. van Rooden, M.J.H. Wermer, M.J.P. van Osch, H.J. Kuijf, S.J. van Veluw, S.M. Greenberg, M.A. van Buchem, J. van der Grond, M.A.A. van Walderveen

This chapter has been published J Alzheimers Dis. 2022. doi: 10.3233/JAD-220354

ABSTRACT

Background Deep medullary vein (DMV) changes occur in cerebral small vessel diseases (SVD) and in Alzheimer's disease. Cerebral amyloid angiopathy (CAA) is a common SVD that has a high co-morbidity with Alzheimer's disease. So far, DMVs have not been evaluated in CAA.

Objective To evaluate DMVs in Dutch-type hereditary CAA (D-CAA) mutation carriers and controls, in relation to MRI markers associated with D-CAA.

Methods Quantitative DMV parameters length, tortuosity, inhomogeneity, and density were quantified on 7 Tesla 3D susceptibility weighted MRI in pre-symptomatic D-CAA mutation carriers (n=8), symptomatic D-CAA carriers (n=8) and controls (n=25). Hemorrhagic MRI markers (cerebral microbleeds, intracerebral hemorrhages, cortical superficial siderosis, convexity subarachnoid hemorrhage), non-hemorrhagic MRI markers (white matter hyperintensities, enlarged perivascular spaces, lacunar infarcts, cortical microinfarcts), cortical grey matter perfusion and diffusion tensor imaging (DTI) parameters were assessed in D-CAA mutation carriers. Univariate general linear analysis was used to determine associations between DMV parameters and MRI markers.

Results Quantitative DMV parameters length, tortuosity, inhomogeneity, and density did not differ between pre-symptomatic D-CAA mutation carriers, symptomatic D-CAA mutation carriers, and controls. No associations were found between DMV parameters and MRI markers associated with D-CAA.

Conclusion This study indicates that vascular amyloid- β deposition does not affect DMV parameters. In patients with CAA, DMVs do not seem to play a role in the pathogenesis of MRI markers associated with CAA.

1. Introduction

Deep medullary veins (DMV) originate 1-2 cm below the cortical gray matter, pass through deep medullary white matter, and drain into subependymal veins of the lateral ventricles. DMVs drain venous blood from the deep and periventricular white matter. At autopsy, periventricular venous collagenosis is associated with the presence of periventricular leukoaraiosis in patients of 60 years and older [1] and in patients with Alzheimer's disease (AD) [2].

Radiological studies reported changes of DMVs on susceptibility weighted MRI in patients with cerebral small vessel diseases (SVD), including Cerebral autosomal dominant arteriopathy with subcortical infarcts and leukoencephalopathy [3, 4], with an inverse relationship between number and/or integrity of DMVs and SVD markers on MRI, in particular with white matter hyperintensities (WMHs) [4-6]. Age also effects DMVs, with decreased number of DMVs associating with the increase of age.[7] Further, in aging an association was shown between venous pathological changes and leukoaraiosis [8], and increased DMV tortuosity in patients with early AD and mild cognitive impairment [9]. Collagenosis of DMVs is assumed to be the underlying pathophysiology of leukoaraiosis in cerebral SVDs[8]. In patients with AD, it is hypothesized that DMV abnormalities are associated with increased pulsatility of venous blood flow and possibly a remote effect of arterial A β deposition in the cortex on the veins of the white matter in patients with concomitant cerebral amyloid angiopathy (CAA)[9].

CAA is one of the most common forms of cerebral SVD and is highly prevalent in the elderly population [10], but also commonly (> 80%) found as co-morbidity in patients with AD [11]. CAA is characterized by deposition of amyloid- β (A β) proteins in the walls of small leptomeningeal and cortical arterioles. Further, A β proteins also aggregate to some extent in leptomeningeal and cortical venules of the brain [12]. As such, the pathophysiology of CAA clearly differs from that of

other – non-amyloid - SVDs. Currently, the effect of vascular A β deposition on deep venous structures has not been evaluated in patients with CAA and the relationship between DMV changes and SVD markers on MRI – especially WMH - in this population is unknown. Moreover, knowledge on occurrence of DMV changes in patients with CAA might provide insight into the underlying pathophysiology of the observed DMV changes in patients with AD, considering the high co-morbidity of CAA and AD.

Dutch-type CAA (D-CAA, also known as Hereditary Cerebral Hemorrhages with Amyloidosis-Dutch type (HCHWA-D)) is an autosomal dominant hereditary form of CAA with similar chemical composition and underlying pathology of A β deposits to that of sporadic CAA [13]. Symptomatology is also similar to sporadic CAA, both are characterized by intracerebral hemorrhages and cognitive impairment, but the onset of symptoms in D-CAA occurs at a relatively young age (50-60 years). Because vascular risk factors are in general not often present at this age, D-CAA can be considered a ‘pure’ model of CAA. Further, concomitant AD is also unlikely to occur in this age category. D-CAA, therefore, provides a unique opportunity to evaluate if vascular A β accumulation results in changes in DMVs.

The objective of this study was to evaluate if DMV changes occur in D-CAA mutation carriers, as compared to controls. The second aim was to evaluate whether these DMV changes correlate with other MRI markers associated with D-CAA.

2. Methods

Study population

D-CAA mutation carriers and age-matched controls who participated in the Early Diagnosis of Amyloid angiopathy Network (EDAN) study [14] were included. The aim of the EDAN study was - amongst others - to identify early markers of D-CAA on 3T and 7T MRI and included adult patients who had been diagnosed with D-CAA via genetic testing, divided into either pre-symptomatic or symptomatic D-CAA mutation carriers. Subjects were considered symptomatic when they had experienced signs of the disease reported to a general practitioner [14]. Data on age, sex and mutation status were available for all. The study was carried out in accordance with the principals of the Declaration of Helsinki and approved by the local Institutional Review Board. Written informed consent was obtained from all participants.

MRI

All subjects underwent both 7T and 3T MRI (Philips Healthcare, Best, The Netherlands). The protocol for the EDAN study consisted of a variety of sequences at both field strengths to enable the analysis of hemorrhagic and non-hemorrhagic MRI markers of CAA; for a detailed description of the sequence parameters we refer to the EDAN protocol [14]. Hemorrhagic MRI markers (cerebral microbleeds, intracerebral hemorrhages, cortical superficial siderosis, and convexity subarachnoid hemorrhages) were assessed on 7T T2*-weighted sequences. Cortical microinfarcts were scored as described previously [15]. Non-hemorrhagic MRI markers were assessed on 3T (WMHs, dilatation of perivascular spaces in basal ganglia and centrum semiovale, lacunar infarcts on fluid-attenuated inversion recovery (FLAIR), T1-weighted and T2-weighted images). Cortical grey matter regional cerebral blood flow (rCBF) was measured on 3T MRI using pseudo-continuous arterial spin labelling[16] and diffusion tensor images were acquired on

3T MRI along 32 noncollinear directions with a b-value of 1000 s/mm²[17]. We assessed DMVs on 7T MRI dual echo 3D flow-compensated T2*-weighted gradient echo scan (TR 19.6/first TE 3 ms/second TE 15 ms, flip angle 20, FOV of 200 x 180 x 100 mm, 512 reconstructed matrix size, resulting in a voxel size of 0.39 x 0.45 x 0.30 mm reconstructed in-plane to 0.39 mm).

DMV analysis

A semi-automated method based on a previous protocol described by Kuijf et al. [18] was used for the detection and quantification of DMVs. In short, grey matter, white matter, and cerebrospinal fluid (CSF) were segmented using the 7T T1-weighted MRI of each subject. Subsequently, the ventricle segmentation was transformed to the 7T 3D flow-compensated T2*-weighted images and corrected for inhomogeneities by applying a bias field correction prior to automatic detection of DMVs. Expansion of the ventricular surface was set at a distance of 5 to 5.5 mm from the ventricles to detect DMVs that intersect with this curved 3D surface (Figure 2). To assess DMVs that drain the white matter of the centrum semiovale, we selected slices cranial from the level of the basal ganglia and splenium of the corpus callosum. Detection of DMVs was performed by applying an automated detection algorithm, after which detected veins were evaluated individually to exclude false positives. Number of DMVs were determined per patient and the overall mean value for the number of veins per subject group (pre-symptomatic and symptomatic D-CAA mutation carriers, and controls) was obtained. Finally, a bidirectional tubular tracking was applied and values derived from the tracking procedure were used to produce the following quantitative DMV parameters: 1) the total length of each vein, to calculate the mean venous length per subject; 2) venous tortuosity, determined by taking the total length of the vein divided by the distance between start and finish of the vein in a straight line within 3D space (i.e., the Euclidean distance), to calculate a mean value for venous tortuosity per subject; 3) venous inhomogeneity, by calculating the derivative of

intensity changes of veins. In more detail, occurrence and frequency of signal intensity transitions within tracked veins was counted and expressed as absolute venous inhomogeneity; a higher number of intensity transitions within a tracked vein will translate into a higher absolute venous inhomogeneity and vice versa; and lastly 4) venous density, by dividing the number of veins by the volume in which they are detected. When presence of an intracerebral hemorrhage in a single hemisphere precluded evaluation of DMVs, this hemisphere was excluded from further analysis and DMVs were only evaluated in the contralateral hemisphere. If this was the case for both hemispheres, or in case of severe motion artefacts, the individual was excluded from further analysis.

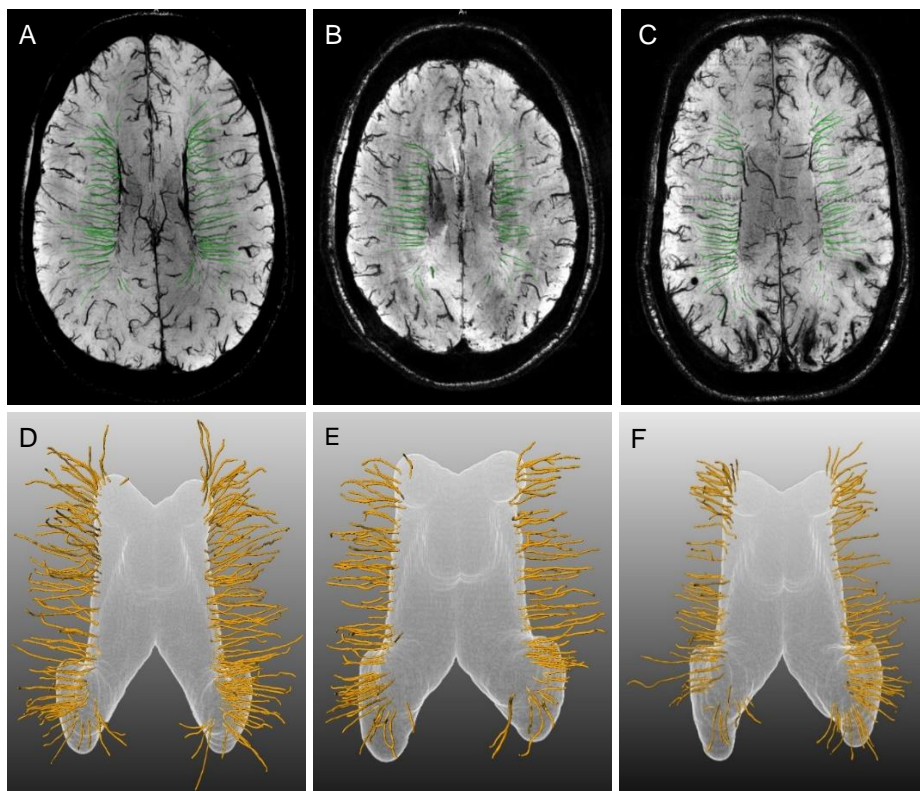


Figure 2: Examples of transversal 6 mm thick maximum intensity projections of 7T T2*-weighted sequence with tracked veins displayed in green (A-C) and corresponding 3D-rendering of the deep medullary veins (DMVs) with the expanded surface shown in white and the reconstructed veins in yellow (D-F). Although mean venous length of the 56-year-old control subject (A, D) was higher as compared to the 51-year-old pre-symptomatic (B, E) and 55-year-old symptomatic (C, F) D-CAA mutation carrier (18.4 mm, 16.1 mm and 16.3 mm, resp), this difference was not statistically significant between groups. Also, mean venous density was higher in this control subject (0.32) as compared to the pre-symptomatic (0.24) and symptomatic (0.25) D-CAA mutation carriers, although this difference was also not significant between groups.

DMV parameters were related to presence and number of lobar cerebral microbleeds, intracerebral hemorrhages, cortical microinfarcts, convexity subarachnoid hemorrhages and presence of cortical superficial siderosis on 7T T2*-weighted sequences. DMV parameters were related to volume of WMHs and dilated perivascular spaces, according to previously described methods [19], and number of lacunar infarcts on 3T MRI. In addition, DMV parameters were related to perfusion of supratentorial cortical grey matter volume outside areas of

intracerebral hemorrhages to make sure we measured grey matter [16] and to diffusion tensor imaging parameters fractional anisotropy (FA), mean diffusivity (MD), axial diffusivity (AD), and radial diffusivity (RD)[17]. 3D T1-weighted images were co-registered with a standard brain from which a ventricle segmentation was selected. The transformed ventricle segmentation was subsequently used to determine ventricular volume for each patient. Total intracranial volume (ICV) and total brain volume (TBV) were also obtained from 3T T1 weighted images.

Statistical analysis

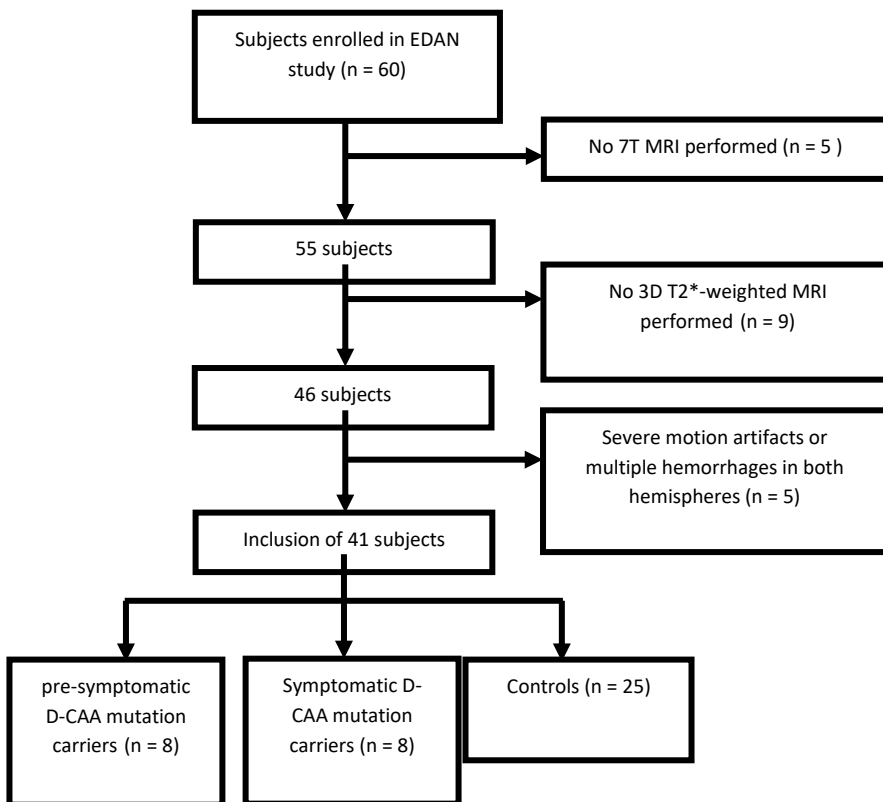
Differences in group means between D-CAA mutation carriers and control subjects were tested with the independent t-test. A univariate general linear model was used to adjust for sex, age, and TBV as percentage of intracranial volume (TBV% ICV). The following between group comparisons were tested: 1) all D-CAA mutation carriers versus controls; 2) pre-symptomatic D-CAA mutation carriers versus controls; and 3) symptomatic D-CAA mutation carriers versus controls. Mean values of venous length, venous tortuosity, absolute venous homogeneity, and venous density were entered as dependent variable.

To assess the correlation between DMV parameters and SVD markers, univariate general linear modeling was used. Dependent variables were the same as mentioned previously, SVD MRI-markers were entered as either a fixed variable or covariate depending on the data. The correlation assessments were done within D-CAA mutation carriers and adjusted for age, sex, and TBV% ICV. To adjust for multiple testing, we divided an α -value of 0.05 by the number of tests performed and considered a p-value <0.001 to be statistically significant. All statistical analysis were performed within SPSS (version 26.0).

3. Results

Of the 60 persons initially included in the EDAN study, 41 were analyzed - see flowchart in figure 1; 16 D-CAA mutation carriers (8 pre-symptomatic [88% female]; mean age: 31.5 years, range 20-51, and 8 symptomatic [63% female]; mean age: 54.9 years, range 45-63), and 25 controls (60% female; mean age: 45.6 years, range 30-67). In 4 symptomatic D-CAA patients, one hemisphere was excluded from analysis, because the presence of intracerebral hemorrhages precluded DMV detection; in these 4 patients only the contralateral hemisphere was used for DMV analysis.

Figure 1. Flowchart of inclusion of patients



DMV parameters between D-CAA mutation carriers and controls

The mean values of DMV parameters for D-CAA mutation carriers and controls are shown in Table 1. Mean venous length did not differ between controls (14.7 mm, 95% confidence interval (CI) 14.3 – 16.1), pre-symptomatic D-CAA mutation carriers (14.3 mm, 95% confidence interval (CI) 12.6-16.1) and symptomatic D-CAA mutation carriers (13.4 mm, 95% CI 11.6 – 15.2). Also, mean tortuosity (controls 1.09, 95% CI 1.08 – 1.10; pre-symptomatic D-CAA mutation carriers 1.09, 95% CI 1.07 – 1.12; symptomatic D-CAA mutation carriers 1.09, 95% CI 1.07 – 1.10), mean absolute inhomogeneity (controls 30.5, 95% CI 28.4 – 32.5; pre-symptomatic D-CAA mutation carriers 26.6, 95% CI 23.7 – 29.5; symptomatic D-CAA mutation carriers 29.4, 95% CI 25.6 – 33.3) and mean venous density (controls 0.23 veins/cm³, 95% CI 0.20 – 0.26; pre-symptomatic D-CAA mutation carriers 0.21 veins/cm³, 95% CI 0.18 – 0.24; symptomatic D-CAA mutation carriers 0.23 veins/cm², 95% CI 0.18 – 0.28) was not different between groups. No association between age and any DMV parameter was found in any of the 3 groups.

Table 1. Demographics and DMV parameters for D-CAA mutation carriers and controls. Mean values \pm standard deviations are given, group means were compared. For sex the number and % within each group are given. Significant Chi-Square test used to report *p* values for sex. Reported *p* values for DMV parameters are obtained by using a univariate general linear model. DMV = deep medullary vein. D-CAA = Dutch-type cerebral amyloid angiopathy.

		D-CAA mutation carriers (n=16)						
		Controls (n=25)	All	p value vs controls	Pre- symptomatic (n=8)	p value vs controls	Symptomatic (n=8)	p value vs controls
Age (y)		45.6 ± 11.8	43.2 ± 15.7	0.13	31.5 ± 13.2	0.15	54.9 ± 6.3	0.02
	Male, n (%)		4					
Sex	Female, n (%)	10 (40)	(25) 12 (75)		1 (1.5)		3 (37.5)	
		15 (60)			7 (87.5)		5 (62.5)	
DMV parameters								
Length (mm)		14.7 ± 1.9	13.9 ± 2.1 1.09	0.52	14.3 ± 2.1	0.43	13.4 ± 2.1	0.52
				0.86				
Tortuosity		1.09 ± 0.02	± 0.03		1.09 ± 0.03		1.09 ± 0.02	
Absolute inhomogeneity		30.5 ± 4.9	28.0 ± 4.2 0.22	0.75	26.6 ± 3.5	0.95	29.4 ± 4.6	0.80
				0.61				
Density (veins/cm³)		0.23 ± 0.07	± 0.05		0.21 ± 0.04		0.23 ± 0.62	

Relation between quantitative DMV parameters and MRI markers associated with D-CAA

The mean values of MRI markers associated with D-CAA in D-CAA mutation carriers and controls are shown in Table 2. In D-CAA mutation carriers, venous parameters did not correlate with any non-hemorrhagic or hemorrhagic SVD markers on MRI; further, no association was present with DTI parameters (FA, MD, AD, RD) or grey matter perfusion values.

Table 2. Mean values \pm standard deviations are given; n are the participants scoring >1 or >2 for the given parameters. WMH, white matter hyperintensities, natural logarithm taken from original values for normal distribution; ICH, intracerebral hemorrhage; cSAH, convexity subarachnoid hemorrhage; cSS, cortical superficial siderosis; PVS, perivascular spaces; GM, grey matter; FA, fractional anisotropy; MD, mean diffusivity; AD, axial diffusivity; RD, radial diffusivity; ICV, intracranial volume; TBV, total brain volume. Total ICV values were scaled to a standardized brain, the scaling factor was used to calculate the values. Small vessel disease markers on MRI in D-CAA mutation carriers and controls

	D-CAA mutation carriers (n=16)			
	Controls (n=25)	All	Pre- symptomatic (n=8)	Symptomatic (n=8)
Microbleeds >2 , n	-	9	1	8
ICH >1 , n	-	8	-	8
cSAH >1 , n	-	5	1	4
Presence cSS, n	-	7	-	7
Cortical microinfarct >1 , n	1	8	0	8
WMH volume, cm ³	2.90 \pm 2.85	17.12 \pm 20.94	2.53 \pm 1.13	33.80 \pm 20.32
Dilated PVS volume, cm ³	0.02 \pm 0.02	0.05 \pm 0.44	0.02 \pm 0.03	0.08 \pm 0.04
Lacunar infarcts >1 , n	7	2	2	-
GM perfusion, mL/min/100 g brain tissue	60.6 \pm 13.2	59.7 \pm 12.4	65.1 \pm 5.6	54.4 \pm 15.2
FA	0.43 \pm 0.02	0.40 \pm 0.04	0.43 \pm 0.01	0.37 \pm 0.04
MD, $\times 10^{-4}$, 1000 s/mm ²	7.37 \pm 0.22	8.03 \pm 1.01	7.34 \pm 0.16	8.71 \pm 1.04
AD, $\times 10^{-3}$, 1000 s/mm ²	1.11 \pm 0.02	1.16 \pm 0.09	1.10 \pm 0.02	1.22 \pm 0.02
RD, $\times 10^{-4}$, 1000 s/mm ²	8.80 \pm 0.21	9.44 \pm 0.97	8.78 \pm 0.15	10.10 \pm 1.0
Normalized GM, cm ³	658 \pm 58	661 \pm 76	715 \pm 55	600 \pm 42
Total ICV, cm ³	1543 \pm 183	1554 \pm 220	1477 \pm 236	1631 \pm 185
Ventricular volume, cm ³	32 \pm 9	38 \pm 16	28 \pm 9	48 \pm 16
Ventricular volume %ICV	2.0 \pm 0.5	2.4 \pm 0.9	1.9 \pm 0.4	2.9 \pm 0.9
TBV %ICV	77 \pm 6	77 \pm 10	83 \pm 12	72 \pm 5

4. Discussion

We did not observe a difference in DMV length, tortuosity, homogeneity, and density between D-CAA mutation carriers and controls. Also, no differences in DMV parameters were found between pre-symptomatic and symptomatic D-CAA mutation carriers. Secondly, in D-CAA mutation carriers no association was found between DMV parameters and MRI markers associated with D-CAA.

Several studies have suggested that arterial and/or venular A β depositions affect the cerebral vasculature in AD patients, including DMVs [9, 20]. Arterial A β deposition has been shown to stiffen vessels and thereby increases pulsatility, causing physical stress on venules. DMVs are suggested to be increasingly susceptible to stress because of their lower baseline resistance. Venular A β deposition has been suggested to impair A β clearance, similar to arterial A β deposition, and is suggested to be an integral part of AD pathogenesis [20]. Although we acknowledge that only a small number of individuals were included in our study, our results did not indicate a clear association between MRI markers of CAA pathology in the cortex and venous pathology in the white matter and this study therefore does not support the hypothesis that concomitant CAA pathology might be a contributing factor to DMV changes in patients with AD.

In contrast to findings in patients with non-amyloid cerebral SVD [3-6, 21], we did not find an association between DMV parameters and non-hemorrhagic and hemorrhagic markers on MRI in D-CAA mutation carriers; more specifically, a relation with WMH volume was not present. Our results suggest that in patients with CAA, a remote CAA-induced change of DMVs do not play a role in the pathogenesis of WMH or other non-hemorrhagic or hemorrhagic markers on MRI. However, considering the typical posterior predominance of WMH in patients with CAA together with the possible relationship between WMH and DMV parameters [4-6], the relationship between posterior WMH and DMV parameters could be

addressed further in patients with CAA in future studies. No association was present with DTI parameters or cortical grey matter perfusion values. DMV inhomogeneity has been associated with FA of DMVs drainage area in cerebral SVD patients [22] and number of DMVs with FA and MD of the white matter in a population-based cohort [23]. Our results, however, do not indicate that DMVs play a role in white matter microstructural integrity loss in patients with CAA. A major limitation of this study is the small sample size. This is inevitably coupled to the relatively small number of D-CAA mutation carriers living in the Netherlands and subsequently only a small number of individuals was included in the original EDAN study. In addition, we had to exclude 5 participants from analysis because of severe motion artifacts and/or presence of multiple large intracerebral hemorrhages, resulting in a further decrease of the sample size.

Bouvy and coworkers [9] found in only a slightly larger group size a significant difference in venous tortuosity in the early AD population as compared to controls, whereas in our study venous tortuosity was similar in all our 3 groups. In the study of Bouvy and coworkers, difference in SVD pathology was more than a factor 3 smaller as concluded from the smaller difference in WMH volumes between groups. We therefore assume that, although the number of participants was small, we would have found a significant difference when venous tortuosity would be an important factor in D-CAA pathology.

A strength of our study is that we used a validated technique for the automated detection and quantification of DMVs on T2*-weighted 7T MRI [18]. Although our sample size is small, the study is performed in a unique population that is considered a 'pure' model for sporadic CAA.

In conclusion, this study showed that quantitative DMV parameters did not differ between D-CAA mutation carriers and controls. In patients with CAA, DMVs likely do not play a role in the pathogenesis of SVD MRI markers associated with D-CAA.

Acknowledgements (including sources of support)

This study was supported by the National Institutes of Health grant R01 NS070834, by the Dutch Heart Foundation and the Netherlands Organization for Scientific Research (NWO), as part of their joint strategic research program: "Earlier recognition of cardiovascular diseases"; this project is partially financed by the PPP Allowance made available by Top Sector Life Sciences & Health to the Dutch Heart foundation to stimulate public-private partnerships, and by a Clinical Established Investigator grant of the Netherlands Heart Foundation 2016T86 Dr Wermer

Conflict of interest/disclosure statement

The authors have no conflict of interest to report

References

1. Moody DM, Brown WR, Challa VR, Anderson RL (1995) Periventricular Venous Collagenosis - Association with Leukoaraiosis. *Radiology* **194**, 469-476.
2. Keith J, Gao FQ, Noor R, Kiss A, Balasubramaniam G, Au K, Rogaeva E, Masellis M, Black SE (2017) Collagenosis of the Deep Medullary Veins: An Underrecognized Pathologic Correlate of White Matter Hyperintensities and Periventricular Infarction? *J Neuropathol Exp Neurol* **76**, 299-312.
3. De Guio F, Vignaud A, Ropele S, Duering M, Duchesnay E, Chabriat H, Jouvent E (2014) Loss of Venous Integrity in Cerebral Small Vessel Disease A 7-T MRI Study in Cerebral Autosomal-Dominant Arteriopathy With Subcortical Infarcts and Leukoencephalopathy (CADASIL). *Stroke* **45**, 2124-2126.
4. Chen XD, Wei L, Wang JH, Shan YL, Cai W, Men XJ, Liu SX, Kang Z, Lu ZQ, Mok VCT, Wu AM (2020) Decreased visible deep medullary veins is a novel imaging marker for cerebral small vessel disease. *Neural Sci* **41**, 1497-1506.
5. Xu ZH, Li FF, Wang B, Xing DX, Pei YS, Yang BQ, Duan Y (2020) New Insights in Addressing Cerebral Small Vessel Disease: Association With the Deep Medullary Veins. *Front Aging Neurosci* **12**, 597799.
6. Zhang RT, Zhou Y, Yan SQ, Zhong GL, Liu C, Jiaerken YF, Song RR, Yu XF, Zhang MM, Lou M (2017) A Brain Region-Based Deep Medullary Veins Visual Score on Susceptibility Weighted Imaging. *Front Aging Neurosci* **9**, 269.
7. Ao DH, Zhang DD, Zhai FF, Zhang JT, Han F, Li ML, Ni J, Yao M, Zhang SY, Cui LY, Jin ZY, Zhou LX, Zhu YC (2021) Brain deep medullary veins on 3-T MRI in a population-based cohort. *J Cereb Blood Flow Metab* **41**, 561-568.
8. Nan D, Cheng YY, Feng LS, Zhao MM, Ma D, Feng JC (2019) Potential Mechanism of Venous System for Leukoaraiosis: From post-mortem to in vivo Research. *Neurodegener Dis* **19**, 101-108.
9. Bouvy WH, Kuijff HJ, Zwanenburg JJM, Koek HL, Kappelle LJ, Luijten PR, Ikram MK, Biessels GJ, Cognitive UV (2017) Abnormalities of Cerebral Deep Medullary Veins on 7 Tesla MRI in Amnesic Mild Cognitive Impairment and Early Alzheimer's Disease: A Pilot Study. *J Alzheimers Dis* **57**, 705-710.
10. Jakel L, De Kort AM, Klijn CJM, Schreuder FHBM, Verbeek MM (2022) Prevalence of cerebral amyloid angiopathy: A systematic review and meta-analysis. *Alzheimers Dement* **18**, 10-28.

11. Attems J, Lauda F, Jellinger KA (2008) Unexpectedly low prevalence of intracerebral hemorrhages in sporadic cerebral amyloid angiopathy - An autopsy study. *J Neurol* **255**, 70-76.
12. Thal DR, Ghebremedhin E, Rub U, Yamaguchi H, Del Tredici K, Braak H (2002) Two types of sporadic cerebral amyloid angiopathy. *J Neuropath Exp Neurol* **61**, 282-293.
13. Zhang-Nunes SX, Maat-Schieman MLC, van Duinen SG, Roos RAC, Frosch MP, Greenberg SM (2006) The cerebral beta-amyloid angiopathies: Hereditary and sporadic. *Brain Pathol* **16**, 30-39.
14. van Rooden S, van Opstal AM, Labadie G, Terwindt GM, Wermer MJH, Webb AG, Middelkoop HAM, Greenberg SM, van der Grond J, van Buchem MA (2016) Early Magnetic Resonance Imaging and Cognitive Markers of Hereditary Cerebral Amyloid Angiopathy. *Stroke* **47**, 3041-3044.
15. van Veluw SJ, Biessels GJ, Luijten PR, Zwanenburg JJM (2015) Assessing Cortical Cerebral Microinfarcts on High Resolution MR Images. *J Vis Exp* **105**, 1-8.
16. van Opstal AM, van Rooden S, van Harten T, Ghariq E, Labadie G, Fotiadis P, Gurol ME, Terwindt GM, Wermer MJH, van Buchem MA, Greenberg SM, van der Grond J (2017) Cerebrovascular function in presymptomatic and symptomatic individuals with hereditary cerebral amyloid angiopathy: a case-control study. *Lancet Neurol* **16**, 115-122.
17. Schouten TM, de Vos F, van Rooden S, Bouts MJRJ, van Opstal AM, Feis RA, Terwindt GM, Wermer MJH, van Buchem MA, Greenberg SM, de Rooij M, Rombouts SARB, van der Grond J (2019) Multiple Approaches to Diffusion Magnetic Resonance Imaging in Hereditary Cerebral Amyloid Angiopathy Mutation Carriers. *J Am Heart Assoc* **8**, e011288. DOI: 011210.011161/JAHA.011118.011288.
18. Kuijff HJ, Bouvy WH, Zwanenburg JJM, Schultz TBR, Viergever MA, Vincken KL, Biessels GJ (2016) Quantification of deep medullary veins at 7 T brain MRI. *Eur Radiol* **26**, 3412-3418.
19. Martinez-Ramirez S, van Rooden S, Charidimou A, van Opstal AM, Wermer M, Gurol ME, Terwindt G, van der Grond J, Greenberg SM, van Buchem M, Viswanathan A (2018) Perivascular Spaces Volume in Sporadic and Hereditary (Dutch-Type) Cerebral Amyloid Angiopathy. *Stroke* **49**, 1913-1919.
20. Morrone CD, Bishay J, McLaurin J (2020) Potential Role of Venular Amyloid in Alzheimer's Disease Pathogenesis. *Int J Mol Sci* **21**, 1985.
21. Zhou Y, Li QQ, Zhang RT, Zhang WH, Yan SQ, Xu JJ, Wang SY, Zhang MM, Lou M (2020) Role of deep medullary veins in pathogenesis of lacunes: Longitudinal observations from the CIRCLE study. *J Cereb Blood Flow Metab* **40**, 1797-1805.
22. Zhang RT, Huang PY, Jiaerken Y, Wang SY, Hong H, Luo X, Xu XP, Yu XF, Li KC, Zeng QZ, Wu X, Lou M, Zhang MM (2021) Venous disruption affects white matter integrity through increased interstitial fluid in cerebral small vessel disease. *J Cereb Blood Flow Metab* **41**, 157-165.
23. Liu ZY, Zhai FF, Ao DH, Han F, Li ML, Zhou LX, Ni J, Yao M, Zhang SY, Cui LY, Jin ZY, Zhu YC (2021) Deep medullary veins are associated with widespread brain structural abnormalities. *J Cereb Blood Flow Metab* **41**, 1-10.

Chapter 7

Summary and discussion

Summary

The overarching theme throughout this thesis is the exploration of new and the improvement of existing methods of measuring neurovascular pathology using MRI techniques and postprocessing. As cerebrovascular afflictions are not located at a single location, these methods are applied throughout the cerebrovascular tree. This thesis starts with the large (macro) arteries (**chapter 2**), to the function of (micro) arteries (**chapters 3 and 4**), to remnants of hemorrhages in brain tissue (**chapter 5**), to finally the venous compartment (**chapter 6**), and takes into account both structure and function of selected parts of the cerebrovascular tree.

We investigated large artery cerebrovascular pathology in combination with a novel MRI technique and advanced postprocessing methods, to extract additional information from pCASL scans. Other research did already prove that additional functional information can be inferred from ASL scans, e.g. resting state networks [1]. Moreover, local physiological- and physical conditions can influence labeling efficiency in pCASL [2-4]. Combining these two facts could hypothetically indicate that one may infer flow territory information from signal fluctuations in the resulting ASL scan due to vessel specific fluctuations in off-resonance effects in the labeling plane. In **chapter 2** we showed the degree of fluctuations that are needed to obtain this information on an individual subject level. This was achieved by an additional gradient in the labeling plane, driving a pattern of signal fluctuations in healthy participants. When applying additional vessel-encoded gradients these methods are able to distinguish flow territories from one another, but this would result in approximately 8.5% lower perfusion signal and thus also a reduction in SNR of the same order of magnitude. We also tested these methods on standard pCASL scans of patients with a severe (>70%) internal carotid stenosis, to see if fluctuations occurring *in vivo* would be sufficient to derive such flow territory information on a single subject level. We were unable to report fluctuations of sufficient magnitude to infer this information from a standard pCASL scan.

Moving from the large arteries to the function of the microvasculature, we looked at two populations of D-CAA patients in **chapters 3 and 4**. Vascular reactivity upon a visual stimulus is increasingly recognized as an important marker of CAA. We found in the literature that these outcome measures are determined in a number of different ways, which may limit the possibility to compare results between sites and studies. In **chapter 3**, the most common ways of post-processing were investigated and tested both on their efficacy as well as reproducibility and we commented on the possibility of introducing instances that could be considered statistically incorrect. We were able to illustrate how this may affect the outcome measures of patient studies. These results are especially relevant due to the high degree of heterogeneity of disease burden in our study sample. Furthermore, we looked at the reproducibility of each of these methods in a test-retest setting. We showed that in healthy individuals the three methods selected distinct sets of voxels, which produced similar outcome measures. However, in D-CAA cases with (severe) pathology, one of the methods showed higher reactivity measures and voxels not restricted to the expected area of activation. This is due to circular analysis or ‘double dipping’. Our data showed that the effects of this bias are especially evident in patients with a more severely disrupted hemodynamic response, and we recommended using the other methods in the future.

A novel high temporal resolution fMRI scan at 7T MRI was used in **chapter 4** to further investigate the hemodynamic changes in a cohort of early stage female D-CAA mutation carriers and healthy participants. To better characterize the hemodynamic response function a short stimulus was applied (3s) in combination with a long rest period (45s), to allow the local vasculature to return to a baseline state after each burst of activation. The results show that especially the main positive BOLD-response is affected in D-CAA, while the post-stimulus undershoot was much less affected. In a previous 3T study of D-CAA patients in our center, there were a number of symptomatic patients that showed little to no response to the visual stimulus [5]. One interesting finding of the study described in this

chapter was that for some of these D-CAA mutation carriers who showed a “flat-line” response on both 3T and 7T with the traditional paradigm and BOLD sequence, we were able to observe a hemodynamic response to the visual stimulus with the combination of a short stimulus and high temporal resolution BOLD scan.

An important imaging finding in CAA and increasingly recognized risk factor for future ICH is cortical superficial siderosis (cSS). This marker was first added to the Boston criteria in the modified version (also known as version 1.5) [6]. The presence and/or progression of cSS has traditionally been described using categorical scales. This inevitably leads to loss of information on a patient based level due to ceiling effects, as well as a further loss of information on a group based level due to large heterogeneity in the highest category. In **chapter 5** this categorical scale has been turned into a quantitative one by segmentation of cSS on susceptibility weighted MR images and subsequently quantifying the volume in a novel, semi-automatic manner. By using this novel way of segmenting and subsequently quantifying siderosis, we are able to distinguish heterogeneity between patients in the highest category, and -within patients – to monitor disease progression in even the most severe cases without suffering from ceiling effects. The highest category showed large heterogeneity (between 2666mm³ and 16521mm³) and we showed progression in three out of five sCAA patients in a one year follow-up, two of whom already were in the highest category.

Changes in deep medullary veins (DMV) have been reported in several cSVD [7-9]. CAA is one of the most common forms of cSVD and a common comorbidity of Alzheimer’s disease [10, 11]. In patients with Alzheimer’s it has been shown that the DMV morphology is changed compared to healthy participants [12]. In **chapter 6**, seed points for DMV tracking were generated on susceptibility weighted images based on the criteria of a tubular shape of hypointense structures intersecting with the inflated surface of the lateral ventricles. DMV segmentation was then

performed by a bidirectional tubular tracking algorithm. Using this method we showed that DMVs were not different in number, tortuosity or absolute homogeneity between healthy participants, presymptomatic and symptomatic D-CAA mutation carriers, nor did we find an association between MRI markers related to CAA and venous morphology parameters. This indicates that in D-CAA the deposition of amyloid does not affect DMV parameters, and that DMVs do not seem to be implicated in the pathogenesis of MRI markers associated with CAA.

Discussion

MRI markers of CAA: considerations for diagnosis, disease monitoring and clinical trials.

Throughout the vascular tree, we aimed to develop new- and improve existing methods of measuring neurovascular pathology using MRI techniques and postprocessing. These methods were mainly tested in patients with CAA, an untreatable disease that leads to cognitive decline, ICH and ultimately death. In vivo diagnosis of CAA in clinical practice is done using the Boston criteria; these criteria are still evolving in order to improve sensitivity and specificity [6, 13, 14]. The latest revision of the Boston criteria includes – apart from age, clinical symptoms and hemorrhagic markers (ICH, CMB and cSS) - also non-hemorrhagic markers (severe visible perivascular spaces and multisport pattern WMH) and shows high specificity over the range of clinical presentations with increased sensitivity for non-ICH presentations [14]. Updates on imaging diagnoses and imaging standards in cSVDs show that markers for cerebrovascular disease are still an active part of research and underline the importance of the type of research described in this thesis [14-16]. Improved methods and techniques facilitates a positive feedback loop in diagnosis sensitivity and specificity, detection of pathology, improved understanding and monitoring of disease progression, which in turn can lead to new technological improvements. This is especially the case for research on “pure” hereditary variants of CAA, such as D-CAA, which due to severity and early age of onset is inherently less hampered by comorbidities and aging, allowing the development of very specific markers.

Some markers that are included in the Boston criteria, can also play an important role in making optimal decisions on disease management. cSS, for example, is a major predictor for future ICH and its presence may warrant a change in treatment and prognosis [17, 18]. Progression of cSS is suggested to be of importance in the

assessment of CAA severity [19, 20], and moving from a categorical scale to a more quantitative method as described in **chapter 5** will be of interest for future clinical research. Further development of this technique may yield more reliable results. For example, by moving from a volumetric measurement to a measure like surface area of the cortex affected, one may be less affected by sequence parameters and field strength related artifacts. However, this will lead to an increase in processing time and the chance of errors in segmentation of the cortical surface, especially in a population with many lobar bleeds, such as a cohort of CAA patients.

Currently, several options for pharmaceutical interventions are studied to provide a much needed treatment solution for CAA, although our still incomplete understanding of disease pathogenesis and progression, as well as the heterogeneity of symptoms expressed by patients make this a difficult endeavor [20-22]. Since hopes are now high that a treatment trial could commence soon, powerful outcome measures must be established with some urgency. CAA progression could be characterized by many outcome measures, e.g. amyloid deposition as measured by amyloid-PET, vascular function, (non-)hemorrhagic brain lesions, CSF-markers, and clinical presentation. Ideally, one would have markers that can detect CAA as early in the disease process as possible, while being easily measured and monitored over time, in combination with being reproducible, reliable and sensitive to a response to treatment. By developing new and improving existing methods to quantify markers, differences between the intervention and control arms can be discerned earlier and more robustly, and with fewer participants in clinical trials. One example of such a potential marker is described in **chapter 4**, where vascular reactivity is measured using high temporal resolution BOLD. This measurement may prove to be an early and sensitive marker for disease progression, and is more stable and clear than the traditional way of measuring vascular reactivity. However, this measurement is performed on 7T MRI, which may impede trials, as scanners with an ultrahigh field strength are of limited availability.

While some of the markers described in this thesis are very relevant for CAA, they are not incorporated in the Boston criteria yet. By adding new or more precisely measured markers to the criteria one could increase the sensitivity and specificity of the diagnosis, ideally to a point that a definite diagnosis could be made in vivo without the need of an invasive biopsy. Vascular reactivity parameters derived from BOLD fMRI are very robust markers on the group level. On the individual level, BOLD amplitude is very repeatable in healthy participants, whereas time-to-peak exhibits only moderate and time-to-baseline even poor repeatability [23]. In **chapter 3**, we analyzed a dataset previously collected by our group [23] with several frequently used postprocessing methods, and the same observations were made by us, independent of the applied methods [24]. Furthermore, in a longitudinal study where a decrease over time of the BOLD amplitude in CAA patients was shown, some CAA patients showed an increase, while some control participants showed a decrease [25]. This indicates that while vascular reactivity is progressively lower in CAA patients, it is at this point not a marker a clinician can use to confirm a CAA diagnosis. However, vascular reactivity is believed to be affected during the first stages of CAA [22], and was found a very robust marker on group level, both in cross-sectional as well longitudinal analyses [5, 25-27]. Therefore, these vascular reactivity measurements can be highly relevant as a marker in clinical trials and for research on disease progression. Because of the complexity of the underlying processes of the BOLD signal, one could imagine that further development of measuring the vascular reactivity could lead to an even more stable marker for disease progression or even diagnosis.

The advances in research into markers allow us to detect more and more subtle change in structure and physiology. Currently, diagnostics like the Boston criteria only include lesions, areas that have suffered damage from hemorrhagic and non-hemorrhagic sources. However, we are more able to detect, and subsequently link, underlying processes to CAA, or cSVD in general. In a future stage functional, and potentially reversible, markers may prove to be as important as or even more

important than lesion based markers, as they may indicate either an earlier diagnosis or a change in treatment or prognosis.

Automation

All chapters in this thesis have a degree of automation, and many of these chapters advocate for the use of more automation. While the use of public-domain software packages in combination with locally developed tools can make life easier and measurements more accurate and reproducible, one must be aware of the pitfalls of automation bias, where users appear to rely more on computational techniques than on their own judgement. Increasingly, artificial intelligence (AI) is making headlines and promises, also for clinical applications. Advances in AI are making a profound impact on MRI and radiology, especially by improving image quality and accelerating MRI exams [28]. These techniques are also applied to segment, classify and diagnose brain pathology [29, 30]. Pubmed shows an exponential growth curve for the number of publications using AI within the field of MRI, with 1,951 publications in 2022 for the MeSH terms of AI and MRI combined. For reference, the combination of the MeSH term for Alzheimer's disease and MRI yielded "only" 949 publications in 2022. The use of AI influences the reading time of radiologists: radiologists spend less time on chest radiographs that are reported as "normal" by AI [31]. However, in that study there was only a mean net gain of 1.5s per radiograph. Several other studies have retrospectively investigated reading times for radiologists combined with AI use, with most of them reporting a shortening of reading time. One of these studies suggested that the use of AI can reassure the radiologist from making the right negative diagnosis [32]. These results indicate that at this time there is only limited advantages of the use of AI for diagnosis, but when models and methods improve they may aid radiologists in their workflow. Recently, a study showed that an automation bias is introduced when radiologists, over the full range of experience, were supported by AI based techniques in reading of mammograms [33]. This automation bias

appears therefore to extend to (highly) experienced experts. It is therefore crucial to keep looking at your data and to keep a system of checks and balances in place, which is also evidenced in e.g. **chapter 3**.

Negative results

A number of publications in this thesis have what could be considered negative results. In **chapter 2** we attempted to determine flow territory information from traditional ASL scans. We successfully showed what variance in labelling efficiency and off resonance effects are needed to infer this information, but also showed that even in cases of severe pathology these conditions are not met. In **chapter 6** we investigated the venous morphology in D-CAA patients. Unlike the results found in Alzheimer's patients, and results in non-amyloid related small vessel disease [7-9, 12], we did not find a different morphology or number of veins between mutation carriers and healthy participants. Overall, positive result papers are more often published and cited [34, 35]. However, some studies find that in their respective field or journal little bias exists between the acceptance of positive and negative result manuscripts [36, 37]. One of these studies suggests that the publication bias would even occur before submission to journals, i.e. a form of self-censoring [37]. On the other hand, another study suggests that positive results are indeed more likely to be published in their field and that this is the most important cause of publication bias [38].

When commercial interests are present in a study, the incentive to publish negative results is further diminished: only 40% of studies in failed phase 3 drug trials are published [39]. It is my conviction, and this is luckily shared by many others, that negative results are an important aspect of science when the research is sufficiently carried out, and that publications of negative results should be more encouraged. Luckily, a trend towards this can be clearly seen in recent years [40, 41]. Omission of negative results in literature can lead to a bias in the literature as

well as a waste of time for future researchers inventing (a non-functional) wheel multiple times over, which is an unethical waste of resources. Furthermore, a biased literature negatively impact the validity of systematic reviews, meta-analyses, power calculations and future studies in general [42, 43].

While negative results are indeed important, and should not be shunned from publication, one should always make sure these results are indeed negative, and not due to errors in study design or power. Negative result publications in prominent journals have been found to often lack in description of the factors that may have led to the negative results [44]. With any publication carefully writing down the constraints is important, but with negative results even more so, as they are showing an absence of evidence of a difference (of course only at the power of the study sample at hand), and not a no difference at all [45].

REFERENCES

1. Dai, W., et al., *Quantifying fluctuations of resting state networks using arterial spin labeling perfusion MRI*. J Cereb Blood Flow Metab, 2016. **36**(3): p. 463-73.
2. Aslan, S., et al., *Estimation of labeling efficiency in pseudocontinuous arterial spin labeling*. Magn Reson Med, 2010. **63**(3): p. 765-71.
3. Wu, W.C., et al., *A theoretical and experimental investigation of the tagging efficiency of pseudocontinuous arterial spin labeling*. Magn Reson Med, 2007. **58**(5): p. 1020-7.
4. Wu, W.-C., et al., *Pseudocontinuous arterial spin labeling perfusion magnetic resonance imaging—A normative study of reproducibility in the human brain*. NeuroImage, 2011. **56**(3): p. 1244-1250.
5. van Opstal, A.M., et al., *Cerebrovascular function in pre-symptomatic and symptomatic individuals with hereditary cerebral amyloid angiopathy: a case-control study*. The Lancet. Neurology, 2017. **16**(2): p. 115-122.
6. Linn, J., et al., *Prevalence of superficial siderosis in patients with cerebral amyloid angiopathy*. Neurology, 2010. **74**(17): p. 1346-50.
7. Xu, Z., et al., *New Insights in Addressing Cerebral Small Vessel Disease: Association With the Deep Medullary Veins*. Front Aging Neurosci, 2020. **12**: p. 597799.
8. Zhang, R., et al., *A Brain Region-Based Deep Medullary Veins Visual Score on Susceptibility Weighted Imaging*. Front Aging Neurosci, 2017. **9**: p. 269.
9. Zhou, Y., et al., *Role of deep medullary veins in pathogenesis of lacunes: Longitudinal observations from the CIRCLE study*. J Cereb Blood Flow Metab, 2020. **40**(9): p. 1797-1805.
10. Jäkel, L., et al., *Prevalence of cerebral amyloid angiopathy: A systematic review and meta-analysis*. Alzheimers Dement, 2022. **18**(1): p. 10-28.

11. Greenberg, S.M., et al., *Cerebral amyloid angiopathy and Alzheimer disease - one peptide, two pathways*. Nat Rev Neurol, 2020. **16**(1): p. 30-42.
12. Bouvy, W.H., et al., *Abnormalities of Cerebral Deep Medullary Veins on 7 Tesla MRI in Amnesic Mild Cognitive Impairment and Early Alzheimer's Disease: A Pilot Study*. J Alzheimers Dis, 2017. **57**(3): p. 705-710.
13. Greenberg, S.M. and M.A. Edgar, *Case records of the Massachusetts General Hospital. Weekly clinicopathological exercises. Case 22-1996. Cerebral hemorrhage in a 69-year-old woman receiving warfarin*. N Engl J Med, 1996. **335**(3): p. 189-96.
14. Charidimou, A., et al., *The Boston criteria version 2.0 for cerebral amyloid angiopathy: a multicentre, retrospective, MRI-neuropathology diagnostic accuracy study*. Lancet Neurol, 2022. **21**(8): p. 714-725.
15. Wardlaw, J.M., et al., *Neuroimaging standards for research into small vessel disease and its contribution to ageing and neurodegeneration*. The Lancet Neurology, 2013. **12**(8): p. 822-838.
16. Duering, M., et al., *Neuroimaging standards for research into small vessel disease—advances since 2013*. The Lancet Neurology, 2023.
17. Charidimou, A., et al., *Cortical superficial siderosis and first-ever cerebral hemorrhage in cerebral amyloid angiopathy*. Neurology, 2017. **88**(17): p. 1607-1614.
18. Charidimou, A., et al., *Cortical superficial siderosis: detection and clinical significance in cerebral amyloid angiopathy and related conditions*. Brain, 2015. **138**(Pt 8): p. 2126-39.
19. Pongpitakmetha, T., et al., *Cortical superficial siderosis progression in cerebral amyloid angiopathy: Prospective MRI study*. Neurology, 2020. **94**(17): p. e1853-e1865.
20. Greenberg, S.M., et al., *Outcome markers for clinical trials in cerebral amyloid angiopathy*. Lancet Neurol, 2014. **13**(4): p. 419-28.
21. Kozberg, M.G., et al., *A practical approach to the management of cerebral amyloid angiopathy*. Int J Stroke, 2021. **16**(4): p. 356-369.
22. Koemans, E.A., et al., *Progression of cerebral amyloid angiopathy: a pathophysiological framework*. The Lancet Neurology, 2023.
23. van Dijk, S.E., et al., *Aging Effect, Reproducibility, and Test-Retest Reliability of a New Cerebral Amyloid Angiopathy MRI Severity Marker-Cerebrovascular Reactivity to Visual Stimulation*. J Magn Reson Imaging, 2022.
24. van Harten, T.W., et al., *Impact of ROI definition on visual stimulation based cerebral vascular reactivity fMRI with a special focus on applications in Cerebral Amyloid Angiopathy*. NMR Biomed, 2023: p. e4916.
25. Switzer, A.R., et al., *Longitudinal decrease in blood oxygenation level dependent response in cerebral amyloid angiopathy*. NeuroImage. Clinical, 2016. **11**: p. 461-467.
26. Switzer, A.R., et al., *Cerebrovascular reactivity in cerebral amyloid angiopathy, Alzheimer disease, and mild cognitive impairment*. Neurology, 2020. **95**(10): p. e1333-e1340.
27. Dumas, A., et al., *Functional MRI Detection of Vascular Reactivity in Cerebral Amyloid Angiopathy*. Annals of neurology, 2012. **72**(1): p. 76-81.
28. Kiryu, S., et al., *Clinical Impact of Deep Learning Reconstruction in MRI*. Radiographics, 2023. **43**(6): p. e220133.
29. Hong, J.S., et al., *Deep Learning Detection and Segmentation of Brain Arteriovenous Malformation on Magnetic Resonance Angiography*. J Magn Reson Imaging, 2023.
30. Wang, D., et al., *Deep learning-based magnetic resonance imaging of the spine in the diagnosis and physiological evaluation of spinal metastases*. J Bone Oncol, 2023. **40**: p. 100483.
31. Shin, H.J., et al., *The impact of artificial intelligence on the reading times of radiologists for chest radiographs*. NPJ Digit Med, 2023. **6**(1): p. 82.
32. Pacilè, S., et al., *Improving Breast Cancer Detection Accuracy of Mammography with the Concurrent Use of an Artificial Intelligence Tool*. Radiol Artif Intell, 2020. **2**(6): p. e190208.
33. Dratsch, T., et al., *Automation Bias in Mammography: The Impact of Artificial Intelligence BI-RADS Suggestions on Reader Performance*. Radiology, 2023. **307**(4): p. e222176.

34. Duyx, B., et al., *Scientific citations favor positive results: a systematic review and meta-analysis*. J Clin Epidemiol, 2017. **88**: p. 92-101.
35. Jannot, A.S., et al., *Citation bias favoring statistically significant studies was present in medical research*. J Clin Epidemiol, 2013. **66**(3): p. 296-301.
36. Okike, K., et al., *Publication bias in orthopaedic research: an analysis of scientific factors associated with publication in the Journal of Bone and Joint Surgery (American Volume)*. J Bone Joint Surg Am, 2008. **90**(3): p. 595-601.
37. van Lent, M., J. Overbeke, and H.J. Out, *Role of editorial and peer review processes in publication bias: analysis of drug trials submitted to eight medical journals*. PLoS One, 2014. **9**(8): p. e104846.
38. Chong, S.W., et al., *The relationship between study findings and publication outcome in anesthesia research: a retrospective observational study examining publication bias*. Can J Anaesth, 2016. **63**(6): p. 682-90.
39. Hwang, T.J., et al., *Failure of Investigational Drugs in Late-Stage Clinical Development and Publication of Trial Results*. JAMA Intern Med, 2016. **176**(12): p. 1826-1833.
40. Bespalov, A., T. Steckler, and P. Skolnick, *Be positive about negatives-recommendations for the publication of negative (or null) results*. Eur Neuropsychopharmacol, 2019. **29**(12): p. 1312-1320.
41. Mlinarić, A., M. Horvat, and V. Šupak Smolčić, *Dealing with the positive publication bias: Why you should really publish your negative results*. Biochem Med (Zagreb), 2017. **27**(3): p. 030201.
42. Rothstein, H.R., *Publication bias as a threat to the validity of meta-analytic results*. Journal of Experimental Criminology, 2008. **4**(1): p. 61-81.
43. Yang, Y., et al., *Publication bias impacts on effect size, statistical power, and magnitude (Type M) and sign (Type S) errors in ecology and evolutionary biology*. BMC Biology, 2023. **21**(1): p. 71.
44. Hebert, R.S., et al., *Prominent medical journals often provide insufficient information to assess the validity of studies with negative results*. J Negat Results Biomed, 2002. **1**: p. 1.
45. Altman, D.G. and J.M. Bland, *Absence of evidence is not evidence of absence*. Bmj, 1995. **311**(7003): p. 485.

Nederlandse Samenvatting

De rode draad door dit proefschrift is de ontwikkeling van nieuwe- en verbetering van bestaande MRI-technieken en nabewerkingsmethoden voor het meten van cerebrovasculaire pathologie. Omdat bepaalde cerebrovasculaire aandoeningen, zoals vasculaire dementie, niet op een bepaalde plek plaatsvinden, worden deze methoden toegepast door de gehele cerebrovasculaire vaatboom. Dit proefschrift begint met de grote (macro) arteriën (hoofdstuk 2), bespreekt dan de functie de microvasculatuur (hoofdstukken 3 en 4), vervolgens de overblijfselen van bloedingen in hersenweefsel (hoofdstuk 5), en daarna het veneuze deel. In het proefschrift wordt dus zowel gekeken naar de structuur als de functie van de totale cerebrovasculaire vaatboom.

In hoofdstuk 2 werd onderzocht of er meer informatie over de grote arteriële cerebrovasculaire vaten uit pCASL scans gehaald kan worden door nieuwe MRI-technieken te combineren met geavanceerde nabewerkingsmethoden. Ander onderzoek had al aangetoond dat er meer functionele informatie gehaald kan worden uit ASL-scans, zoals de resting-state netwerken. Bovendien is bekend dat lokale fysiologische en fysieke condities effect kunnen hebben op de efficiëntie van het pCASL-labelen. Door deze twee feiten te combineren kwamen wij tot de hypothese dat wellicht informatie over de stroomgebieden van arteriën gehaald kan worden uit signaal fluctuaties in ASL-scans. Om deze hypothese te testen, is het nodig om te weten welke mate van fluctuaties nodig zijn om, deze informatie over de stroomgebieden te bepalen op het niveau van een individuele deelnemer. Dit hebben wij in gezonde deelnemers bepaald door een extra gradient toe te voegen tijdens het labelings-proces, welke een spatieel patroon van signaalfunctuaties veroorzaakt. Door dergelijke extra vessel-encoding gradiënten toe te passen konden deze methoden stroomgebieden inderdaad van elkaar onderscheiden worden, maar dit wel ten koste van een ongeveer 8,5% lager perfusiesignaal en dus een reductie in signaal-ruis-verhouding van dezelfde orde grootte. Vervolgens hebben we gekeken of deze fluctuaties in vivo ook voldoende voorkomen om op individueel niveau stroomgebiedinformatie te krijgen. Dit

hebben wij gedaan door retrospectief te kijken naar pCASL scans van patiënten met een ernstige (>70%) unilaterale stenose in de binnenste halsslagader. In deze populatie konden wij aantonen dat dit niet het geval was.

We keken in hoofdstukken 3 en 4 dieper in de vaatboom, namelijk naar de functie van de microvasculatuur. Vasculaire reactiviteit na een visuele stimulus is een steeds beter beschreven marker voor CAA. In de vakliteratuur worden de uitkomstmaten op verschillende manieren bepaald, wat de vergelijking van resultaten tussen instituten en studies bemoeilijkt. In hoofdstuk 3 is gekeken naar de meest voorkomende manieren van nabewerking, welke vervolgens getest zijn voor hun effectiviteit en reproduceerbaarheid, en we bekeken de mogelijkheid van het optreden van statistische fouten wanneer deze methoden worden toegepast. We hebben hierbij ook laten zien wat voor effect dit kan hebben op patiëntenstudies. Doordat de D-CAA populatie in dit hoofdstuk een hoge mate van heterogeniteit heeft, komt dit effect nog duidelijker naar voren. De reproduceerbaarheid van de methoden werd gekwantificeerd in een test-retest onderzoek. We lieten zien dat terwijl in gezonde deelnemers de drie methoden verschillende voxels includeerden, deze wel degelijk gelijke resultaten opleverden. Echter, in D-CAA patiënten met ernstige pathologie liet één van de methoden een hogere reactiviteit zien en includeerde ook voxels buiten de regio waar men activatie mag verwachten. Dit komt door circulaire analyse of zogeheten 'double dipping'. Onze data lieten zien dat de effecten van deze bias vooral zichtbaar zijn in patiënten met een hemodynamische respons die erg verstoord is, en om dergelijke bias te vermijden raden wij de andere methoden aan voor gebruik in toekomstig onderzoek.

In hoofdstuk vier zijn dergelijke hemodynamische veranderingen verder onderzocht in een cohort van jonge, vrouwelijke D-CAA mutatie-dragers en gezonde deelnemers, maar dan met een nieuwe 7 Tesla fMRI scan met een zeer hoge temporele resolutie. Om de hemodynamische respons beter te beschrijven is

een korte stimulus (3 seconden) gebruikt in combinatie met een lange rust periode (45 seconden). Deze lange rust periode zorgt ervoor dat de vasculatuur weer herstelt tot een normale rust conditie na elke activatieperiode. Uit de resultaten blijkt dat vooral de positieve BOLD-respons aangedaan is bij D-CAA patiënten, waarbij de post-stimulus 'undershoot' veel minder was aangedaan. In een eerdere 3 Tesla studie met patiënten met D-CAA in ons ziekenhuis, was er een aantal symptomatische patiënten met D-CAA die weinig tot geen respons hadden na de stimulus. Een interessante bevinding van dit hoofdstuk is dat sommige van de D-CAA mutatie-dragers die op 3 Tesla en 7 Tesla met een traditioneel paradigma en BOLD-sequentie geen respons lieten zien, wel een hemodynamische respons lieten zien met behulp van de hoog temporele resolutie BOLD-sequentie na een korte visuele stimulus.

Een belangrijke beeldvormingsbevinding in CAA is corticale superficiële siderose (cSS), welke in toenemende mate als een risicofactor voor toekomstige intracranieële bloedingen wordt erkend. Deze marker werd voor het eerst toegevoegd aan de Boston criteria voor CAA in de gemodificeerde versie (ook wel bekend als versie 1.5). De aanwezigheid en/of progressie van cSS is traditioneel beschreven in categorische schalen. Dit leidt tot een verlies van informatie op patiëntniveau door plafondeffecten, en ook verlies van informatie op groepsniveau door de grote heterogeniteit in de hoogste categorieën. In hoofdstuk 5 is deze categorische schaal doorontwikkeld tot een kwantitatieve schaal door segmentatie van cSS op susceptibiliteitsgewogen MRI-beelden, en vervolgens het volume te kwantificeren op een nieuwe, semiautomatische manier. Door deze nieuwe manier van het beoordelen van siderose, zijn we erin geslaagd om de heterogeniteit tussen patiënten in de hoogste categorie van elkaar te onderscheiden. Ook werd het mogelijk om binnen dezelfde patiënt de ziekteprogressie te volgen zonder last te hebben van plafondeffecten. De hoogste categorie had ook de hoogste heterogeniteit in cSS-volume (tussen 2.7 cm³ en 16.5 cm³), en na een follow-up periode van een jaar zagen we progressie in drie van de

vijf patiënten met sCAA, waarvan twee al in de hoogste categorie zaten bij de eerste scan.

Veranderingen in diepe medullaire venen zijn bekend in een aantal verschillende cerebrovasculaire aandoeningen. CAA is een van de meest voorkomende cerebrovasculaire aandoeningen en een veel voorkomende co-morbiditeit van de ziekte van Alzheimer. In patiënten met de ziekte van Alzheimer is de morfologie van diepe medullaire venen verschillend vergeleken met die van gezonde deelnemers. In hoofdstuk 6, zijn startpunten gegenereerd voor het vervolgen van diepe medullaire venen op susceptibiliteitsgewogen MRI-beelden. Deze punten werden gezet op die plaatsen waar tubulaire structuren het opgeblazen oppervlak van de laterale ventrikels doorkruisten. Vervolgens zijn de diepe medullaire venen gesegmenteerd door een tweerichtings tubulaire trackingsalgoritme. Door deze methode te gebruiken laten we zien dat diepe medullaire venen niet verschillend waren in aantal, tortuositeit of homogeniteit tussen gezonde deelnemers, presymptomatische en symptomatische D-CAA dragers. Ook vonden we geen associatie tussen MRI-markers gerelateerd aan CAA en veneuze morfologische parameters. Dit leidt tot de conclusie dat in D-CAA de depositie van amyloïde geen effect heeft op de diepe medullaire venen en dat de diepe medullaire venen geen grote rol spelen in de pathogenese van D-CAA.

List of publications

1. Schipper MR, Vlegels N, **van Harten TW**, Rasing I, Koemans EA, Voigt S, Luca A, Kaushik K, van Etten ES, van Zwet EW, Terwindt GM, Biessels GJ, van Osch MJ, van Walderveen MA, Wermer MJ. J Cereb Blood Flow Metab. 2023 Dec;43(12):2144-2155. doi: 10.1177/0271678X231200425.
2. **van Harten TW**, Koemans EA, Voigt S, Rasing I, van Osch MJP, van Walderveen MAA, Wermer MJH. Quantitative measurement of cortical superficial siderosis in cerebral amyloid angiopathy. Neuroimage Clin. 2023;38:103447. doi: 10.1016/j.nicl.2023.103447
3. Koemans EA, van Walderveen MAA, Voigt S, Rasing I, **van Harten TW**, J A van Os H, van der Weerd N, Terwindt GM, van Osch MJP, van Veluw SJ, Freeze WM, Wermer MJH. Subarachnoid CSF hyperintensities at 7 tesla FLAIR MRI: A novel marker in cerebral amyloid angiopathy. Neuroimage Clin. 2023;38:103386
4. **van Harten TW**, van Rooden S, Koemans EA, van Opstal AM, Greenberg SM, van der Grond J, Wermer MJH, van Osch MJP. Impact of region of interest definition on visual stimulation-based cerebral vascular reactivity functional MRI with a special focus on applications in cerebral amyloid angiopathy. NMR Biomed. 2023 Jul;36(7):e4916
5. Koemans EA, Castello JP, Rasing I, Abramson JR, Voigt S, Perosa V, **van Harten TW**, van Zwet EW, Terwindt GM, Gurol ME, Rosand J, Greenberg SM, van Walderveen MAA, Biffi A, Viswanathan A, Wermer MJH. Sex Differences in Onset and Progression of Cerebral Amyloid Angiopathy. Stroke. 2023 Feb;54(2):306-314.
6. **van Harten TW**, Heijmans A, van Rooden S, Wermer MJH, van Osch MJP, Kuijf HJ, van Veluw SJ, Greenberg SM, van Buchem MA, van der Grond J, van Walderveen MAA. Brain Deep Medullary Veins on 7T MRI in Dutch-Type Hereditary Cerebral Amyloid Angiopathy. J Alzheimers Dis. 2022;90(1):381-388
7. Arts T, Onkenhout LP, Amier RP, van der Geest R, **van Harten TW**, Kappelle J, Kuipers S, van Osch MJP, van Bavel ET, Biessels GJ, Zwanenburg JJM; Heart-Brain Connection Consortium. Non-Invasive Assessment of Damping of Blood Flow Velocity Pulsatility in Cerebral Arteries With MRI. J Magn Reson Imaging. 2022 Jun;55(6):1785-1794.
8. Koemans EA, Voigt S, Rasing I, **van Harten TW**, Jolink WMT, Schreuder FHBM, van Zwet EW, van Buchem MA, van Osch MJP, Terwindt GM, Klijn CJM, van Walderveen MAA, Wermer MJH. Cerebellar Superficial Siderosis in Cerebral Amyloid Angiopathy. Stroke. 2022 Feb;53(2):552-557.

9. Schmitz-Abecassis B, Vinogradov E, Wijnen JP, **van Harten TW**, Wiegers EC, Hoogduin H, van Osch MJP, Ercan E. The use of variable delay multipulse chemical exchange saturation transfer for separately assessing different CEST pools in the human brain at 7T. *Magn Reson Med*. 2022 Feb;87(2):872-883. doi: 10.1002/mrm.29005.
10. Rasing I, Voigt S, Koemans EA, van Zwet E, de Kruijff PC, **van Harten TW**, van Etten ES, van Rooden S, van der Weerd L, van Buchem MA, van Osch MJP, Greenberg SM, van Walderveen MAA, Terwindt GM, Wermer MJH. Occipital Cortical Calcifications in Cerebral Amyloid Angiopathy. *Stroke*. 2021 May;52(5):1851-1855.
11. Bulk M, **van Harten TW**, Kenkhuis B, Inglese F, Hegeman I, van Duinen S, Ercan E, Magro-Checa C, Goeman J, Mawrin C, van Buchem M, Steup-Beekman G, Huizinga T, van der Weerd L, Ronen I. Quantitative susceptibility mapping in the thalamus and basal ganglia of systemic lupus erythematosus patients with neuropsychiatric complaints. *Neuroimage Clin*. 2021;30:102637.
12. Koemans EA, Voigt S, Rasing I, Jolink W, **van Harten TW**, van der Grond J, van Rooden S, Schreuder F, Freeze WM, van Buchem MA, van Zwet EW, van Veluw SJ, Terwindt GM, van Osch M, Klijn C, van Walderveen M, Wermer M. Striped occipital cortex and intragryal hemorrhage: Novel magnetic resonance imaging markers for cerebral amyloid angiopathy. *Int J Stroke*. 2021 Dec;16(9):1031-1038.
13. **van Harten TW**, Dzyubachyk O, Bokkers RPH, Wermer MJH, van Osch MJP. On the ability to exploit signal fluctuations in pseudocontinuous arterial spin labeling for inferring the major flow territories from a traditional perfusion scan. *Neuroimage* 2001, 230, 117813.
14. Ter Telgte A, Scherlek AA, Reijmer YD, van der Kouwe AJ, **van Harten TW**, Duering M, Bacskai BJ, de Leeuw FE, Frosch MP, Greenberg SM, van Veluw SJ. Histopathology of diffusion-weighted imaging-positive lesions in cerebral amyloid angiopathy. *Acta Neuropathol*. 2020 May;139(5):799-812.
15. van Opstal AM, van Rooden S, **van Harten TW**, Ghariq E, Labadie G, Fotiadis P, Gurol ME, Terwindt GM, Wermer MJH, van Buchem MA, Greenberg SM, van der Grond J. Cerebrovascular function in presymptomatic and symptomatic individuals with hereditary cerebral amyloid angiopathy: a case-control study. *Lancet Neurol*. 2017 Feb;16(2):115-122.

16. Charidimou A, Morotti A, Valenti R, Giese AK, Boulouis G, Pasi M, Roongpiboonsopit D, Lauer A, Xiong L, **van Harten TW**, Karadeli H, Fotiadis P, Jessel MJ, Viswanathan A. Journal Club: Time trends in incidence, case fatality, and mortality of intracerebral hemorrhage. *Neurology*. 2016 May 17;86(20):e206-9.

Curriculum Vitae

Thijs van Harten was born on May 31st 1985, in 's-Gravenhage, the Netherlands. His academic career started in Leiden, with the bachelor Biomedische Wetenschappen in 2010, with a minor in Science Based Business. He did his bachelor's internship on 'Lineage-specific chimerism analysis in patients after allogeneic stem cell transplantation and DLI' at the department of experimental hematology at the Leiden University Medical Center. After his bachelor he continued with the research Master of Biomedical Sciences and did his first internship at the department of Radiology at the Leiden University Medical Center titled 'Vascular Changes in Cerebral Amyloid Angiopathy', looking at structural and functional changes in a patient control study in D-CAA. This led to another internship at Massachusetts General Hospital on 'Neuropathology of Small Vessel Disease', where he investigated the link between in vivo MRI, ex vivo MRI, and histology in CAA patients. Subsequently, he started as a PhD candidate in 2017 at the department of Radiology of the Leiden University Medical Center, during which he focused on advanced MRI markers of cerebral small vessel disease. Currently, he is continuing his research as a research fellow at Massachusetts General Hospital.